

General Energy Research Department
Laboratory of Atmospheric Chemistry

Modelling of air quality for winter and summer episodes in Switzerland

Final Report

S. Andreani-Aksoyoglu, J. Keller, I. Barmpadimos, D. Oderbolz, M. Tinguely, A.S.H. Prévôt
Laboratory of Atmospheric Chemistry, Paul Scherrer Institut, 5232 Villigen PSI, Switzerland

M.R. Alfarra
University of Manchester, UK

J. Sandradewi
An den Birnbäumen 29, 37671 Höxter, Germany

This project was financially supported by the Federal Office of Environment, FOEN
(Bundesamt für Umwelt, BAFU)

Summary

The air quality in Switzerland was modelled with a regional air quality model for three episodes, January-February 2006, June 2006 and January 2007. The focus of the calculations was on the particulate matter concentrations, as well as ozone in summer. The model results were compared with the aerosol data collected by the Aerosol Mass Spectrometer (AMS), which was operated during all three episodes and with the air quality monitoring data from the NABEL stations, as well as the detailed measurements performed at Payerne within the frame of the EMEP monitoring programme. The air quality model used in this study is the 3-dimensional photochemical model CAMx (Comprehensive Air quality Model with eXtensions). There were 3 nested model domains covering a large part of the European continent, central Europe and Switzerland with horizontal resolutions of $27\text{ km} \times 27\text{ km}$, $9\text{ km} \times 9\text{ km}$ and $3\text{ km} \times 3\text{ km}$, respectively. We produced the meteorological input data for each grid cell using the MM5 meteorological model. Our emission inventory contains both anthropogenic and biogenic emissions in all model domains. Initial and boundary conditions were obtained from the global model MOZART used for similar periods. We calculated selected statistical parameters in order to evaluate the model performance both in winter and summer periods.

In general, the model system is able to predict gaseous and particulate matter concentrations reasonably well except during low-wind conditions when the model performance gets worse. The concentrations of pollutants could be reproduced satisfactorily when the wind speed was moderate or strong. Under stagnant conditions (low-wind), meteorological model fails to capture the structure of atmospheric boundary layer and in particular temperature inversions. The vertical transport is therefore not well estimated. Another project to improve the performance of the meteorological model is under way. The problems associated with the low-wind conditions, are expected to be eliminated in the near future.

The statistical evaluation of ozone concentrations in summer show that the model performance criteria are met at some NABEL stations such as Chaumont, Laegern, Payerne, Taenikon (rural) as well as Lugano (urban), Rigi and Davos (elevated). The worst model performance was obtained for the stations Basel (suburban), Bern (urban) and Haerkingen (motorway).

The model performance for inorganic aerosols such as particulate nitrate, sulphate and ammonium is better than for organic aerosols. The air quality model results for northern Switzerland suggest that the particulate nitrate and organic aerosols dominate the aerosol composition in winter, as shown also by the measurements. The model predicts that organic aerosols are mainly primary in winter. However, measurement data suggest that more than half of the organic aerosols in winter are secondary. In summer, the main component of aerosols is the organic aerosol fraction and it is mostly secondary. Secondary organic aerosols are predicted to come mainly from the biogenic precursors. The model underestimates the organic aerosol mass concentrations in winter as well as in summer as other current regional models. The improvement of wood-burning emissions in the inventory might lead to a better simulation of organic aerosols especially in winter. The disagreement between measurements and model results is believed to be mainly due to the secondary organic aerosols (SOA) formation, which is not yet understood completely and therefore not treated properly in the models. Recent studies indicate new formation pathways from species not treated before and new processes such as

oligomerization of SOA in addition to the simple partitioning between gas- and particle phase. These new SOA formation mechanisms had not been treated in the model version used in this study. However, the latest CAMx version which became recently available, contains a new SOA module allowing oligomerization of aerosols, together with the new pathways to SOA formation from isoprene and sesquiterpenes, in addition to formation from monoterpenes. Furthermore, the gas-phase mechanism CB4 was replaced in the new version by the updated mechanism CB05 that was shown to lead to improvements in ozone and PM modelling. The model performance of CAMx is therefore expected to improve –especially for organic aerosols- in future studies.

Table of Contents

1	Introduction.....	7
2	Models.....	9
2.1	Meteorological Model MM5.....	9
2.1.1	Model description	9
2.1.2	MM5 Model setup.....	9
2.2	Photochemical Model CAMx.....	12
2.2.1	Model description	12
2.2.2	Gas-phase chemistry	13
2.2.3	Aerosol chemistry.....	13
2.2.4	Pollutant Removal	14
2.2.5	Input and Output Files	14
2.2.6	CAMx Model setup	15
3	Emissions.....	17
3.1	European Anthropogenic Emissions.....	17
3.2	Swiss Anthropogenic Emissions	18
3.2.1	Road traffic emissions.....	18
3.2.2	Industrial and residential emissions.....	19
3.2.3	Other emissions	19
3.3	Biogenic Emissions.....	19
3.4	Conversion of the emissions to the CAMx grids	20
4	Model performance evaluation	21
4.1	General.....	21
4.2	Meteorology	21
4.3	Air quality	22
5	Episode 1: January-February 2006	25
5.1	Meteorology	25
5.2	Gaseous pollutants	36
5.3	Aerosols.....	41
6	Episode 2: June 2006.....	57
6.1	Meteorology	57
6.2	Gaseous pollutants	59
6.3	Aerosols.....	66
7	Episode 3: January 2007.....	77
7.1	Meteorology	77

7.2 Gaseous pollutants	80
7.3 Aerosols.....	85
8 Conclusions.....	96
Acknowledgements.....	98
Acronyms.....	99
References	101
Appendix.....	107

1 Introduction

Atmospheric aerosols are known to have adverse health effects and they play an important role in climate change by modifying the radiative balance of the atmosphere (IPCC, 2007). The legal threshold for the yearly average of PM₁₀ (particles smaller than 10 μm in aerodynamic diameter d) is 20 $\mu\text{g m}^{-3}$ in Switzerland. As a short-term threshold, the concentration averaged over 24 hours may exceed 50 $\mu\text{g m}^{-3}$ only once a year. PM₁₀ concentrations in Switzerland frequently exceed the threshold values, especially in the southern part of the Alps. The health relevant particles are considered to be those with smaller sizes ($d < 1 \mu\text{m}$ or $d < 2.5 \mu\text{m}$). However, there is no ambient air quality standard for PM₁ or PM_{2.5} in Switzerland.

While the formation of gaseous pollutants such as ozone is well known, there is still a lack of knowledge about aerosol formation. *Gehrig and Buchmann* (2003) evaluated the long-term PM_{2.5} and PM₁₀ measurements at various Swiss sites. *Hueglin et al.* (2005) investigated the chemical composition of atmospheric PM showing that organic matter, sulphate and nitrate are the main contributors to the annual PM_{2.5} mass concentration at rural, near-city and urban background sites. At kerbside sites, organic matter (30%) and elemental carbon (17%) are the two main contributors while inorganic aerosols all together contribute around 30% to the annual aerosol concentration. The authors also showed that nitrate levels were much lower in summer than in winter. Recently, *Lanz et al.* (2007) characterized submicron ambient aerosol in summer 2005 at an urban background site at Zurich using positive matrix factorization (PMF) for aerosol mass spectrometer (AMS) data. The authors concluded that only a small (<10%) fraction of organic PM originates from freshly emitted fossil fuel combustion while other primary sources contribute with similar or higher importance such as charbroiling (10-15%) and wood burning (10%) and food cooking (6%). A high fraction (60-69%) of the measured organic aerosol mass was shown to be oxygenated organic aerosol (OOA) which was interpreted mostly as secondary organic aerosol (SOA). In a more recent study, *Lanz et al.* (2008) applied the same method to the data for winter 2006 at the same site. The results suggested that the major components of organic aerosols was OOA (52-57%). ¹⁴C measurements of organic carbon indicated that 31 and 69% of OOA originated from fossil and non-fossil sources, respectively. Particles from wood burning (35-40%) and traffic-related hydrocarbon-like organic aerosol (3-13%) accounted for the other half of measured organic matter.

Understanding the partitioning behaviour of semi-volatile species between the gas and aerosol phases can help us to predict how changes in anthropogenic and biogenic activity will influence the formation of aerosols in the atmosphere. With this understanding, appropriate control strategies can be developed. In recent years several air quality models have been upgraded to include aerosol dynamical processes such as coagulation, nucleation, evaporation, and condensation and a transition from bulk to size-resolved treatment of aerosol microphysics and chemistry has been undertaken to better account for aerosol processes (*Zhang et al.*, 2004; *Held et al.*, 2004). Modelling secondary organic aerosol (SOA) formation is among the most demanding aspects associated with atmospheric organic photo-oxidation because the formation process depends on a) the representation of the parent organic species that lead to condensable products after being oxidized, b) the gas-phase chemistry where condensable species are formed, and c) the representation

of the gas/particle partitioning process of the condensable compounds. The temperature dependence of SOA formation is another key point of uncertainties affecting models. The current models often underestimate SOA concentrations (Zhang *et al.*, 2004; Cousin *et al.*, 2005, Volkamer *et al.*, 2006). Recent experimental evidence for oligomerization reactions in organic aerosols indicated the need to readdress the current assumptions in models about the partitioning of oxidation products in the gas and the particle phase (Kalberer *et al.*, 2004). A recent model study by Morris *et al.* (2006) showed that including mechanisms that are not yet treated in current models, such as oligomerization, SOA formation from isoprene and sesquiterpenes, led to increased SOA yields. Robinson *et al.* (2007) indicated another pathway to SOA formation from primary organic-particulate emissions. Authors showed experimentally that photo-oxidation of diesel emissions rapidly generates organic aerosol, greatly exceeding the contribution from known secondary organic-aerosol precursors. This new mechanism will soon be implemented in the current air quality models.

Applications of aerosol models require speciated aerosol measurements at high temporal and spatial resolution (Held *et al.*, 2004; Yin *et al.*, 2004; Bessagnet *et al.*, 2004; Cousin *et al.*, 2005). In Switzerland with its very complex terrain, some 3-dimensional modelling studies were conducted for ozone (Kuebler *et al.*, 2002; Andreani-Aksoyoğlu *et al.*, 2001; Keller *et al.*, 2008, Andreani-Aksoyoğlu *et al.*, 2008a). However, there are very few model studies on aerosols (Andreani-Aksoyoğlu *et al.*, 2003; Andreani-Aksoyoğlu *et al.*, 2008b). For the region south of the Alps around Milan, most of the studies have concentrated on ozone or trace gases like VOCs, NO₂, and formaldehyde (Baertsch-Ritter, *et al.*, 2003; Neftel, *et al.*, 2002; Martilli, *et al.*, 2002; Steinbacher, *et al.*, 2005; Liu, *et al.*, 2007a,b; Ordóñez, *et al.*, 2006). It was found that this region is one of the most polluted areas in Europe due to the high emissions but also due to the meteorological features of the Po basin. Ozone production in Milan was shown to be strongly VOC sensitive for a large range of meteorological conditions (Baertsch-Ritter, *et al.*, 2004). In the last years, studies on particulate matter are also getting into the focus because of the very high concentrations in this area (Baltensperger, *et al.*, 2002; Andreani-Aksoyoğlu, *et al.*, 2004; 2008b, Putaud, *et al.*, 2002, Vecchi *et al.*, 2007).

The aerosol concentrations were very high during January-February 2006 in Switzerland. There were several measurements during that period investigating the chemical composition of particles. Additional measurements within the frame of the European EMEP programme were performed at Payerne in June 2006 and January 2007. Availability of detailed aerosol measurements during all three episodes gives a unique opportunity to test the models under different meteorological conditions over the complex terrain of Switzerland. In this study, the air quality in Switzerland was modelled during those three episodes and model's capability of capturing the summer and winter smog characteristics was tested.

2 Models

2.1 Meteorological Model MM5

2.1.1 Model description

The dispersion of air pollutants is predominantly controlled by the prevailing meteorological conditions. On the one hand, the wind pattern determines the advective transport. Heavily polluted air from high emission regions may increase the pollution level in downwind areas. Conversely, air from large regions with low human activity is mostly clean and may improve air quality. For instance, the poor air quality in the Po basin influences the pollutants' level in southern Switzerland during south wind conditions, whereas cleaner air is observed when the wind is blowing from the north (*Weber and Prévôt, 2002*). On the other hand, a stable atmosphere confines the pollutants to a small air volume leading to high concentrations. A persistent inversion layer prevents the air from being vertically mixed.

Eulerian air quality models compute the spatial and temporal distributions of atmospheric species on a 3-dimensional rectangular grid. The meteorological data must be available for the same coordinates. Gridded data can be derived from numerical forecasts or from monitored data provided by the national weather services. The grid and the resolution of these data, however, are usually different from those required by the air quality model.

To solve this problem, a meteorological model can be tailored in order to match its output parameters and grids to the needs of the air quality model. At the Laboratory of Atmospheric Chemistry (LAC) we apply the meso-scale model MM5 (*PSU/NCAR, 2004*) as the meteorological driver for the Comprehensive Air Quality Model with Extensions (CAMx). Currently, the most recent version 3.7.4, issued in October 2006, is used. This version has new features for the simulation in complex terrain (*Zaengl, 2002*). Up to 4 nested grids can be defined. The most suitable projection for mid-latitude domains is the Lambert Conic Conformal one, which transforms the earth's surface to a cone. This cone is specified by the longitude and latitude of the coarse domain's centre, and by the "true" latitudes where the cone intersects the earth's surface. The position of the cone was selected in such a way that the coordinate system is close to the oblique Mercator grid used by the Federal Office of Topography, SWISSTOPO. Time in MM5 is specified as UTC (Universal Time Coordinated).

2.1.2 MM5 Model setup

MM5 supports both 1-way and 2-way nesting. If the 1-way nesting option is selected, the mother domain (domain 1) is modelled first, and the boundaries for the daughter domain (domain 2) are extracted from the output using the pre-processor NESTDOWN. For a 3rd domain nested entirely in domain 2, the cycle is repeated in an analogous way. In the case of 2-way nesting, all domains are treated in one single run. The daughter domains are controlled by their mother domains at the boundaries and feed back information to the higher domain. This feature, however, requires that the grid cell size of the daughter domain is 1/3 of that of the mother domain. Although we used the 1-way option in this study due to memory limitations, we kept the factor 3 between the grid cell sizes of mother and daughter domains.

The coarse domain has roughly the same size as the COSMO 7 model domain, which covers a large part of the European continent. COSMO 7 (COSMO, 2002) is the meteorological forecast model, which is currently in use at the Swiss Met Office, MeteoSwiss. For the present study 3 nested domains were defined for MM5. They were specified in accordance with the requirements of CAMx (see also Sec. 2.2.6).

Projection:

centre longitude	: 3.5 deg E
centre latitude	: 47.0 deg N
true latitude 1	: 46.0 deg N
true latitude 2	: 48.0 deg N

Coarse grid (domain 1):

grid cell size	: 27 km × 27 km
number of cells	: 95 × 79
domain size	: 2565 km × 2133 km

(see Figure 2.1.1)

1st fine grid (domain 2):

grid cell size	: 9 km × 9 km
number of cells	: 78 × 60
domain size	: 702 km × 540 km

(see Figure 2.1.2)

2nd fine grid 2 (domain 3):

grid cell size	: 3 km × 3 km
number of cells	: 132 × 96
domain size	: 396 km × 288 km

(see Figure 2.1.3)

Vertical layering:

31 terrain-following σ -levels

We chose the Eta PBL option, using the Mellor-Yamada scheme, to calculate the planetary boundary layer height (PBL) (Janjić, 1994).

The meteorology of the 3 episodes January - February 2006, June 2006 and January 2007 was simulated in groups of 4 days (e.g. 1 – 4 January, 4 – 7 January,...). The first full day was used as the spin up day initialized by COSMO 7 analyses. The simulation results of the next 3 consecutive days were used as input for CAMx. An overlap of 1 day was inserted for the next 4-day period, i.e. the spin-up day started, for instance, on 4 January at 0:00 UTC. Four-dimensional data analysis (FDDA) using COSMO 7 (analyses data) was applied for domains 1 and 2, whereas domain 3 was modelled without nudging. The meteorological variables required by CAMx are extracted and converted to CAMx format using the post-processor MM5CAMx. In addition, this program calculates the vertical diffusivity K_v which is not an output of

MM5 but required by CAMx. The CMAQ scheme for calculating K_v was used in this study. MM5 currently runs on a 32-bit multi-processor cluster using 4 to 20 processors depending on the number of jobs in the input queue.

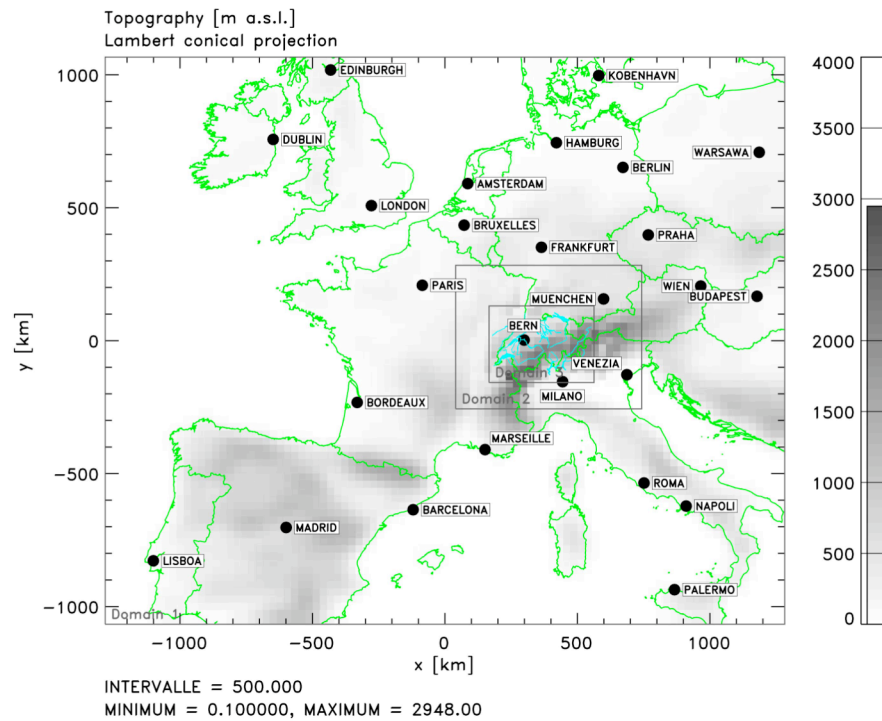


Figure 2.1.1: Topography of MM5 domain 1; 27 km × 27 km horizontal resolution

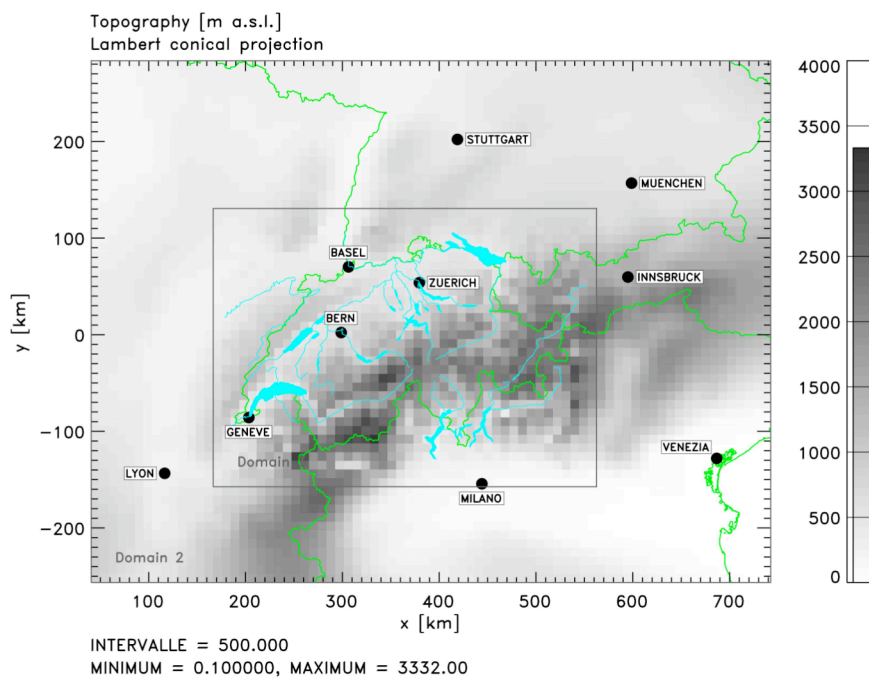


Figure 2.1.2: Topography of MM5 domain 2; 9 km × 9 km horizontal resolution

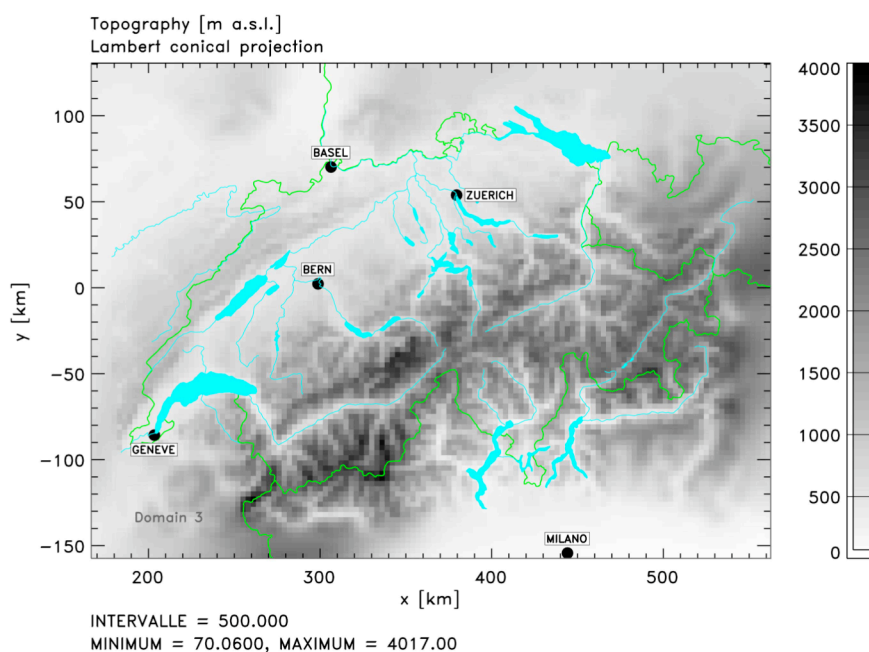


Figure 2.1.3: Topography of MM5 domain 3; 3 km × 3 km horizontal resolution

2.2 Photochemical Model CAMx

2.2.1 Model description

In this study, the CAMx model (version 4.40) was used with three nested domains (Environ, 2006). CAMx is a Eulerian photochemical dispersion model that allows for an integrated “one-atmosphere” assessment of gaseous and particulate air pollution over many scales ranging from urban to regional. It is designed to unify all of the technical features required of “state-of-the-science” air quality models into a single system that is computationally efficient and publicly available. CAMx simulates the emission, dispersion, chemical reactions, and removal of pollutants in the lower troposphere by solving the pollutant continuity equation for each chemical species on a system of nested three-dimensional grids. The model incorporates two-way grid nesting, which means that pollutant concentration information propagates into and out of all grid nests. This feature allows CAMx to be run with coarse grid spacing over a wide regional domain in which high spatial resolution is not particularly needed. Within the same run, fine grid nesting is applied in areas where high resolution is required.

Similar to MM5, CAMx can perform simulations on various types of Cartesian map projections. The Lambert Conic Conformal projection identical to that of MM5 was used for this study. Furthermore, the vertical grid structure is defined externally, so layer interface heights may be specified as any arbitrary function of space and/or time. This flexibility in defining the horizontal and vertical grid structures allows CAMx to be configured to match the grid of many meteorological models that are used to provide environmental input fields.

2.2.2 Gas-phase chemistry

There are five chemical mechanisms supported in the CAMx version 4.40. These are three different versions of Carbon Bond Mechanism CBM-IV (Gery, *et al.*, 1989) (one with revised and updated CBM-IV, one with reactive chlorine chemistry, one with the extensions for aerosol modelling), SAPRC99 chemical mechanism (Carter, 2000) and a user-defined simple chemistry mechanism. In this study, the CBM-IV mechanism with the extensions for aerosol modelling was used. Photolysis rates were derived for each grid cell assuming clear sky conditions as a function of five parameters: solar zenith angle, altitude, total ozone column, surface albedo and atmospheric turbidity. Since the photolysis rates are significantly affected by the presence of clouds, a cloud input file is required in case of cloudy conditions. The model provides an option to adjust photolysis rates for the presence of clouds using the approach developed for the Regional Acid Deposition Model (RADM) (Chang, *et al.*, 1987). This approach provides a realistic impact on photolysis rates by accounting for cloud optical depth. Besides reducing photolysis below clouds, photolytic rates are enhanced above clouds due to reflection.

2.2.3 Aerosol chemistry

The aerosol species calculated by CAMx include sulphate, nitrate, ammonium, secondary organic aerosols (5 classes based on the precursors), primary organic aerosols, elemental carbon, sodium, chloride, and primary inert material. In CAMx, aerosol processes are linked to the CBM-IV gas-phase mechanism. The gas-phase photochemistry forms aerosol precursors via the OH initiated oxidation of SO₂ to sulphate, production of nitric acid, and formation of condensable organic gases. The CBM-IV precursors TOL (mostly toluene) and XYL (mostly xylene) produce two different condensable species CG1 and CG2. In the model, there are three more condensable organic gases (CG3, CG4 and CG5) produced by the oxidation of alkanes, monoterpenes (biogenic) and cresol.

The aerosol precursors are supplied to aerosol chemistry, which performs the following processes:

- aqueous sulphate and nitrate formation in resolved cloud water using RADM aqueous chemistry algorithm (Chang, *et al.*, 1987)
- partitioning of condensable organic gases (CG1-CG5) to secondary organic aerosols (SOA1-SOA5) to form a condensed organic solution phase using a semi-volatile equilibrium scheme called SOAP (Strader, *et al.*, 1998)
- partitioning of inorganic aerosol constituents (sulphate, nitrate, ammonium, sodium, and chloride) between the gas and particle phases using the ISORROPIA thermodynamic module (Nenes, *et al.*, 1998)

CAMx provides two options for treating aerosol size distributions: the coarse/fine (CF) scheme and sectional (CMU) scheme from Carnegie Mellon University. The CF scheme divides the size distribution into two modes as coarse and fine. Primary species are modelled as fine and/or coarse particles, while all secondary species are treated as fine particles. The CMU scheme employs a sectional approach that models the size evolution of each aerosol constituent among a number of fixed size sections. The user defines the number of size sections and their size ranges. In this scheme, the bulk aerosol concentrations from the aqueous/aerosol chemistry modules are distributed into each size bin. The nucleation model employs the nucleation rate parameterization proposed by Russell, *et al.* (1994). The coagulation rate of aerosol particles is modelled according to Seinfeld and Pandis (1998).

2.2.4 Pollutant Removal

Trace gases and particles are removed from the atmosphere via deposition to the surface. Dry deposition refers to the direct sedimentation and/or diffusion of material to various terrestrial surfaces and uptake into biota. Dry deposition of gases is based on the resistance model of *Wesely* (1989). Surface deposition of particles occurs via diffusion, impaction and/or gravitational settling. The resistance approach used in UAM-AERO (*Kumar, et al.*, 1996) has been adopted in CAMx.

Wet deposition refers to the uptake of material via chemical absorption (gases) or nucleation/impaction (particles) into cloud water, and subsequent transfer to the Earth's surface by precipitation. The efficiency of wet and dry deposition processes to remove pollutants from the air depends on the physical and chemical properties of the pollutants, local meteorological conditions, the type of surface on which they are being deposited, and on the frequency, duration, and intensity of precipitation events. The wet scavenging model implemented in CAMx, calculates the following processes: wet scavenging of gases within and below precipitating clouds, wet scavenging of gases dissolved in cloud water, wet scavenging of in-cloud aerosols, and wet scavenging of dry particles.

2.2.5 Input and Output Files

CAMx requires various input data to describe photochemical conditions, surface characteristics, initial and boundary conditions, emission rates, and various meteorological fields over the entire modelling domain (Table 2.2.1). Preparing this information requires several pre-processing and pre-modelling steps to translate raw data to final input files for CAMx. Photolysis rates must be calculated using parameters such as albedo, haze, and ozone column for the specific period to be simulated.

The model produces hourly average concentration output files containing the entire three-dimensional fields of user-selected species for each domain. There are also instantaneous fields for each domain containing the three-dimensional concentrations of all species modelled. As the instantaneous concentration files are used for CAMx restarts, the model only writes instantaneous fields for the last two simulation hours. The output deposition file contains two-dimensional deposition parameters such as dry deposition, velocity field, dry deposited mass field, wet deposited mass field, and precipitation liquid concentration for each species. Other output files are mass budget, simulation diagnostic and simulation tracking files.

Since input and output files are in binary format, several programs are used to convert files with different structures from ASCII to binary and vice versa. Post-processing and plotting programs developed by us are used for the evaluation of data.

Table 2.2.1: Data requirements of CAMx

Meteorology (supplied by a meteorological model)	3-dimensional gridded fields -horizontal wind components -temperature -pressure -water vapour -vertical diffusivity -clouds/rainfall
Air Quality (obtained from either measured ambient data or from large-scale models)	gridded initial concentrations gridded boundary concentrations time/space constant top concentrations
Emissions (supplied by an emission model)	gridded sources (anthropogenic and biogenic) elevated point sources
Geographic	gridded land use/surface cover gridded surface UV albedo codes
Other (ozone column from TOMS data, photolysis rates from radiative model)	atmospheric radiative properties -gridded haze opacity codes -gridded ozone column codes -photolysis rates lookup table
Chemistry parameters	chemical information for the simulation and mechanism

2.2.6 CAMx Model setup

The model domains were defined according to the requirements of CAMx and MM5. The mother domain is the same as MM5 coarse domain (domain 1) and has a resolution of 27 km × 27 km. The second domain which has a resolution of 9 km × 9 km, covers Switzerland and partly also the surrounding countries. The third domain over Switzerland has the highest resolution with 3 km × 3 km. There are 14 σ -layers in a terrain-following Lambert Conic Conformal coordinate system that is ideal for mid-latitude domains. They are a sub-set of the 31 σ -layers of MM5. At a surface pressure of 950 hPa the lowest layer thickness is about 40 m. The model top was set at $\sigma = 0.55$, which corresponds to a geometric layer top at sea level of about 7000 m.

CAMx requires hourly concentrations of species along the four lateral boundaries of the coarse domain, for each vertical layer. It also needs 3-dimensional concentration fields at the beginning of the simulation to initialize the model. Another input required by the model is the concentrations at the top of the model domain. This input contains the time- and space-invariant species concentrations that are assumed to exist above the top boundary of the entire modelling grid. These initial and boundary conditions were extracted from the output of the global model MOZART for similar periods (Horowitz, *et al.*, 2003). MOZART has a resolution of 1.895 degrees × 1.875 degrees. The coordinate system (geographic) and the vertical structure are different from those of CAMx. Therefore, the output of MOZART model had to be adjusted to the vertical structure of CAMx before being used for boundary and initial concentration files. The rates of atmospheric photolysis reactions depend upon solar irradiance and therefore are sensitive to the amount of solar radiation transmitted

through the atmosphere as well as reflected from the earth's surface. Photolysis rates were derived for each grid cell as a function of five parameters: solar zenith angle, height above ground, ultraviolet (UV) albedo of the ground, atmospheric turbidity, and total ozone column density. The required ozone column densities were extracted from the TOMS data (NASA/GSFC, 2005). The rates were calculated using the TUV photolysis pre-processor (Madronich, 2002). The chemical mechanism used in this study is the CBM-IV gas-phase mechanism 4 with aerosols. The simulated episodes are 1 January–10 February 2006, 1–30 June 2006, and 1–31 January 2007. Simulations started at 0000 UTC on the first day and ended at 2400 UTC on the last day of the episodes. The concentrations of particles smaller than 2.5 μm in diameter were calculated using the fine/coarse option of CAMx.

For CAMx fine grids, buffer cells must be specified along the boundaries in order to ensure a proper mass exchange between nested domains. Moreover, each fine grid (excluding buffer cells) must exactly fit into an integer number of cells of the coarse grid (see also Sec. 2.1.2). Note that MM5 fine grids are slightly larger than the corresponding CAMx grids, to minimize the influence of the boundaries of the meteorological fields on the corresponding air quality grid.

The following CAMx domains were derived from the MM5 domains:

Coarse grid (domain 1), same as the MM5 grid:

grid cell size	: 27 km \times 27 km
number of cells (no buffer cells)	: 95 \times 79
domain size	: 2565 km \times 2133 km

1st fine grid (domain 2):

grid cell size	: 9 km \times 9 km
number of cells (including buffer cells)	: 74 \times 56
domain size	: 666 km \times 504 km

2nd fine grid (domain 3):

grid cell size	: 3 km \times 3 km
number of cells (including buffer cells)	: 128 \times 92
domain size	: 384 km \times 276 km

vertical layering

14 terrain-following σ -levels

3 Emissions

Air quality models such as CAMx require gridded emission rates at regular time intervals, e.g. 1 h. It is obvious that the emission inventories must include the same species as those specified in the chemical mechanism of the model. Inorganic species are usually given explicitly. Conversely, organic compounds are treated in chemical reaction schemes of various complexities. In order to restrict the number of species, they are lumped into categories according to specific properties such as reaction rate constants. We are using currently the Carbon Bond Mechanism (CBM-IV) (Gery, *et al.*, 1989). This lumped mechanism is based on chemical bonds. Examples are the single (paraffinic, PAR) and the double (olefinic, OLE) bonds. Molecules are split into a specified number of PARs and OLEs according to their number of reactive bonds. For instance, n-butane is represented by 4 PAR, propene by 1 OLE + 1 PAR.

Emission data of these species are hardly ever available in the required format. Raw emission inventories usually report annual data in geographic coordinates or projected to a country specific coordinate system (e.g. the oblique Mercator projection for Switzerland). Moreover, they split the volatile organic compounds (VOCs) into only a few categories, the simplest being methane and the total of non-methane volatile organic compounds (NMVOC).

In this project, the anthropogenic emissions and their projections to specific years are taken from various European data sources described in Section 3.1. For the grid cells located in Switzerland, emissions are replaced by the Swiss data given in Section 3.2. Biogenic emissions are calculated separately. They depend on irradiance and temperature as well as on land cover (Section 3.3).

Gridded emissions refer to a specific year. The European data set, for instance, are available for 2000. To harmonize data from different sources and reference years, emissions have to be converted to a common reference year. Emissions for various countries and years are available as annual totals of different species, split into a number of source categories. On the European level, these totals are available from EMEP (for the past) and from IIASA (for the past and the future). Details are given in Section 3.4.

3.1 European Anthropogenic Emissions

The annual emissions and time functions for Europe were kindly provided by the Freie Universitaet Berlin (FUB). This inventory was jointly developed with the Umweltbundesamt (UBA) and The Netherlands Organisation for Applied Scientific Research (TNO) in the frame of the CITY-DELTA project (Stern, 2003; Bultjes, *et al.*, 2002). The inventory includes TSP, PM₁₀, PM_{2.5}, CH₄, CO, NH₃, NMVOC, NO_x and SO₂ for the source categories as defined in the SNAP (Selected Nomenclature for Air Pollution) classification (Table 3.1.1). Emissions of the category “road traffic” (SNAP 7) are calculated as the sum of the SNAPS 7a, 7b and 7c.

Table 3.1.1: SNAP categories of the European emissions

SNAP	Description
1	public power, cogeneration and district heating plants
2	commercial, institutional and residential combustion
3	industrial combustion and processes with combustion
4	non-combustion production processes
5	extraction and distribution of fossil fuels
6	solvent use
7a	road transport gasoline
7b	road transport diesel
7c	road transport evaporation
8	other mobile sources and machinery
9	waste treatment and disposal
10	Agriculture
11	other sources and sinks (not used in the inventory)

The emission data are available as a gridded inventory extending from 10 deg W to 25 deg E and from 35 deg N to 60 deg N. The spatial resolution is 0.125 deg latitude (~14 km) and 0.25 deg longitude (~19 km at 47 deg N), and the grid size is 140 x 200 grid cells. Reference year is 2000. Seasonal, weekly and diurnal variations are available as well. The diurnal dependence refers to civil time, i.e. Central European Time (CET) in winter and Central European Summer Time (CEST) in summer for most countries. Hence the emission has to be shifted to UTC to be compatible with MM5.

The conversion of the total NMVOC emissions to the CBM-IV split is performed in two steps. First, the NMVOCs of each SNAP category are split in 221 explicit species according to *Passant* (2002). In the second step, each of those species is converted to the CBM-IV substances following the rules provided by ENVIRON.

The region of Lombardy in northern Italy was treated differently. Hourly emission data of the years of interest were interpolated from 1999 and 2010 data provided by the CityDelta project. An extended *Passant* scheme including 426 explicit NMVOC species is available at the CityDelta webpage (*Thunis*, 2002).

3.2 Swiss Anthropogenic Emissions

3.2.1 Road traffic emissions

Annual road traffic emissions of NO_x, CO, NMVOC, toluene, benzene, xylene, PM2.5 and PM10 were prepared by INFRAS on the basis of the emission handbook for road traffic (*Keller and de Haan*, 2004). Data are split into link and zone emissions. The spatial resolution is 250 m; the co-ordinates are based on the Swiss co-ordinate system. Reference year of this inventory is 2000. An average diurnal variation was provided as well (*Heldstab and Wuethrich*, 2006). For the present study the inventory was converted to 2005 taking the projections of the annual emissions published by *Keller and de Haan* (2004).

Since cars in Switzerland have to fulfil the same emission standards as those of EU (Euro standards), the total NMVOC emission was split into the CBM-IV species following the rules of *Passant* (2002) for the SNAP category 7 and of ENVIRON as described above.

3.2.2 Industrial and residential emissions

Annual NO_x, PM_{2.5} and PM₁₀ emissions from residential activities, heating, industry, off-road traffic, rail transport (PM only) and agriculture / forestry on a 200 m resolution were provided by Meteotest. Reference year of those data is 2000. Annual totals of PM₁₀ emissions were split into numerous sub-categories according to *Kropf* (2001) and *Heldstab et al.* (2003). Those emissions include substantial percentages of biomass burning. About 75 % of the residential PM₁₀ emissions, 10 % of the industrial and 23 % of the agricultural and forestal emissions are released by biomass combustion. The data were converted to 2005 using the projections published in *BUWAL* (1995).

Spatial distributions of total annual NMVOC emissions from industry and household were also provided by INFRAS (*Heldstab and Wuethrich*, 2006). The split into the explicit speciation according to the scheme of Passant and the conversion to CBM-IV was performed on the basis of a survey of different sources such as paint production, paint use, printing industry, solvent use, etc. (*Schneider*, 2007).

3.2.3 Other emissions

Ammonia is released mainly by manure, followed by waste treatment and road traffic. Meteotest provided annual NH₃ emissions for 2000 on a 1 km grid.

3.3 Biogenic Emissions

The most abundant biogenic species in Switzerland are monoterpenes, which are emitted mainly by Norway spruce and fir trees. Less abundant, but much more reactive is isoprene emitted predominantly by oak trees and, to a lesser extend, by spruce and pasture. NO emissions are caused by bacteriological decomposition in soils. Monoterpene and NO emissions are temperature dependent, whereas the isoprene release is a function of both temperature and shortwave irradiance. In *Andreani-Aksoyoğlu and Keller* (1995) and *Keller, et al.* (1995) a method for the estimation of biogenic emissions is given. Gridded biogenic emissions were calculated directly for the CAMx domains. Land use and meteorological data are required for each domain.

As a first guess, global land use data on a 30" grid were downloaded and converted by the MM5 pre-processors to the domains of interest. Those data were then replaced by the Global Land Cover inventory GLC2000. For each European country the deciduous and coniferous forest fractions were split into the tree species mentioned above according to *Simpson, et al.* (1999). Inside the Swiss border the global data were replaced by data of the "Arealstatistik" (100 m resolution) issued by the Federal office of Statistics (*BFS*, 1999) and by forest data (1 km resolution) taken from the "Landesforstinventar" (*Mahrer and Vollenweider*, 1983). The latter includes the land cover of 10 different tree species, in particular spruce, fir and oak. About 24% of the Swiss area is covered with forests, of which 71% are coniferous. Norway spruce and fir are the most abundant species (67 and 20 % of the coniferous forests, respectively). Conversely, oak trees contribute only 8% to deciduous trees. Gridded temperature and shortwave irradiance data were extracted from the MM5 output.

3.4 Conversion of the emissions to the CAMx grids

First, we converted the European emission inventory to the CBM-IV mechanism as described in Sec. 3.1. Subsequently the geographic coordinates were transformed to the lambertian coordinates of each CAMx domains. For those grid cells located within the Swiss boundaries, the European values were replaced by the Swiss emission data. Anthropogenic emissions of a given CAMx grid cell were calculated by computing the geographic (or Swiss) co-ordinates of the 4 corners and the totals of the European (or Swiss) emission rates within the respective polygons. The emissions of the Lombardy Region were inserted in a similar way. Biogenic emissions do not need to be converted since they are already based on the meteorological grids.

The seasonal, weekly and diurnal variations of the European emissions released by the 10 SNAP source categories were taken into account by applying the time functions included in the TNO/FUB/UBA inventory. For Switzerland, the seasonal dependence of residential and industrial emissions, the weekly variation of industry, and the diurnal patterns of residential, industrial and road traffic emissions were replaced by data provided by INFRAS, if available (Sec. 3.2).

4 Model performance evaluation

4.1 General

Validation of a model refers to the general comparison of modelled results against observations carried out by the model developers. However, the validation by model developers is unlikely to have been undertaken in the area being considered by modellers. Therefore, it is necessary to perform a comparison (often called verification) of modelled results versus any local measurements at relevant locations. Both graphical and statistical performance measures are recommended for modelling studies (*USEPA*, 1991; *EPA*, 2005; *Schlünzen*, 2008). These measures should be applied for modelling results beginning on the second day of the modelling episode. The first day is eliminated to mitigate the effects of initial conditions.

Graphical displays provide important information on qualitative relationships between predicted and observed variables. The recommended graphical displays for each episode are time-series plots, ground-level isopleths, and scatter plots of predictions and observations. The time-series plot depicts the hourly predicted and observed quantities for the simulation period. The time series reveals the model's ability to reproduce the peak prediction, the presence of any significant bias within the diurnal cycle and a comparison of timing of the predicted and observed maxima. Ground-level isopleths display the spatial distribution of predicted variables at a selected hour. In the case of air quality data they provide information on the magnitude and location of predicted pollutant plumes. Scatter plots of predictions and observations depict the extent of bias and error in the hourly prediction-observation pairs. The systematic positioning of data points above or below the perfect correlation line indicates the bias. The dispersion of points is a measure of the error in the simulation. The scatter plots also reveal outlier prediction-observation pairs.

Statistical performance measures can provide meaningful measures of model accuracy for dense monitoring networks. A variety of such measures were proposed in the past. The applicability depends on the variable to be assessed. For instance, wind vectors or temperature cannot be evaluated by the same statistical quantities as concentrations (see Sec. 4.2 and 4.3).

4.2 Meteorology

Time series of hourly wind speed, wind direction, air temperature, specific humidity, global irradiance, precipitation rate and planetary boundary layer height are plotted for 24 ANETZ stations together with MM5 simulations and, if available, COSMO 7 analyses. Those stations cover the main climatic regions of Switzerland (Table 4.2.1). Note that COSMO 7 data is taken from the 3h input files for MM5 i.e. not from the original COSMO 7 data. Those files do not include global irradiance and precipitation. Planetary boundary layer height simulations of MM5 at Payerne are compared with the convective boundary layer (CBL) height calculated from radio soundings on the basis of the “parcel” method (*Seibert, et al.*, 2000). Note that this approach is different from that implemented in MM5 and that the conditions are fulfilled only if the boundary layer is under unstable conditions. Despite this restriction the CBL height is given for all 3 episodes. Plots for 6 exemplary stations during the 3 episodes are given in the Appendix.

Concerning the statistical analysis of the time series, there are mainly 2 variable types, which have to be treated differently. The definitions of the statistical measures

used in the evaluation are given in Table 4.2.2. Note that often different terms are in use for the same measure.

- **scalars:** the performance of temperature, specific humidity, global irradiance and absolute wind velocity are characterized by the Mean Bias Error MBE, the Mean Gross Error MGE and the correlation coefficient r . In principle, the normalized errors defined in Sec. 4.3 could also be used. However, for temperature scales with offsets (e.g. deg C) this normalization makes no sense. The significance of MBE to be different from zero on a 95 % confidence level using Student's t-distribution is also estimated.
- **vectors:** the deviation of the simulated wind vectors from the measurements is characterized by the Direction Weighted Wind Error DIST. The calculation of the error of wind direction is not trivial because of the discontinuity at $0 / 360^{\circ}$. To overcome this difficulty we calculate the MBE after having transformed the angular difference such that it is always in the range $0-180^{\circ}$. Note that in this case $MBE = MGE$ holds.

The statistical measures are calculated for 24 h a day, except for the global irradiance G where only values during daylight ($G > 50 \text{ W m}^{-2}$) are considered

In their meso-scale model inter-comparison covering different domains of the world, Cox *et al.*, (1998) suggest the following desired accuracy: 2°C for temperature, 2°C for dew point depression, 1 m s^{-1} and 2.5 m s^{-1} for wind speeds $< 10 \text{ m s}^{-1}$ and $> 10 \text{ m s}^{-1}$, respectively, and 30° for wind direction.

In this study the Root Mean Square Error RMSE is not used for the analysis of meteorological quantities since it gives too much weight to outliers. In a strict sense it is applicable only for normally distributed variables.

The performance of MM5 is evaluated on the basis of simulations and measurements at 24 ANETZ stations located throughout whole Switzerland (Table 4.2.1). As an option, exposed mountain stations (DOL, CHA, MLS, JUN, PIL, COV, CIM) and stations with non-representative time patterns (DIS, PIO, SBE located in the catchment area of the respective valley) are disregarded, i.e. 14 stations are left for the analysis. The statistical quantities of each meteorological variable of interest can be calculated for the total of all stations and time steps or for each station separately. In the former case the analysis yields the average model performance relevant to the whole country.

In Sections 5 – 7 we show the evaluation results for each period of the 3 episodes to show differences between different weather regimes.

4.3 Air quality

The most common statistical parameters used to evaluate regional air quality models are given in Table 4.3.1. There are some parameters defined especially for ozone by the USEPA (1991) such as mean normalized bias error (MNBE) and mean normalized gross error (MNGE). It is recommended that these measures lie in the following ranges: $MNBE \pm 5-15 \%$, $MNGE 30-35 \%$. However, no such performance guidance has been developed for PM models yet. Boylan and Russell (2006) proposed the use of mean fractional error (MFE) and mean fractional bias (MFB) as PM model performance measures. They recommended model performance goals and criteria. Performance goals are defined as the level of accuracy that is considered to be the best a model can be expected to achieve in that application. According to their definition, a model performance goal has been met when both MFE and MFB are less than or equal to $+50\%$ and $\pm 30\%$, respectively. Performance

criteria, on the other hand, are defined as the level of accuracy that is considered to be acceptable for standard modelling applications. The model performance criteria have been met when both the MFE and MFB are less than or equal to +75% and $\pm 60\%$, respectively.

Table 4.2.1: ANETZ stations used in the evaluation of MM5

ANETZ station	Acronym	Region	Altitude (m a.s.l.)	location
Fahy	FAH	north of Jura	596	plain
Basel-Binningen	BAS	north of Jura	316	plain
La Dole	DOL	Jura	1670	mountain peak
Chasseral	CHA	Jura	1599	mountain peak
Geneva	GVE	Swiss Plateau	420	plain
Payerne	PAY	Swiss Plateau	490	plain
Bern	BER	Swiss Plateau	565	plain
Buchs	BUS	Swiss Plateau	387	plain
Zurich Airport	KLO	Swiss Plateau	436	plain
St. Gallen	STG	Swiss Plateau	779	plain
Molésón	MLS	Alps	1972	mountain peak
Jungfrauoch	JUN	Alps	3580	mountain peak
Pilatus	PIL	Alps	2106	mountain peak
Corvatsch	COV	Alps	3315	mountain peak
Sion	SIO	Alps	482	valley
Disentis	DIS	Alps	1190	valley
Chur-Ems	CHU	Alps	555	valley
Samedan	SAM	Alps	1705	valley
Cimetta	CIM	southern Switzerland	1672	mountain peak
Magadino	MAG	southern Switzerland	197	valley
Lugano	LUG	southern Switzerland	273	valley
Stabio	STA	southern Switzerland	353	valley
Piotta	PIO	southern Switzerland	1007	valley
San Bernardino	SBE	southern Switzerland	1639	valley

In this study, we evaluated the model performance by means of graphical as well as statistical parameters. The graphical tools used for each episode are time series, ground-level isopleths and modelled versus observed concentrations. The model results for the three studied episodes were evaluated also using the statistical measures given in Table 4.3.1. Only daytime data between 8:00 and 18:00 were used to evaluate ozone statistics and the first day was eliminated to avoid the effects of initial conditions, as mentioned before.

Table 4.2.2: Statistical measures used for the evaluation of meteorological models (EPA, 2005; Schlünzen, 2008) $x_{mod}(i)$: modelled data, $x_{obs}(i)$: observed data.

Mean Bias Error, MBE	$MBE = \frac{1}{N} \sum_{i=1}^N (x_{mod}(i) - x_{obs}(i))$
Mean Gross Error, MGE	$MGE = \frac{1}{N} \sum_{i=1}^N x_{mod}(i) - x_{obs}(i) $
Mean Bias Error, MBE, of the transformed wind direction DD	$MBE = \frac{1}{N} \sum_{i=1}^N (DD_{mod}(i) - DD_{obs}(i))$
Direction Weighted Wind Error, DIST	$DIST = \frac{1}{N} \sum_{i=1}^N \sqrt{(u_{mod}(i) - u_{obs}(i))^2 + (v_{mod}(i) - v_{obs}(i))^2}$
Correlation coefficient, r	$r = \frac{\sum_{i=1}^N (x_{mod}(i) - \bar{x}_{mod}) \times (x_{obs}(i) - \bar{x}_{obs})}{\sqrt{\sum_{i=1}^N (x_{mod}(i) - \bar{x}_{mod})^2} \times \sqrt{\sum_{i=1}^N (x_{obs}(i) - \bar{x}_{obs})^2}}$

Table 4.3.1: Statistical formulation of evaluation indexes (N is the number of effective data in the period without the spin-up day, $C_{mod}(t)$ and $C_{obs}(t)$ are the simulated and observed concentrations at time t , respectively) (Boylan and Russell, 2006; USEPA, 1991).

Mean Normalized Bias Error, $MNBE$	$MNBE = \frac{1}{N} \sum_{t=1}^N \frac{C_{mod}(t) - C_{obs}(t)}{C_{obs}(t)} \times 100$
Mean Normalized Gross Error, $MNGE$	$MNGE = \frac{1}{N} \sum_{t=1}^N \frac{ C_{mod}(t) - C_{obs}(t) }{C_{obs}(t)} \times 100$
Root Mean Square Error, $RMSE$	$RMSE = \sqrt{\frac{1}{N} \sum_{t=1}^N (C_{mod}(t) - C_{obs}(t))^2}$
Correlation coefficient, r	$r = \frac{\sum_{t=1}^N (C_{mod}(t) - \bar{C}_{mod}) \times (C_{obs}(t) - \bar{C}_{obs})}{\sqrt{\sum_{t=1}^N (C_{mod}(t) - \bar{C}_{mod})^2} \times \sqrt{\sum_{t=1}^N (C_{obs}(t) - \bar{C}_{obs})^2}}$
Mean Fractional Bias, MFB	$MFB = \frac{1}{N} \sum_{t=1}^N \frac{C_{mod}(t) - C_{obs}(t)}{(C_{obs}(t) + C_{mod}(t))/2} \times 100$
Mean Fractional Error, MFE	$MFE = \frac{1}{N} \sum_{t=1}^N \frac{ C_{mod}(t) - C_{obs}(t) }{(C_{obs}(t) + C_{mod}(t))/2} \times 100$

5 Episode 1: January-February 2006

5.1 Meteorology

The meteorological conditions during January-February 2006 were analysed and classified using time series of measurements taken at ANETZ and NABEL stations together with simulations performed with MM5 and CAMx.

Figures 5.1.1 and 5.1.2 show time series of measured and modelled wind direction and wind speed, air temperature, precipitation and CO mixing ratios at the NABEL stations Zurich and Payerne, respectively. Based on the agreement of model CO concentrations with observations we divided the episode in 5 periods:

Period I: 1-5 January

Period II: 6-16 January

Period III: 17-22 January

Period IV: 23 January-4 February

Period V: 5-9 February

Carbon monoxide has been chosen as a proxy for quantifying air mass transport since the chemical reaction of CO with OH is relatively slow and the concentrations are not affected considerably by this reaction. The model predictions and measurements of CO during period I, III and V are very similar. In period II and IV, however, the model performance with severe underestimation of the observed values is insufficient.

The meteorological parameters also have different characteristics in those five periods. During period I a cyclone moved from the North Sea to southern Italy. Air temperatures in the Swiss Plateau were above zero, wind speed was moderate and there was no precipitation except at the very beginning. The model predicted wind speed quite well except on 4 January where the modelled wind speed was higher. An analysis of the Alpine Weather Statistics (AWS) (*Wanner, et al.*, 1998) and synoptic charts produced by Global Forecast System (GFS) of National Centers for Environmental Prediction (*NCEP*, 2004; *Wetterzentrale*, 2008) yields that the high pollution episode of period II was either associated with an anticyclone over central Europe or with indifferent conditions which favoured low wind speed and an extended fog layer over the Swiss Plateau (Figure 5.1.3). Comparison of surface values and vertical profiles of meteorological parameters with observations show that surface values are predicted reasonably well (Figures 5.1.1 and 5.1.2). During stagnant conditions, however, MM5 fails to capture the structure of the atmospheric boundary layer. The comparison of MM5 model results with the vertical profiles of potential temperature from soundings at Payerne shows clearly that the model cannot reproduce the temperature inversions during the Periods II and IV (Figure 5.1.4). This in turn implies that vertical mixing is not well captured.

Period II was terminated by the passage of a warm front which resulted in precipitation, higher wind speed and a fast increase of temperature. The increased wind speed and precipitation during the following period III resulted in low air pollution levels. Period III was followed by another pollution episode between 23 January and 5 February (Period IV). AWS data for the synoptic conditions varied between indifferent, southerlies, easterlies and anti-cyclonic. As seen on GFS reanalysis (Figure 5.1.5), this was the result of the balance between a low-pressure

weather system over the Iberian Peninsula or West Mediterranean and a ridge from Western to Eastern Europe. Switzerland being in between these two systems, experienced weak winds in the directions between south and east. Concentrations of CO reached even higher levels in period IV compared to period II. Therefore, it is interesting to examine in the future whether the aforementioned weather conditions of period IV cause high pollution episodes in general, in addition to pure anti-cyclonic conditions. Finally, period V was increasingly influenced by a cyclonic situation over the Mediterranean Sea coupled with a subsidence of the 500 hPa geopotential leading to a steady decrease of the pollution levels. The period was terminated by moderate precipitation.

A common element between periods II and IV is temperature inversions (Figure 5.1.4). The temperature inversions were further investigated by examining the difference of the potential temperature (hereafter denoted as dTp) between Payerne (NABEL) and Chaumont (MeteoSwiss). These stations are in a relatively close distance to each other (about 25km) and the elevation in Chaumont is about 650m higher than in Payerne. Thus the difference of the potential temperature can be used as a proxy for detecting the presence of a temperature inversion. As shown in figure 5.1.6, there was a sharp decrease of dTp at the beginning of period II. At the end of that period dTp increased abruptly. We should note that an equally sharp decrease of dTp by about 10°C was also observed in period IV. This implies the development of a temperature inversion. At the end of period IV when pollution levels were lower, dTp increased abruptly by 12 °C approximately. The contrast between low-wind periods (II and IV) and high-wind periods (III and V) can be seen clearly. As seen in the figure, MM5 does not follow the observations. This result probably reflects an inadequate estimation of the vertical structure of the atmosphere and it is consistent with the findings from the comparison of simulated and observed profiles of potential temperature (Figure 5.1.4).

The elevated pollution levels in periods II and IV were also investigated from the point of view of the origin of air pollution. It is often hypothesized that air pollution episodes in Switzerland are associated with import of pollutants from abroad, in particular from Po Basin, which is one of the most heavily polluted areas in Europe. The HYbrid Single-Particle Lagrangian Integrated Trajectory Model (HYSPLIT) (*Draxler and Rolph, 2008*) driven by Global Data Assimilation System (GDAS) Environmental Modeling Center data with resolution of approximately 0.7×0.7 degrees was used in order to investigate this hypothesis. Figure 5.1.7 shows an example of backward trajectories from 1 February at 00:00LT (Period IV) where the highest peak of CO in January-February 2006 was observed. No influence from Po Basin can be seen in that case. It should be noted that the presence of the Alps between the Po Basin and the Swiss Plateau reduces direct exchange of air between these two areas, especially at low heights in the atmosphere. In general, examination of numerous trajectory plots for periods II and IV did not reveal any pollutant transport from Po Basin. However, even if there is a considerable transport of pollutants from Po Basin, it is very difficult to simulate it in trajectory models because very high-resolution data are required in order to accurately simulate the atmospheric circulation in Alpine regions. On the other hand, some transport from coal combustion sources in Poland could be expected, but there is no strong evidence for that either.

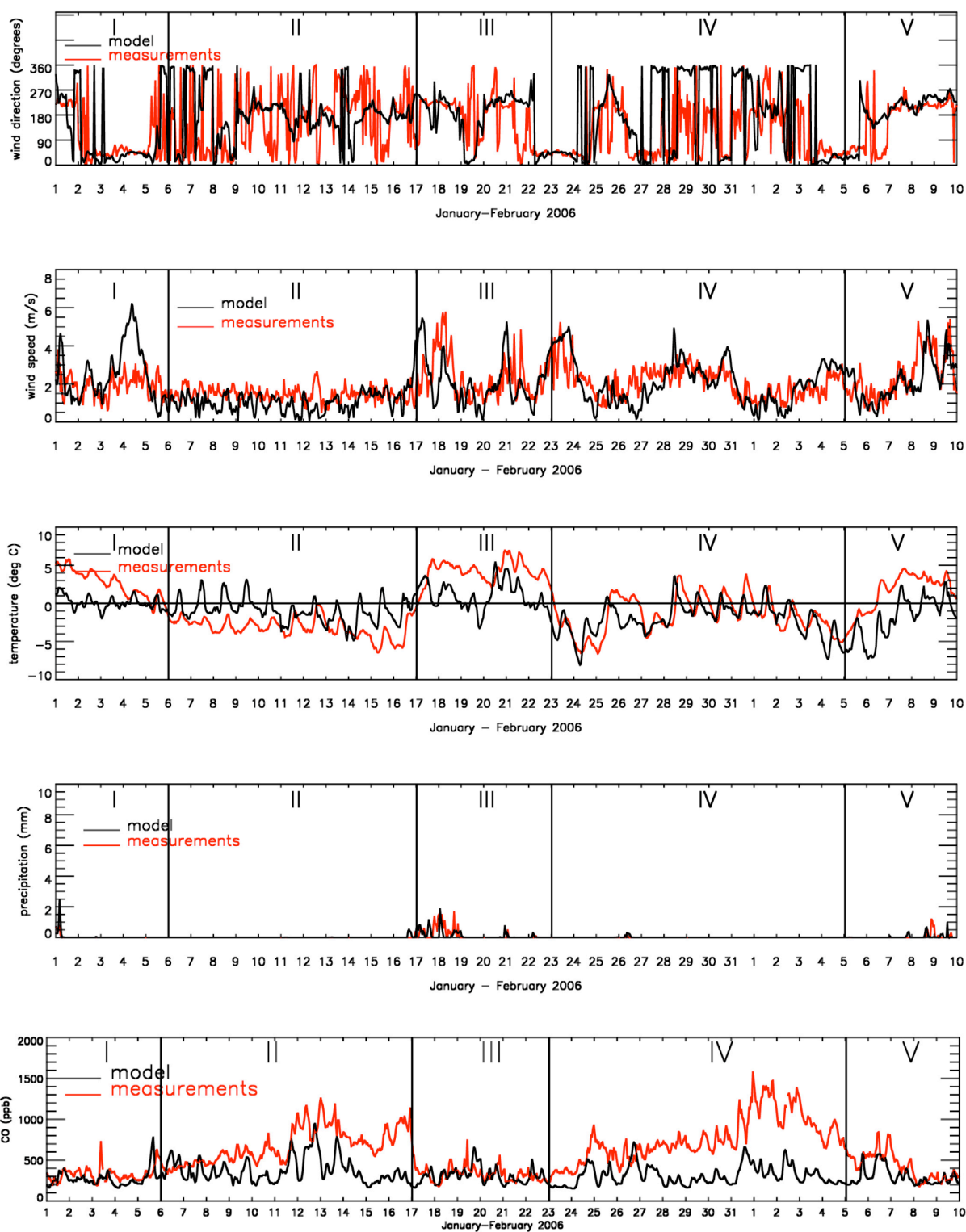


Figure 5.1.1: Comparison of measured and modelled wind direction (degrees), wind speed (m s^{-1}), air temperature (C), precipitation (mm) and CO concentrations (ppb) at Zurich (NABEL station) in January-February 2006.

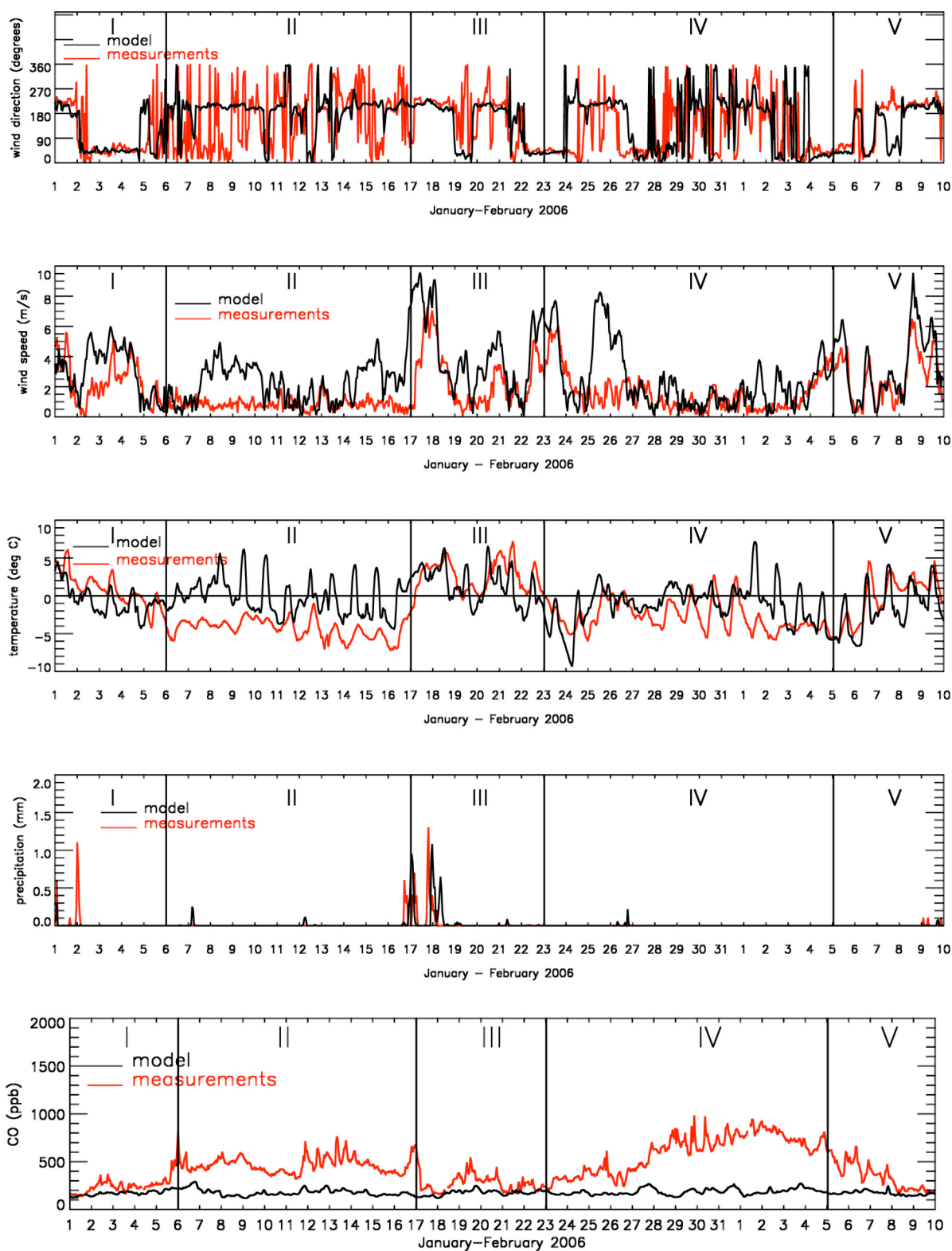
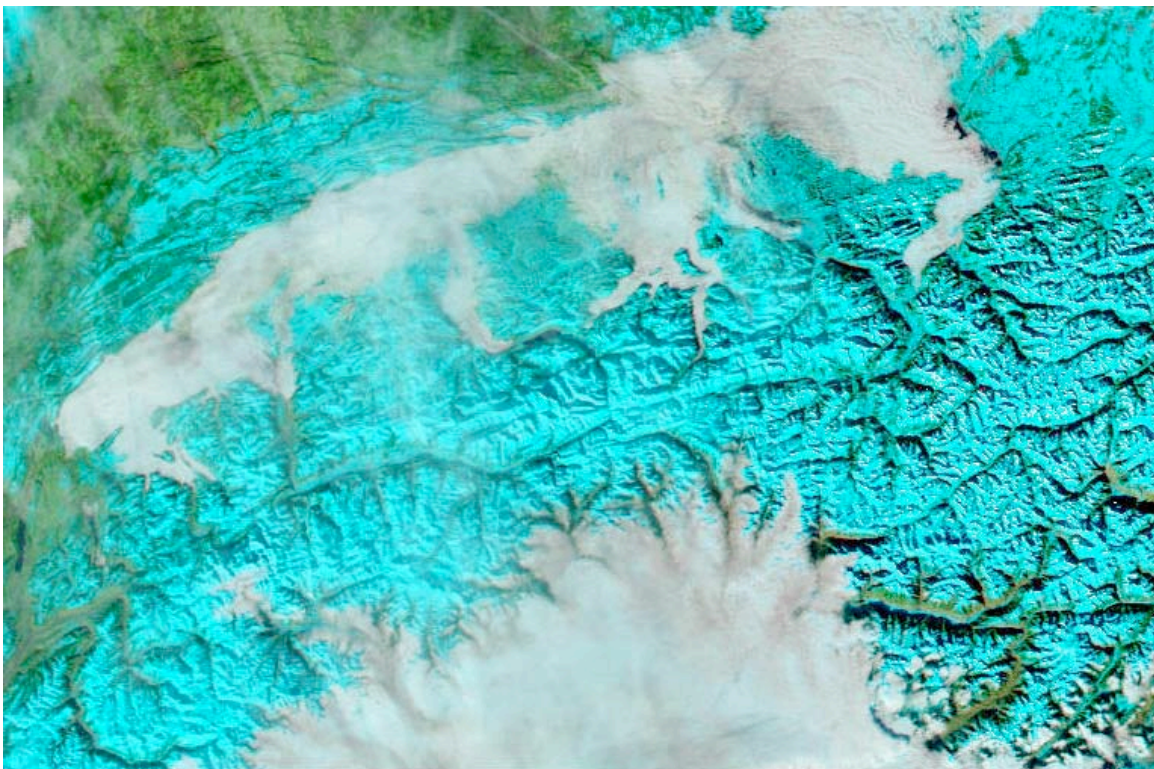
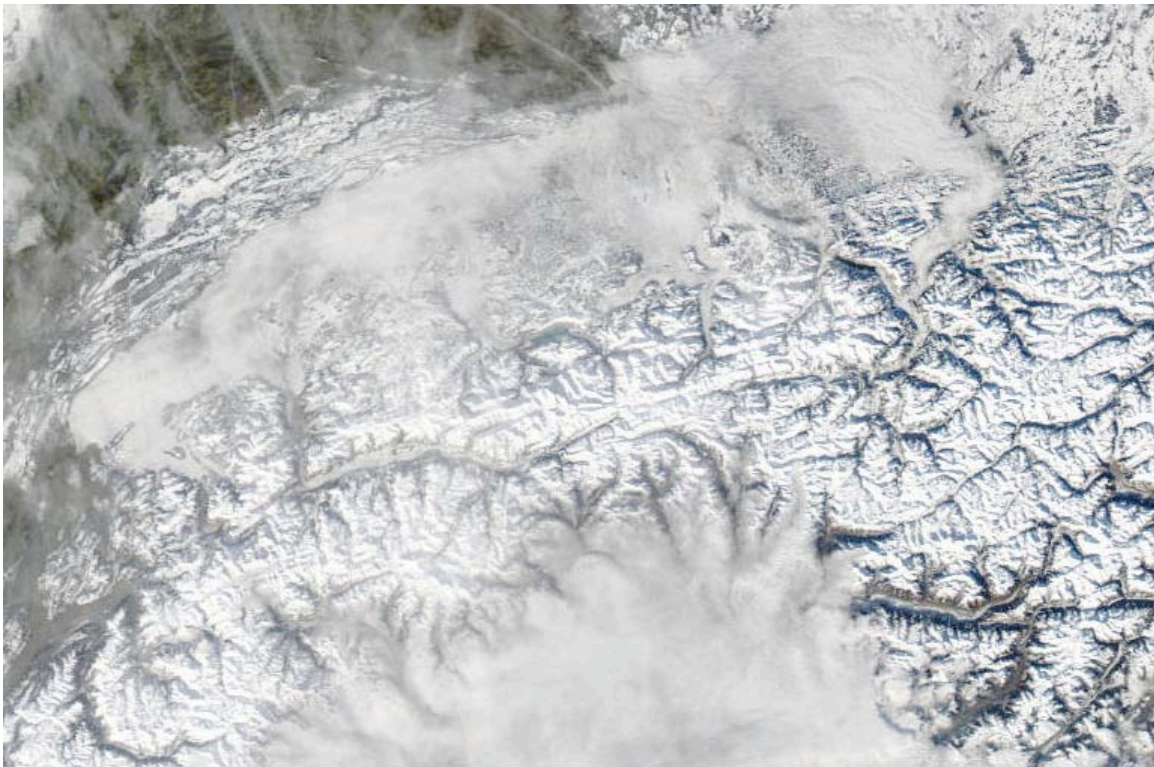
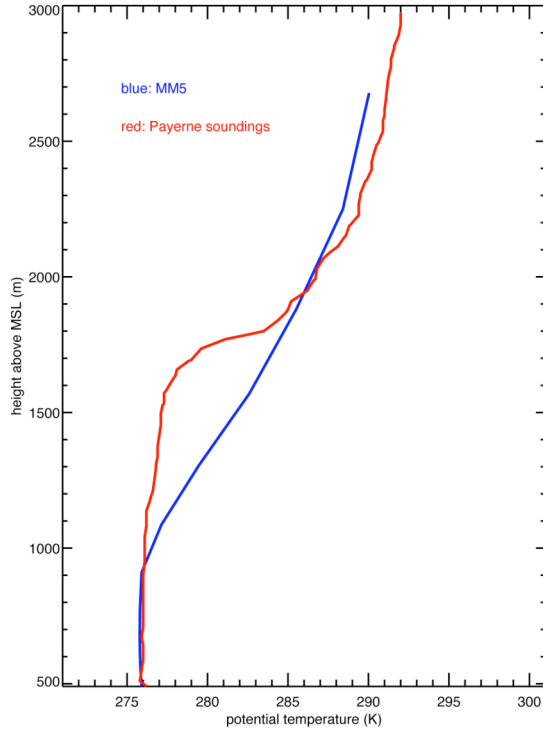


Figure 5.1.2: Comparison of measured and modelled wind direction (degrees), wind speed (m s^{-1}), air temperature (C), precipitation (mm) and CO concentrations (ppb) at Payerne (NABEL station) in January-February 2006.

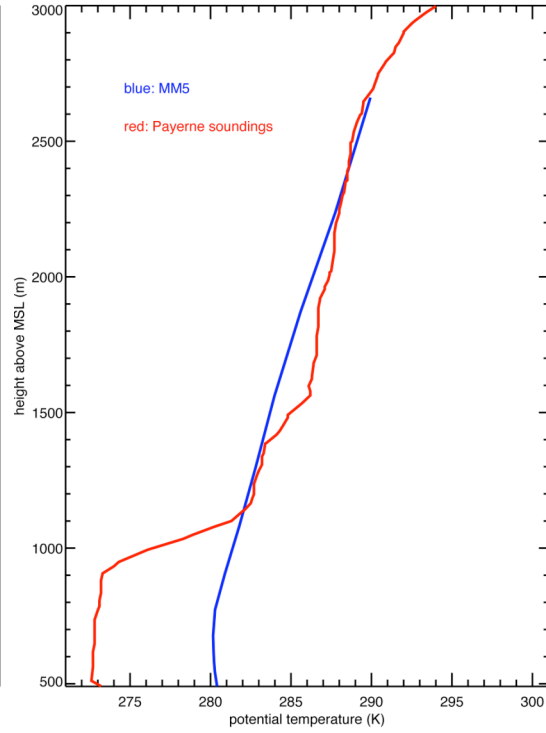


*Figure 5.1.3: Extended fog layers (“Hochnebel”) above the Swiss Plateau and the Po Basin. MODIS overpass on 8 January 2006. Top: RGB, bottom: false colour.
Source: MODIS Rapid Response System, <http://rapidfire.sci.gsfc.nasa.gov/subsets/>*

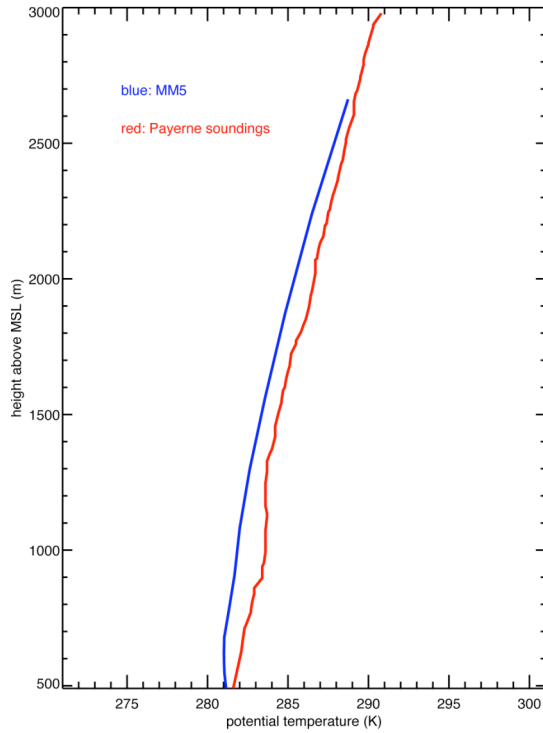
a) 4 January 2006 (Period I)



b) 9 January 2006 (Period II)



c) 18 January 2006 (Period III)



d) 3 February 2006 (Period IV)

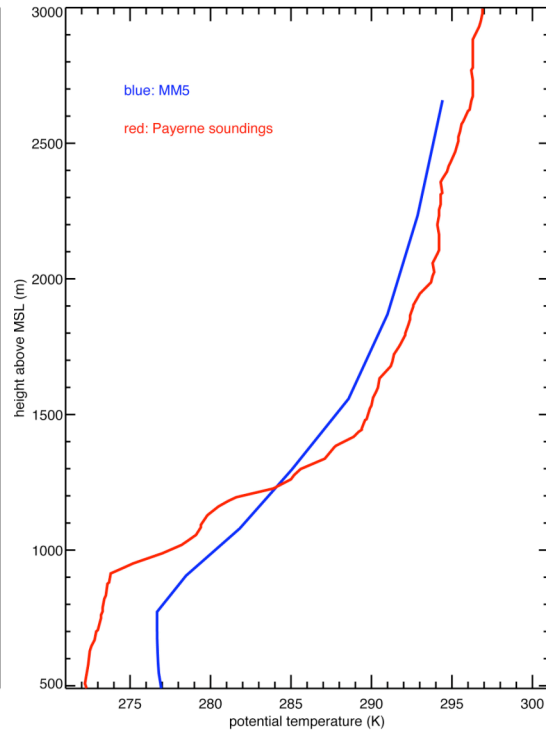


Figure 5.1.4: The comparison of vertical profiles of potential temperature (K) from soundings at Payerne (red) and from MM5 meteorological model (blue) in January 2006. a) 4 January (period I), b) 9 January (period II), c) 18 January (period III), d) 3 February (period IV).

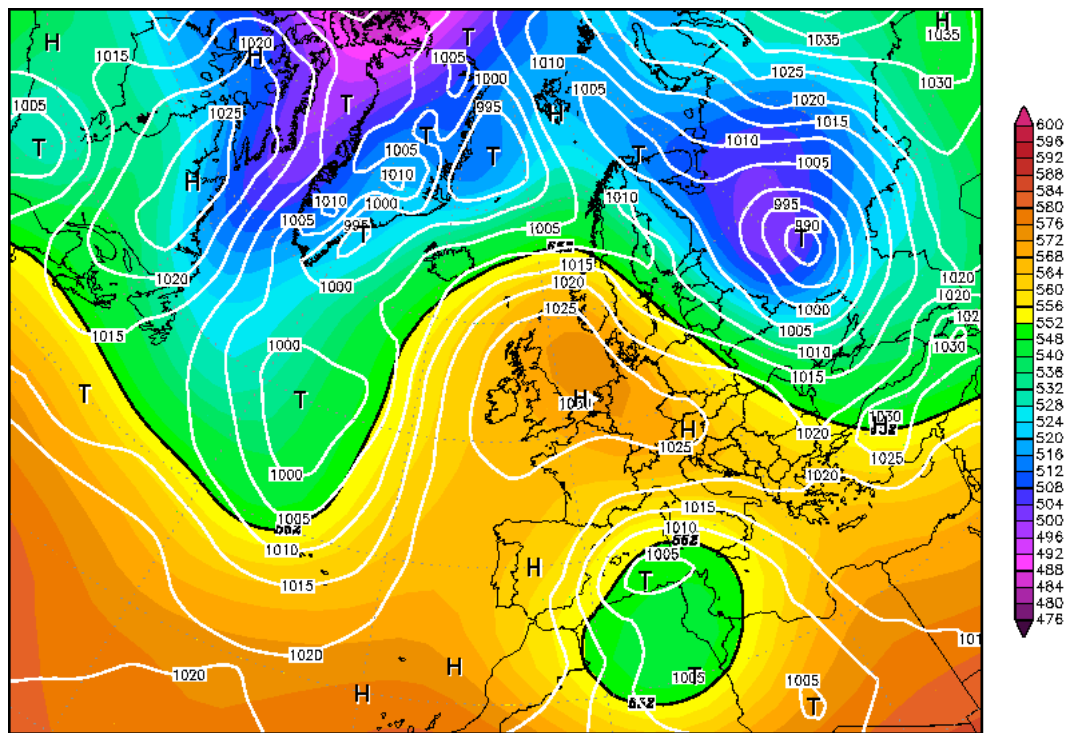


Figure 5.1.5: 500hPa geopotential (gpdm) and surface pressure (hPa) on 31 January 2006 at 00:00 UTC. An abrupt increase of CO concentrations was recorded a few hours later. The combination of a cyclone over the West Mediterranean and high pressure over Europe results in 'easterlies' weather over Switzerland. Reanalysis of NCEP. Courtesy Wetterzentrale, www.wetterzentrale.de

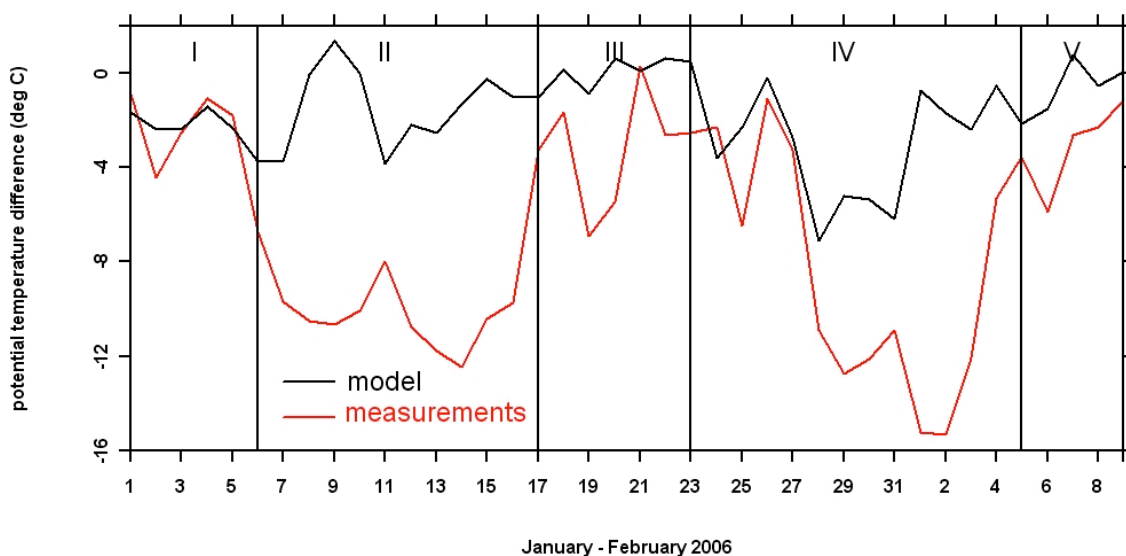


Figure 5.1.6: Temperature difference between measurements at Payerne (NABEL) and Chaumont (MeteoSwiss) as well as model results during January–February 2006 (data at 12:00 UTC).

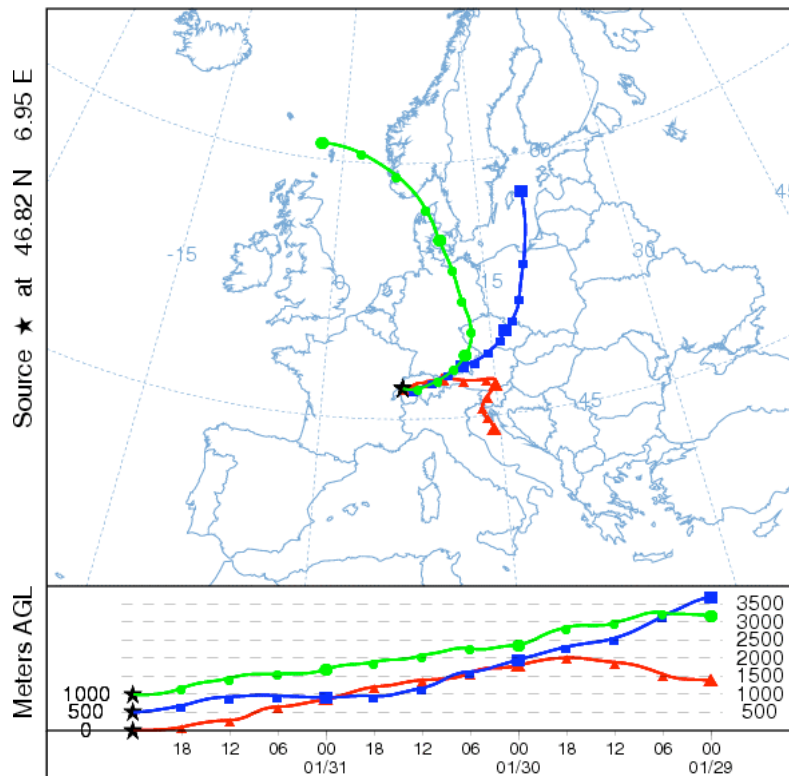


Figure 5.1.7: Backward trajectory plot from HYSPLIT model driven by GDAS meteorological data. The end time is midnight of 1 February 2006.

The agreement of model results and observations should not be based on only one or two locations of interest, but on measurements taken at as many representative sites as possible (see also Section 4). A first impression of the model performance may be obtained by a visual inspection of time series. As examples, Figures A1 to A7 in the Appendix show the time series of surface wind speed, wind direction, air temperature, specific humidity, global irradiance, planetary boundary layer height, and precipitation rate at CHA, PAY, KLO, STG, SIO and MAG for domain 3. Blue stands for hourly ANETZ observations or for convective boundary layer CBL height, green for 3 hourly COSMO 7 simulations (taken from the MM5 input file) and red for hourly MM5 simulations. Note that COSMO 7 data are reanalyzed using numerous weather stations over whole Europe, whereas the MM5 fields were nudged with COSMO 7 data only in domain 1 and 2. Moreover, COSMO 7 fields in MM5 input files do not include global irradiance, planetary boundary height and precipitation although they are available in the original COSMO 7 files because those variables are not used for initialization and FDDA. In general, the degree of agreement depends on the location, the time and the variable of interest. For instance, wind speed at the mountain station CHA is strongly under-predicted by both models. At KLO the agreement is quite good. Apparently, COSMO 7 performs better than MM5 due to the reanalysis of COSMO 7 data. Wind direction is fairly well captured by the models at high wind conditions, but may substantially differ from measurements when the boundary layer is stable. Temperature and specific humidity agree well with measurements most of the time. Global irradiance from MM5 agrees fairly well only at higher altitudes, i.e. above fog and cloud layers. Rain rate is captured surprisingly well by MM5. Finally, the planetary boundary layer (PBL) height is an indicator of the volume air pollutants are confined within. During low wind periods PBL height is often

zero. CBL heights at Payerne calculated according to the “parcel” method are nearly always greater than the modelled PBL heights.

In the first step of statistical evaluation, the mean bias, the mean error, the correlation coefficient and the direction weighted wind error DIST (see Section 4) were calculated for whole January (Table 5.1.1). The analysis was performed for all 3 domains using the reduced set of 14 stations to check the influence of the spatial resolution. The full set of 24 stations in domain 3 was used to estimate the performance if non-representative stations are included. The outputs for domain 1 and 2 of the two models are close together due to the strong nudging of MM5 with COSMO 7 reanalysis data. This is true for all investigated variables. For domain 3, however, the performance of MM5 (forecast run without FDDA) for wind was worse. Temperature and specific humidity were slightly higher correlated for MM5 compared to COSMO 7. The inclusion of 24 stations increased the mean error of wind speed. Scalar quantities were hardly affected by the number of stations. The following ranges of the correlation coefficient were found (Table 5.1.1): 0.38 - 0.54 for wind speed, 0.59 – 0.74 for temperature, 0.68 – 0.81 for specific humidity and 0.47 – 0.53 for global irradiance. The MBE of wind speed, temperature, specific humidity and global irradiance significantly differ from zero (at a confidence level of 95 %).

The periods of January - February episode were investigated separately in the second step to detect changes in the associated statistical measures (Table 5.1.2) Note that period IV is split into 2 sub-periods because each month is analyzed separately. Modelled wind speeds are quite well correlated with measurements during the periods I, III and VI, whereas the performance in the low wind period II is worse. The MBE is mostly less than the desired accuracy of 1 m s^{-1} (Cox, *et al.*, 1998), whereas MGE is slightly above. COSMO 7 wind speeds perform better than MM5 results since those fields are reanalyzed. Similar features are evident for MGE. On the average, the MBE of the wind direction is very large, roughly between 50° and 80° , thus significantly greater than the desired value of 30° . This bias is smaller for high wind speed periods. COSMO 7 data are slightly less biased than the data from MM5. Note that a grid spacing of 46 km and partly flat domains were specified in the study of Cox *et al.* (1998), hence the small-scale variations of wind direction is supposed to be much smaller than over a complex topography and for grid resolutions of a few kilometres. The range of DIST is $2.06 \leq \text{DIST} \leq 2.72 \text{ m s}^{-1}$ and $1.36 \leq \text{DIST} \leq 1.80 \text{ m s}^{-1}$ for MM5 and COSMO 7 simulations, respectively (roughly between 90 and 180 % relative to the mean observations).

Modelled and observed temperatures agree at a fairly good level, the correlation coefficient being around 0.5 for period II and mostly above for the rest of the time. MBE is mostly within the $\pm 2^\circ\text{C}$ interval except for MM5 simulations during the periods II and V. MGE is within $\pm 4^\circ\text{C}$. Specific humidity correlates well for nearly every period and model (about $0.5 < r < 0.8$). The MBE, although statistically significant, is small and hardly depends on the time period. Finally, the irradiance has a high spatial and temporal variability, which is not fully captured by MM5. This is partly due to the insufficient capability to model fog and low-level clouds.

Table 5.1.1: Mean bias error MBE and its 95% confidence interval (Δ MBE), mean gross error MGE, correlation coefficient r and direction weighted wind error DIST of modelled vs. measured meteorological quantities measured at selected ANETZ stations. January 2006, domain 3. FFSFC: wind speed (m s^{-1}), DDSFC: wind direction ($^{\circ}$), UVSFC: wind vector (for dist) (m s^{-1}), TSFC: air temperature ($^{\circ}\text{C}$), QSFC: specific humidity (kg kg^{-1}), G: global irradiance (W m^{-2}). The desired accuracy: 2°C for temperature, 1 m s^{-1} for wind speeds, 30° for wind direction. See text for details.

variable	domain	model	# stations	MBE	Δ MBE	MGE	r	DIST
FFSFC	1	MM5	14	0.20	0.03	1.03	0.48	n.a.
FFSFC	1	COSMO	14	0.22	0.05	1.08	0.46	n.a.
FFSFC	2	MM5	14	0.33	0.03	1.05	0.51	n.a.
FFSFC	2	COSMO	14	0.27	0.05	1.05	0.54	n.a.
FFSFC	3	MM5	14	0.94	0.05	1.66	0.34	n.a.
FFSFC	3	COSMO	14	0.35	0.05	1.01	0.57	n.a.
FFSFC	3	MM5	24	0.29	0.06	2.70	0.38	n.a.
FFSFC	3	COSMO	24	-1.11	0.09	2.33	0.37	n.a.
DDSFC	1	MM5	14	62.2	n.a.	62.2	n.a.	n.a.
DDSFC	1	COSMO	14	66.6	n.a.	66.6	n.a.	n.a.
DDSFC	2	MM5	14	62.0	n.a.	62.0	n.a.	n.a.
DDSFC	2	COSMO	14	63.0	n.a.	63.0	n.a.	n.a.
DDSFC	3	MM5	14	70.2	n.a.	70.2	n.a.	n.a.
DDSFC	3	COSMO	14	63.2	n.a.	63.2	n.a.	n.a.
DDSFC	3	MM5	24	69.4	n.a.	69.4	n.a.	n.a.
DDSFC	3	COSMO	24	62.8	n.a.	62.8	n.a.	n.a.
UVSFC	1	MM5	14	n.a.	n.a.	n.a.	n.a.	1.67
UVSFC	1	COSMO	14	n.a.	n.a.	n.a.	n.a.	1.75
UVSFC	2	MM5	14	n.a.	n.a.	n.a.	n.a.	1.69
UVSFC	2	COSMO	14	n.a.	n.a.	n.a.	n.a.	1.67
UVSFC	3	MM5	14	n.a.	n.a.	n.a.	n.a.	2.43
UVSFC	3	COSMO	14	n.a.	n.a.	n.a.	n.a.	1.67
UVSFC	3	MM5	24	n.a.	n.a.	n.a.	n.a.	3.93
UVSFC	3	COSMO	24	n.a.	n.a.	n.a.	n.a.	3.10
TSFC	1	MM5	14	-0.86	0.07	2.89	0.70	n.a.
TSFC	1	COSMO	14	-0.84	0.14	3.25	0.61	n.a.
TSFC	2	MM5	14	-0.40	0.07	2.58	0.74	n.a.
TSFC	2	COSMO	14	-0.81	0.14	3.23	0.62	n.a.
TSFC	3	MM5	14	1.79	0.08	3.33	0.57	n.a.
TSFC	3	COSMO	14	-0.74	0.14	3.25	0.62	n.a.
TSFC	3	MM5	24	1.58	0.05	2.91	0.74	n.a.
TSFC	3	COSMO	24	-0.40	0.12	3.58	0.59	n.a.
QSFC	1	MM5	14	-0.00027	0.00001	0.00052	0.78	n.a.
QSFC	1	COSMO	14	-0.00015	0.00003	0.00058	0.68	n.a.
QSFC	2	MM5	14	-0.00027	0.00001	0.00049	0.81	n.a.
QSFC	2	COSMO	14	-0.00011	0.00002	0.00055	0.70	n.a.
QSFC	3	MM5	14	0.00005	0.00001	0.00050	0.75	n.a.
QSFC	3	COSMO	14	-0.00007	0.00003	0.00057	0.68	n.a.
QSFC	3	MM5	24	0.00011	0.00001	0.00053	0.77	n.a.
QSFC	3	COSMO	24	0.00006	0.00002	0.00060	0.70	n.a.
G	1	MM5	14	27.9	4.1	81.4	0.52	n.a.
G	2	MM5	14	19.5	4.3	83.2	0.48	n.a.
G	3	MM5	14	-14.8	4.5	83.4	0.47	n.a.
G	3	MM5	24	-32.8	3.4	87.7	0.53	n.a.

Table 5.1.2: Mean observation MOBS, mean bias error MBE and its 95% confidence interval (Δ MBE), mean gross error MGE, correlation coefficient r and direction weighted wind error DIST of modelled vs. measured meteorological quantities measured at 14 ANETZ stations. Periods of January / February 2006 episode, domain 3. FFSFC: wind speed (m s^{-1}), DDSFC: wind direction ($^{\circ}$), UVSFC: wind vector (for dist) (m s^{-1}), TSFC: air temperature ($^{\circ}\text{C}$), QSFC: specific humidity (kg kg^{-1}), G: global irradiance (W m^{-2}). The desired accuracy: 2°C for temperature, 1 m s^{-1} for wind speeds, 30° for wind direction. See text for details.

variable	model	period	MOBS	MBE	Δ MBE	MGE	r	DIST
FFSFC	MM5	1-5 Jan 2006	1.80	0.99	0.10	1.66	0.42	n.a.
FFSFC	COSMO	1-5 Jan 2006	1.81	0.44	0.12	1.11	0.52	n.a.
FFSFC	MM5	6-16 Jan 2006	1.15	0.61	0.06	1.38	-0.11	n.a.
FFSFC	COSMO	6-16 Jan 2006	1.14	0.08	0.06	0.80	0.26	n.a.
FFSFC	MM5	17-22 Jan 2006	2.02	0.94	0.11	1.78	0.32	n.a.
FFSFC	COSMO	17-22 Jan 2006	1.99	0.72	0.13	1.33	0.63	n.a.
FFSFC	MM5	23-31 Jan 2006	1.78	1.33	0.10	1.91	0.39	n.a.
FFSFC	COSMO	23-31 Jan 2006	1.78	0.39	0.08	1.03	0.57	n.a.
FFSFC	MM5	1-4 Feb 2006	1.19	0.52	0.07	1.03	0.30	n.a.
FFSFC	COSMO	1-4 Feb 2006	1.18	0.04	0.09	0.63	0.57	n.a.
FFSFC	MM5	5-9 Feb 2006	2.04	1.22	0.13	1.82	0.38	n.a.
FFSFC	COSMO	5-9 Feb 2006	2.04	0.65	0.14	1.24	0.60	n.a.
DDSFC	MM5	1-5 Jan 2006	n.a.	61.1	n.a.	61.1	n.a.	n.a.
DDSFC	COSMO	1-5 Jan 2006	n.a.	53.8	n.a.	53.8	n.a.	n.a.
DDSFC	MM5	6-16 Jan 2006	n.a.	80.6	n.a.	80.6	n.a.	n.a.
DDSFC	COSMO	6-16 Jan 2006	n.a.	69.5	n.a.	69.5	n.a.	n.a.
DDSFC	MM5	17-22 Jan 2006	n.a.	63.9	n.a.	63.9	n.a.	n.a.
DDSFC	COSMO	17-22 Jan 2006	n.a.	58.9	n.a.	58.9	n.a.	n.a.
DDSFC	MM5	23-31 Jan 2006	n.a.	67.1	n.a.	67.1	n.a.	n.a.
DDSFC	COSMO	23-31 Jan 2006	n.a.	63.6	n.a.	63.6	n.a.	n.a.
DDSFC	MM5	1-4 Feb 2006	n.a.	72.8	n.a.	72.8	n.a.	n.a.
DDSFC	COSMO	1-4 Feb 2006	n.a.	71.0	n.a.	71.0	n.a.	n.a.
DDSFC	MM5	5-9 Feb 2006	n.a.	59.9	n.a.	59.9	n.a.	n.a.
DDSFC	COSMO	5-9 Feb 2006	n.a.	58.3	n.a.	58.3	n.a.	n.a.
UVSFC	MM5	1-5 Jan 2006	n.a.	n.a.	n.a.	n.a.	n.a.	2.38
UVSFC	COSMO	1-5 Jan 2006	n.a.	n.a.	n.a.	n.a.	n.a.	1.62
UVSFC	MM5	6-16 Jan 2006	n.a.	n.a.	n.a.	n.a.	n.a.	2.06
UVSFC	COSMO	6-16 Jan 2006	n.a.	n.a.	n.a.	n.a.	n.a.	1.36
UVSFC	MM5	17-22 Jan 2006	n.a.	n.a.	n.a.	n.a.	n.a.	2.69
UVSFC	COSMO	17-22 Jan 2006	n.a.	n.a.	n.a.	n.a.	n.a.	2.04
UVSFC	MM5	23-31 Jan 2006	n.a.	n.a.	n.a.	n.a.	n.a.	2.72
UVSFC	COSMO	23-31 Jan 2006	n.a.	n.a.	n.a.	n.a.	n.a.	1.80
UVSFC	MM5	1-4 Feb 2006	n.a.	n.a.	n.a.	n.a.	n.a.	1.66
UVSFC	COSMO	1-4 Feb 2006	n.a.	n.a.	n.a.	n.a.	n.a.	1.20
UVSFC	MM5	5-9 Feb 2006	n.a.	n.a.	n.a.	n.a.	n.a.	2.59
UVSFC	COSMO	5-9 Feb 2006	n.a.	n.a.	n.a.	n.a.	n.a.	1.93

Table 5.1.2: Continued

variable	model	period	MOBS	MBE	Δ MBE	MGE	r	DIST
TSFC	MM5	1-5 Jan 2006	-0.37	0.35	0.17	2.48	0.62	n.a.
TSFC	COSMO	1-5 Jan 2006	-0.31	-1.18	0.29	2.86	0.63	n.a.
TSFC	MM5	6-16 Jan 2006	-4.71	3.90	0.14	4.62	0.49	n.a.
TSFC	COSMO	6-16 Jan 2006	-4.69	0.28	0.28	3.85	0.48	n.a.
TSFC	MM5	17-22 Jan 2006	1.38	-0.51	0.15	2.69	0.48	n.a.
TSFC	COSMO	17-22 Jan 2006	1.37	-1.79	0.22	2.69	0.66	n.a.
TSFC	MM5	23-31 Jan 2006	-2.31	1.54	0.12	2.63	0.67	n.a.
TSFC	COSMO	23-31 Jan 2006	-2.28	-1.05	0.24	3.10	0.59	n.a.
TSFC	MM5	1-4 Feb 2006	-3.02	2.69	0.23	3.47	0.48	n.a.
TSFC	COSMO	1-4 Feb 2006	-2.99	-0.92	0.37	3.14	0.53	n.a.
TSFC	MM5	5-9 Feb 2006	-0.67	-0.59	0.16	2.51	0.57	n.a.
TSFC	COSMO	5-9 Feb 2006	-0.70	-1.57	0.24	2.52	0.65	n.a.
QSFC	MM5	1-5 Jan 2006	0.00312	-0.00005	0.00003	0.00051	0.57	n.a.
QSFC	COSMO	1-5 Jan 2006	0.00313	-0.00009	0.00006	0.00053	0.63	n.a.
QSFC	MM5	6-16 Jan 2006	0.00222	0.00020	0.00002	0.00056	0.64	n.a.
QSFC	COSMO	6-16 Jan 2006	0.00221	-0.00001	0.00004	0.00057	0.58	n.a.
QSFC	MM5	17-22 Jan 2006	0.00355	-0.00016	0.00003	0.00051	0.73	n.a.
QSFC	COSMO	17-22 Jan 2006	0.00355	-0.00022	0.00006	0.00062	0.65	n.a.
QSFC	MM5	23-31 Jan 2006	0.00266	0.00005	0.00002	0.00043	0.81	n.a.
QSFC	COSMO	23-31 Jan 2006	0.00265	-0.00003	0.00005	0.00056		n.a.
QSFC	MM5	1-4 Feb 2006	0.00266	0.00000	0.00004	0.00051	0.53	n.a.
QSFC	COSMO	1-4 Feb 2006	0.00267	-0.00019	0.00009	0.00075	0.24	n.a.
QSFC	MM5	5-9 Feb 2006	0.00286	-0.00006	0.00002	0.00034	0.75	n.a.
QSFC	COSMO	5-9 Feb 2006	0.00286	-0.00016	0.00006	0.00054	0.52	n.a.
G	MM5	1-5 Jan 2006	191.5	-29.1	13.5	98.0	0.17	n.a.
G	MM5	6-16 Jan 2006	216.1	1.7	7.0	77.8	0.47	n.a.
G	MM5	17-22 Jan 2006	223.8	-21.9	11.6	85.9	0.47	n.a.
G	MM5	23-31 Jan 2006	217.3	-24.4	7.7	82.8	0.54	n.a.
G	MM5	1-4 Feb 2006	234.5	6.3	20.7	161.3	-0.16	n.a.
G	MM5	5-9 Feb 2006	240.8	8.8	15.2	124.5	0.26	n.a.

5.2 Gaseous pollutants

The time series of measured and modelled mixing ratios of O_3 , O_x ($O_3 + NO_2$), NO_x ($NO + NO_2$) and SO_2 are shown in Figures 5.2.1 and 5.2.2 for Zurich and Payerne respectively. These plots suggest that model underestimates NO_x during the second and the fourth periods. The improvement in the agreement between modelled and measured O_x at Zurich with respect to O_3 indicates that ozone titration with NO is the main reason of disagreement for ozone plots. On the other hand, there is still a difference between modelled and measured O_x at the rural site Payerne, indicating significant dry deposition of O_3 and NO_2 . The modelled concentrations of SO_2 are higher than the measurements especially in the second and fourth periods. The model performance looks better at the elevated site Chaumont (Fig. 5.2.3). As Figure 5.1.6 suggested, the temperature inversion is probably the reason of worse model performance at Payerne than in Chaumont.

The scatter plots of modelled versus measured concentrations of some species at Zurich are shown in Figure 5.2.4 for each period. The deviations from the perfect correlation line occur mostly in the second and the fourth periods. The overestimation of ozone and SO_2 is noticeable. On the other hand, the model performance at Chaumont seems to be better for those species (Figure 5.2.5).

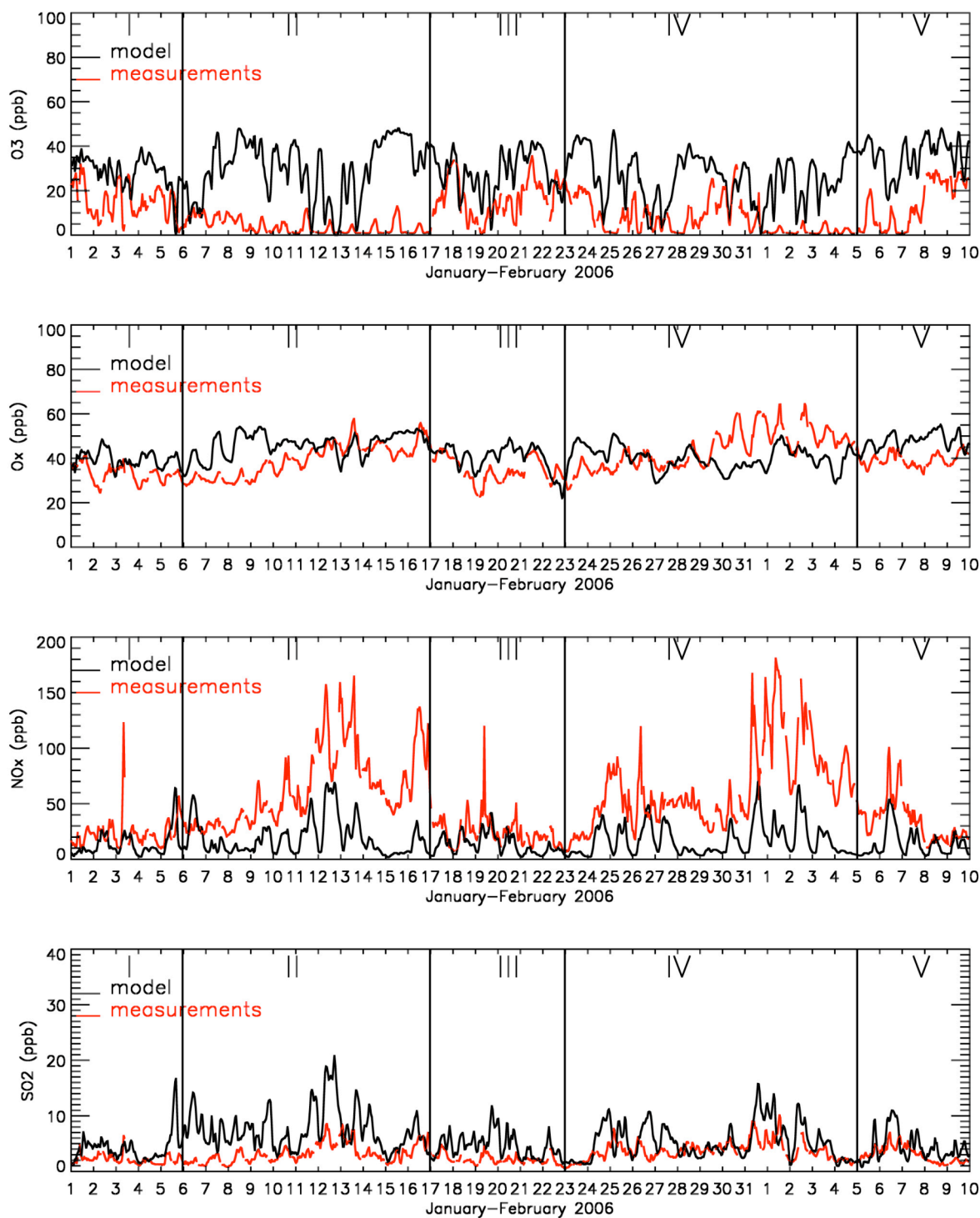


Figure 5.2.1: Comparison of modelled and measured (NABEL) gas-phase species concentrations (ppb) at Zurich in January-February 2006 ($O_x = O_3 + NO_2$).

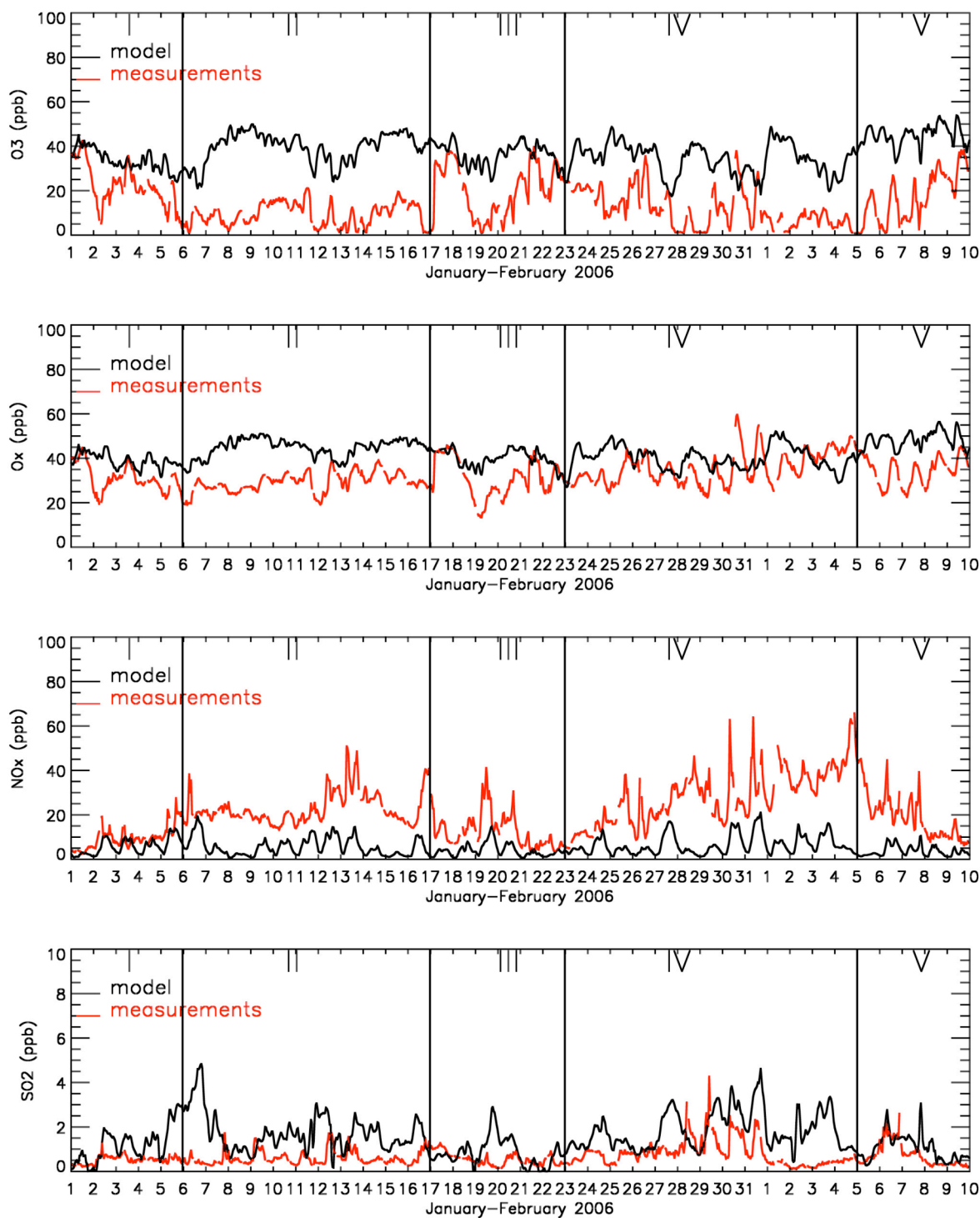


Figure 5.2.2: Comparison of modelled and measured (NABEL) gas-phase species concentrations (ppb) at Payerne in January-February 2006 ($O_x = O_3 + NO_2$).

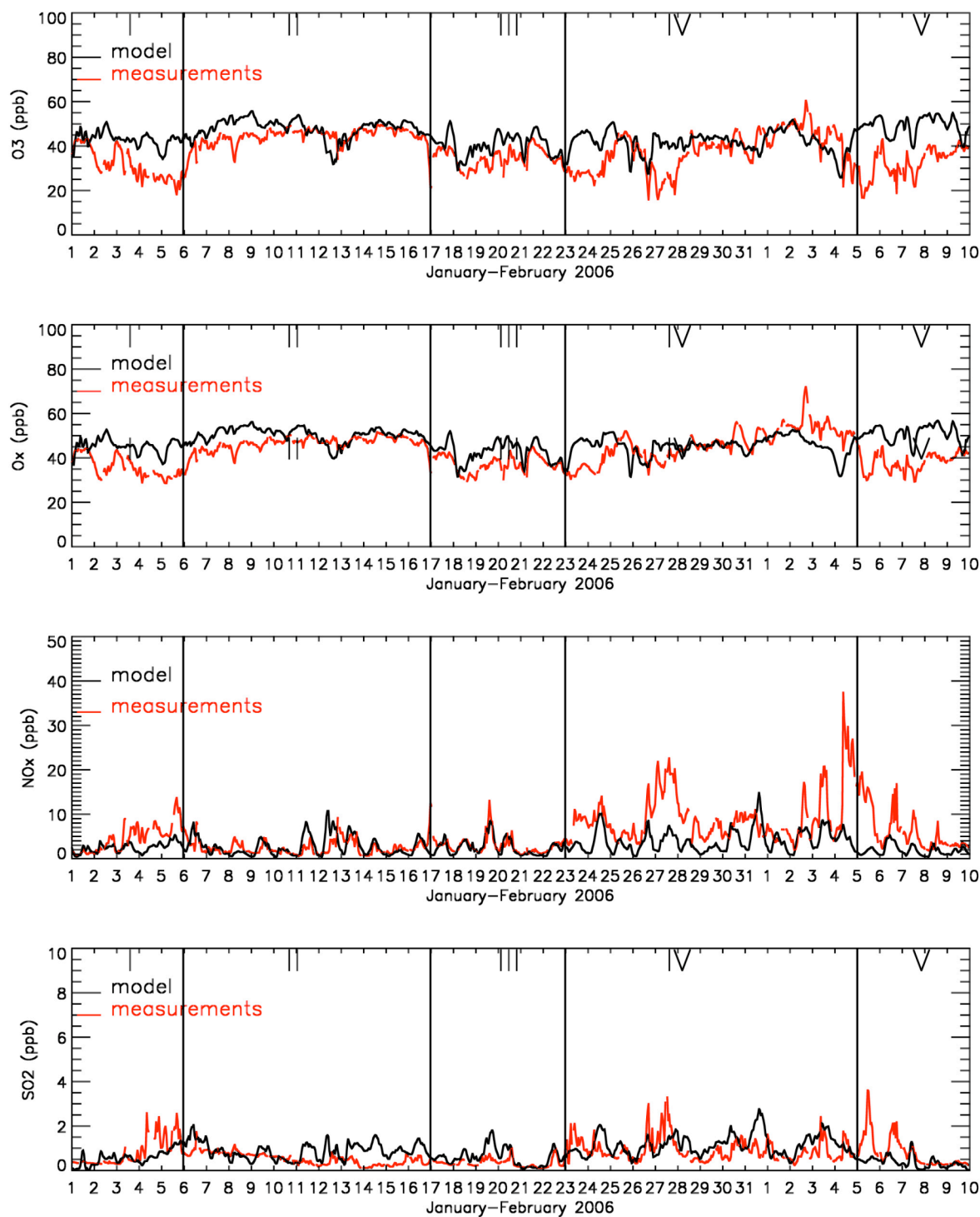


Figure 5.2.3: Comparison of modelled and measured (NABEL) gas-phase species concentrations (ppb) at Chaumont in January-February 2006 ($O_x = O_3 + NO_2$).

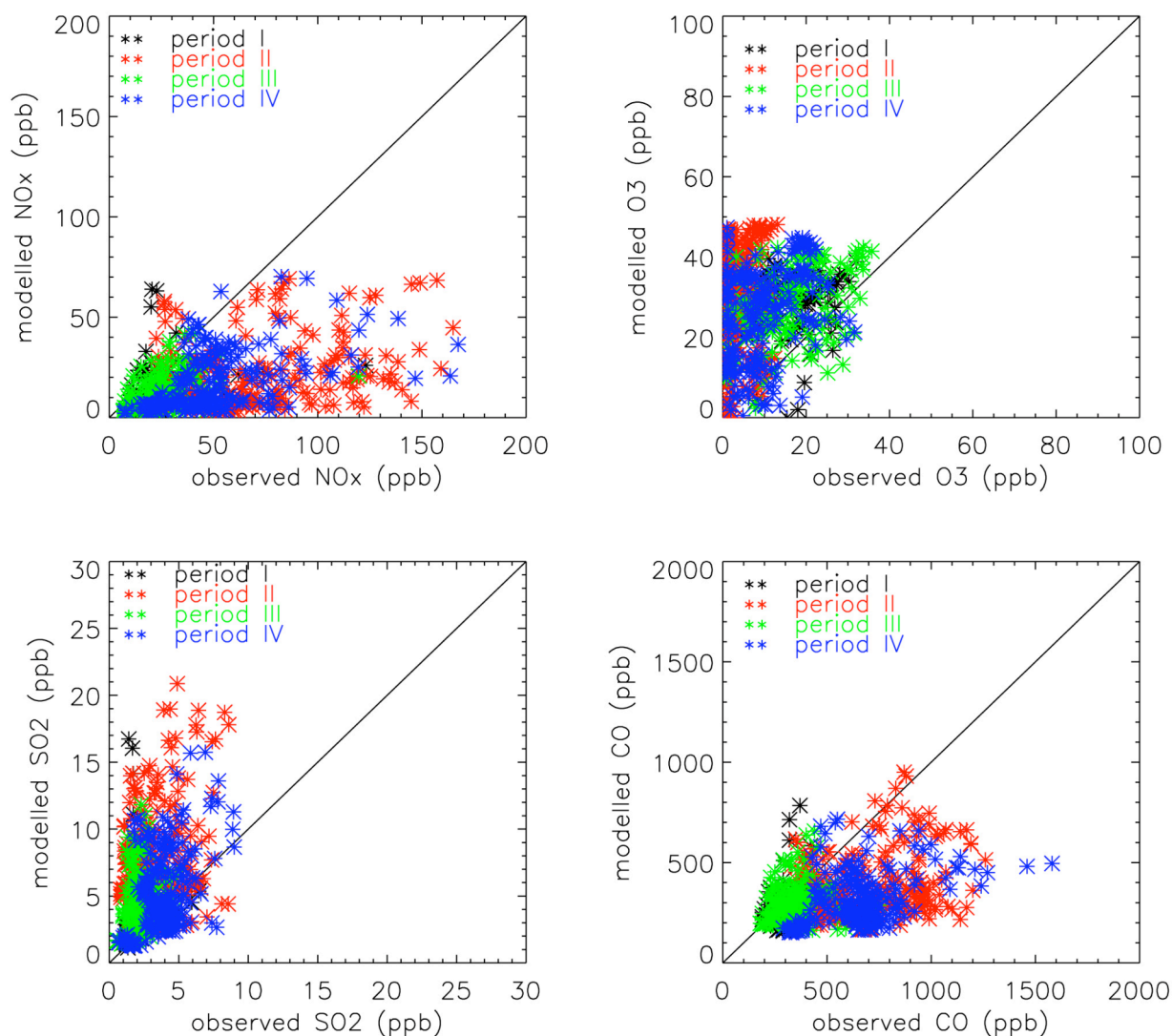


Figure 5.2.4: Comparison of modelled and observed (NABEL) gas-phase species concentrations (ppb) at Zurich in January 2006.

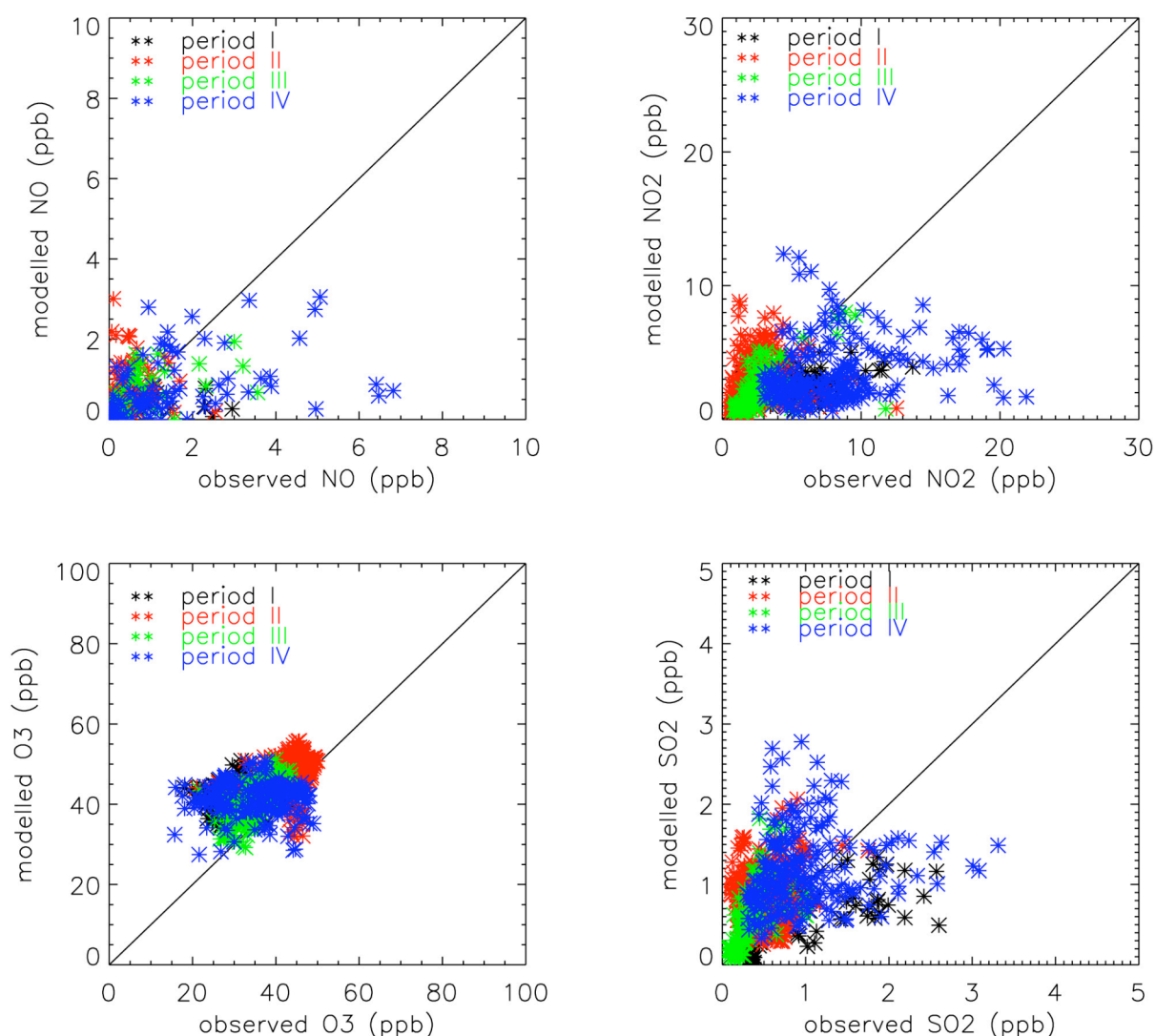


Figure 5.2.5: Comparison of modelled and measured (NABEL) gas-phase species concentrations (ppb) at Chaumont in January 2006.

5.3 Aerosols

The CAMx aerosol module calculates the distribution of primary aerosols (elemental carbon EC and primary organic aerosols POA) and formation and distribution of secondary aerosols (particulate nitrate, NO_3 , particulate sulphate, SO_4 , particulate ammonium, NH_4 , secondary organic aerosols, SOA). In this study, only the particles smaller than $2.5 \mu\text{m}$ in diameter were calculated. There are 5 SOA classes; one for SOA formed from biogenic precursors and four from different anthropogenic precursors (see section 2.2.3).

There are daily average concentrations of PM_{10} , $\text{PM}_{2.5}$ and PM_{10} measured at Payerne in 2006. These data were compared with the model $\text{PM}_{2.5}$ results for Payerne (Fig. 5.3.1). The measurements for all size fractions and the modelled $\text{PM}_{2.5}$ results are all very similar in the first and the third periods although the particle sizes are different, indicating that most of the particles were small. Measurements show an increasing trend with particle size in second and fourth periods when the wind speed was low and particle concentrations were higher. However, the predicted

PM2.5 concentrations remained low in these periods. More detailed measurements were available at Zurich (Fig. 5.3.2). These are measurements with the aerosol mass spectrometer (PM1) as well as hourly PM10 measurements at the NABEL station Zurich. These measurements have higher time resolution than filter measurements shown in Figure 5.3.1. The measured PM10 shows the same trend as AMS measurements, which refer to PM1. A collection efficiency of 0.5 was used for AMS data in this period (Lanz *et al.*, 2008). The levels of PM10 and PM1 seem to be similar in the third and the fourth periods indicating that the particles are mainly smaller than 1 micrometer. On the other hand, PM10 concentrations are higher during the second period showing the existence of coarser particles. The model predictions during the first period when the levels were low, agree quite well with PM10 measurements. All measurements and model results match very well in the third period. This figure is similar to Fig. 5.3.1 in Payerne, except the PM1 and PM10 levels are the same at Zurich in fourth period. It seems that there were more coarse particles at Payerne. The model seriously underestimates the aerosol concentrations in the second and fourth periods when particle concentrations were high.

The comparison of modelled and measured inorganic aerosol concentrations at Zurich is shown in Figure 5.3.3. The results look similar to those for gaseous species. The model predictions and AMS measurements agree quite well with each other during the third period. However, model results are lower than the measured quantities during the second and fourth period, showing mainly the effect of meteorology. The AMS measurements continued on another site at Reiden between 28 January and 9 February (Fig. 5.3.4). This site was beside the motorway A2 and exposed to road emissions. The measured concentrations of inorganic aerosols reached their peaks at the end of January and the levels of nitrate and ammonium were higher than those at Zurich. On the other hand, the model failed to capture these peaks. As in the case of gaseous species, model-measurement agreement became better during the last period after 5 February when the wind was stronger.

We also compared the measured nitrogen containing gas and aerosol compounds with the modelled ones. The gaseous ammonia and particulate ammonium ($\text{NH}_3 + \text{NH}_4$) and gaseous nitric acid and particulate nitrate ($\text{HNO}_3 + \text{NO}_3$) concentrations were measured at Payerne (Figure 5.3.5). These are daily average concentrations. The model predictions and measurements agree quite well with each other during the first and the third periods, but measurements are higher under the low-wind conditions. The comparison of modelled and measured sulphur in the particle phase shows a similar trend like nitrogen.

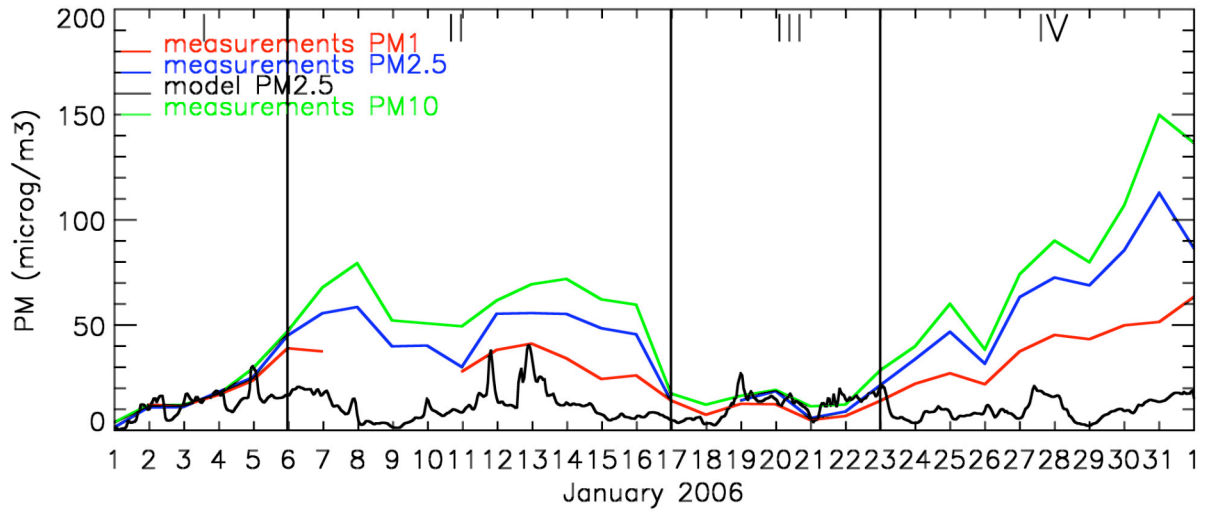


Figure 5.3.1: Comparison of PM1, PM2.5 and PM10 (daily filter measurements at Payerne NABEL station), and PM2.5 (model) ($\mu\text{g m}^{-3}$) in January 2006

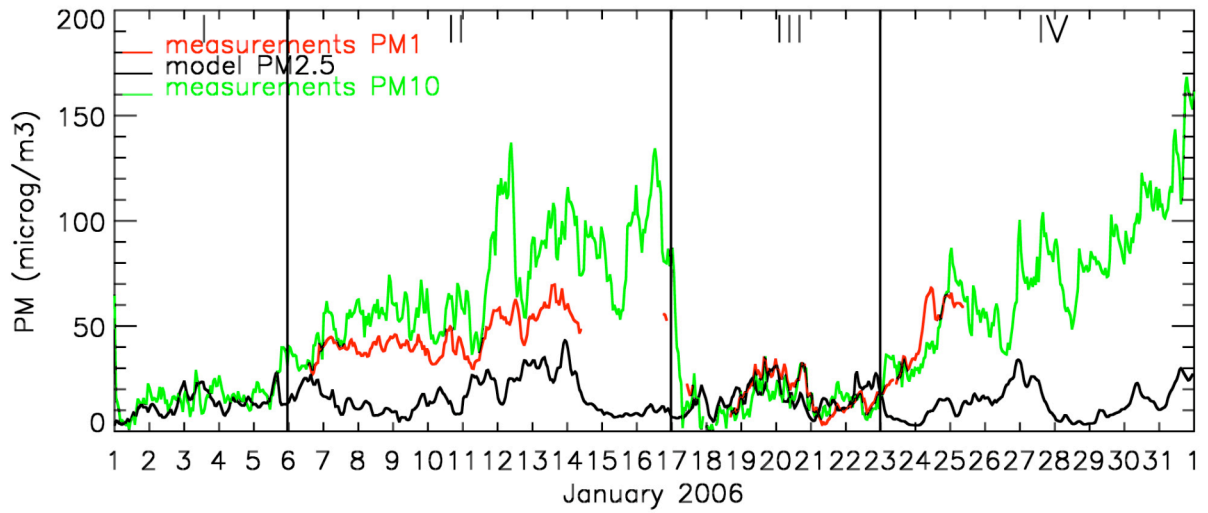


Figure 5.3.2: Comparison of PM1 (AMS measurements), PM2.5 (model) and PM10 (NABEL measurements) ($\mu\text{g m}^{-3}$) at Zurich in January 2006

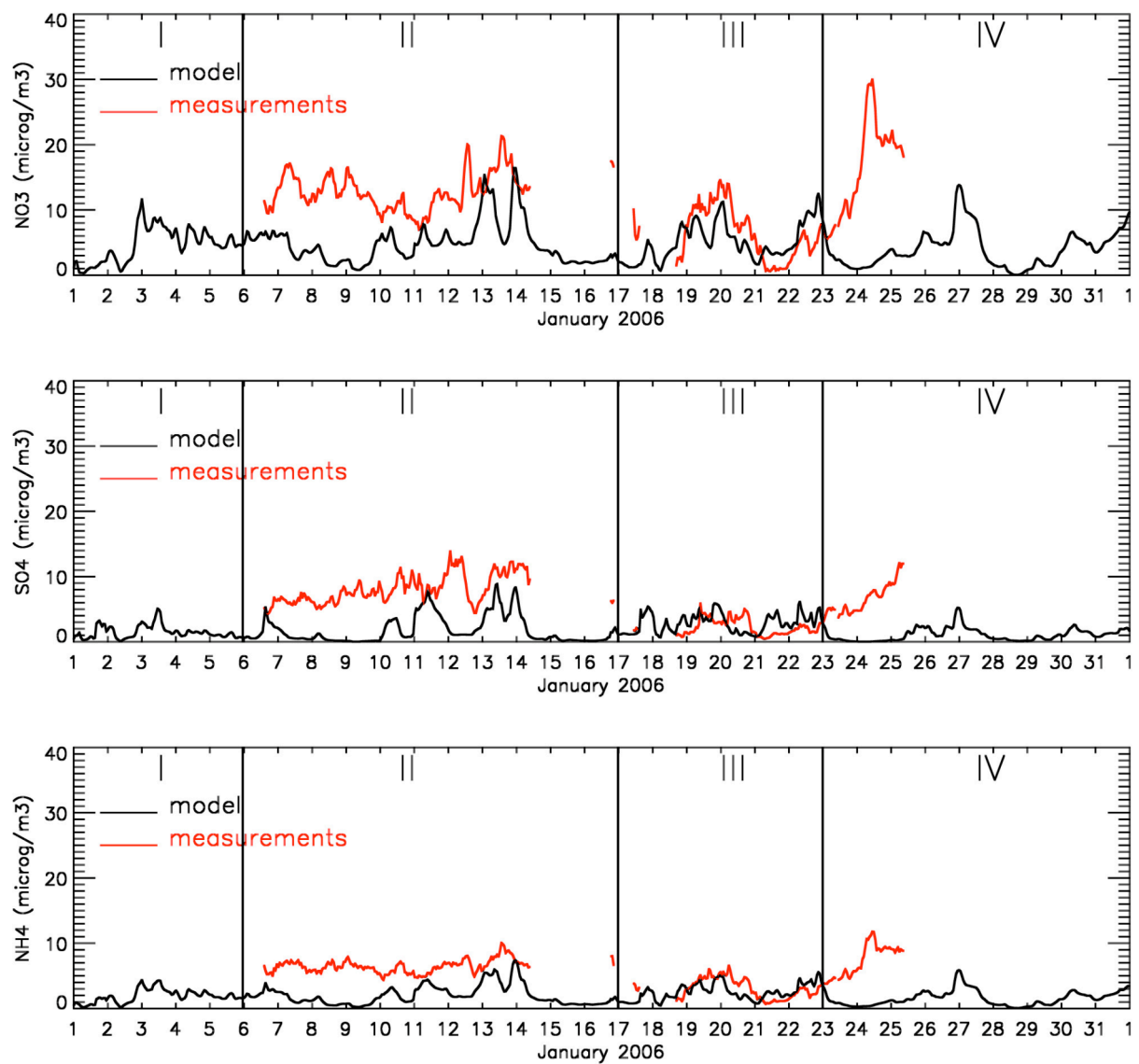


Figure 5.3.3: Comparison of modelled and measured (AMS) inorganic aerosols ($\mu\text{g m}^{-3}$) at Zurich in January 2006.

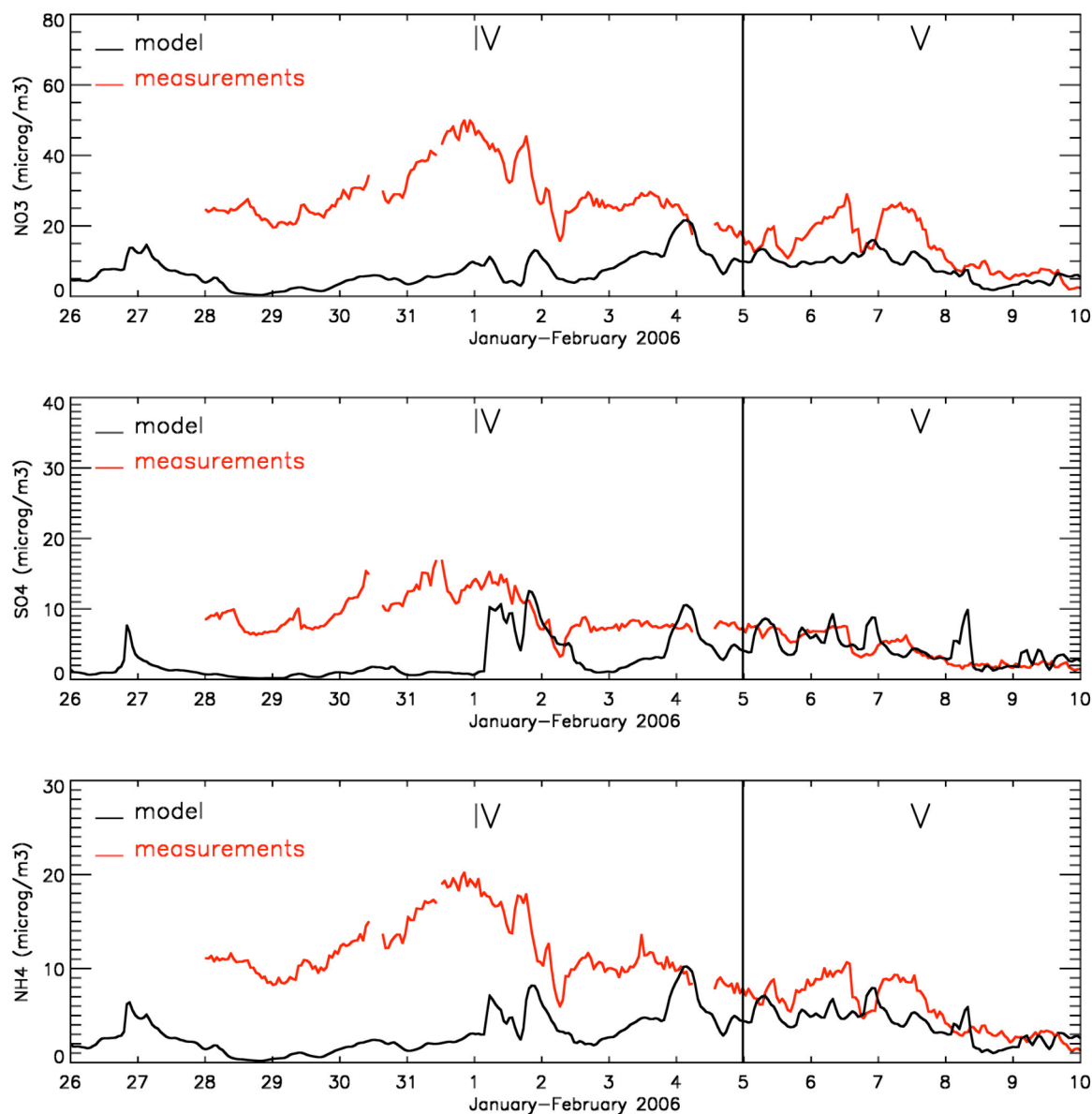


Figure 5.3.4: Comparison of modelled and measured (AMS) inorganic aerosols ($\mu\text{g m}^{-3}$) at Reiden in January-February 2006.

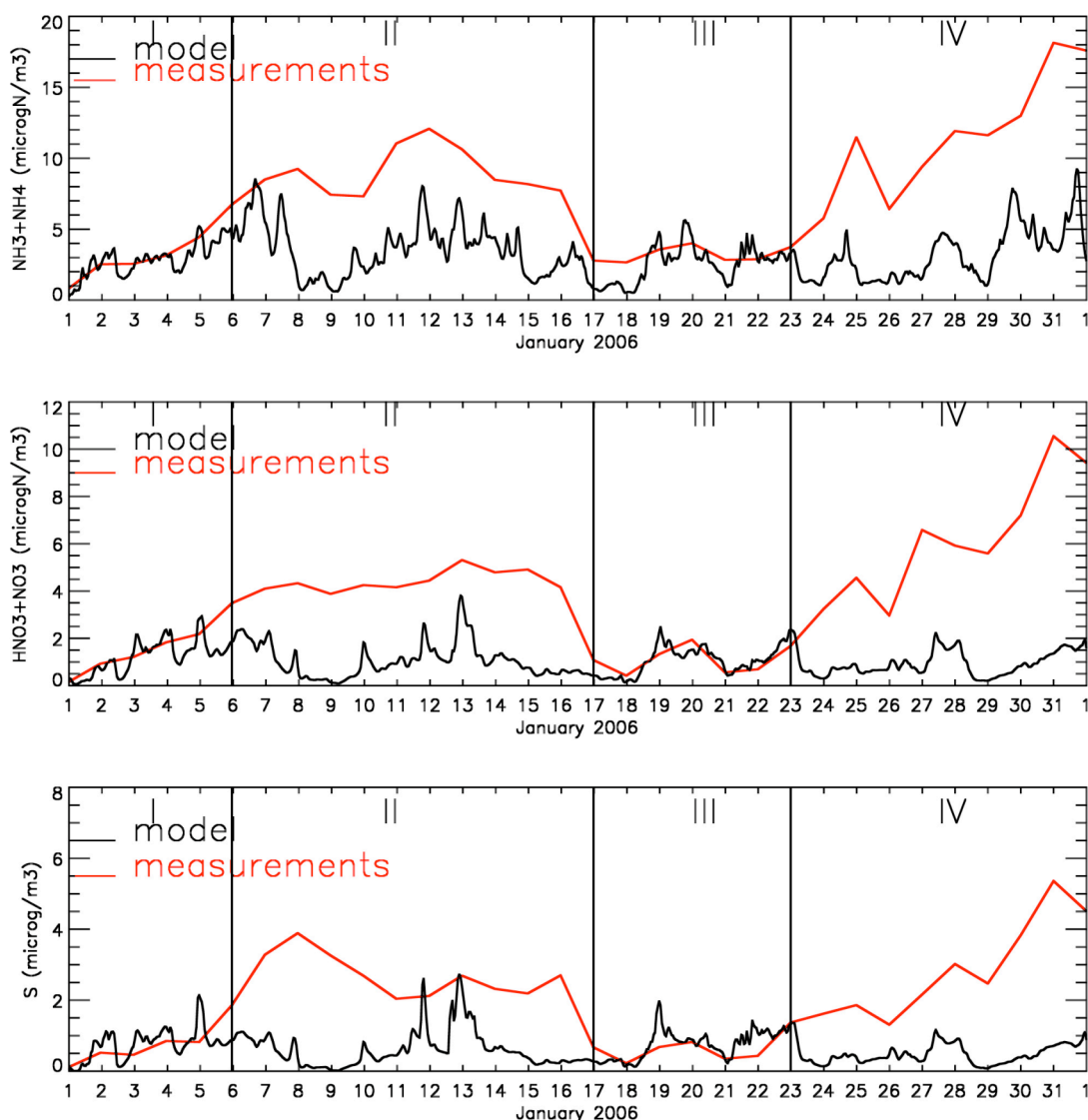


Figure 5.3.5: Comparison of modelled and measured total ammonia (upper panel), total nitrate ($\mu\text{gN m}^{-3}$) (middle panel) and S ($\mu\text{g m}^{-3}$) (lower panel) at Payerne in January 2006.

The predicted concentrations of organic aerosols are much lower than the values measured by AMS at Zurich (Fig. 5.3.6). The main fraction of organic aerosols predicted by the model is primary organic aerosols (POA) whereas the concentrations of secondary organic aerosols –mainly biogenic– are very small. The discrepancy between the measurements and model results cannot be explained only by the inaccurate representation of the meteorological parameters. There might be also other reasons causing underestimation of organic aerosols such as uncertainties in the wood-burning emissions, and/or missing mechanisms for SOA formation in the model, in addition to the insufficient performance of the meteorological model during the second and fourth period.

Analysis of AMS data suggested that about half of the particulate organic mass was oxygenated organic aerosols (OOA), mostly representing SOA (Lanz et al., 2008). However, the modelled organic aerosols are mainly primary. The SOA are substantially underestimated by the model.

The organic aerosol concentrations were very high at the end of January and beginning of February. The model underestimated organic aerosols at Reiden during the whole period whereas the difference between the measurements and the predictions was higher during the low wind period (Fig. 5.3.7).

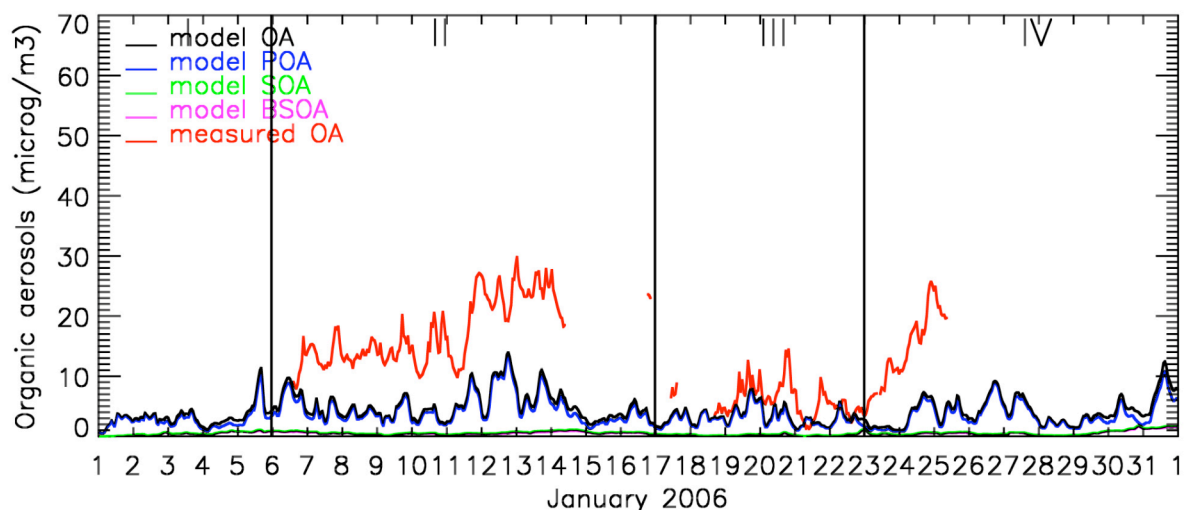


Figure 5.3.6: Comparison of modelled and measured organic aerosols ($\mu\text{g m}^{-3}$) as well as modelled POA (primary organic aerosols), SOA (secondary organic aerosols) and BSOA (biogenic secondary organic aerosols) at Zurich in January 2006.

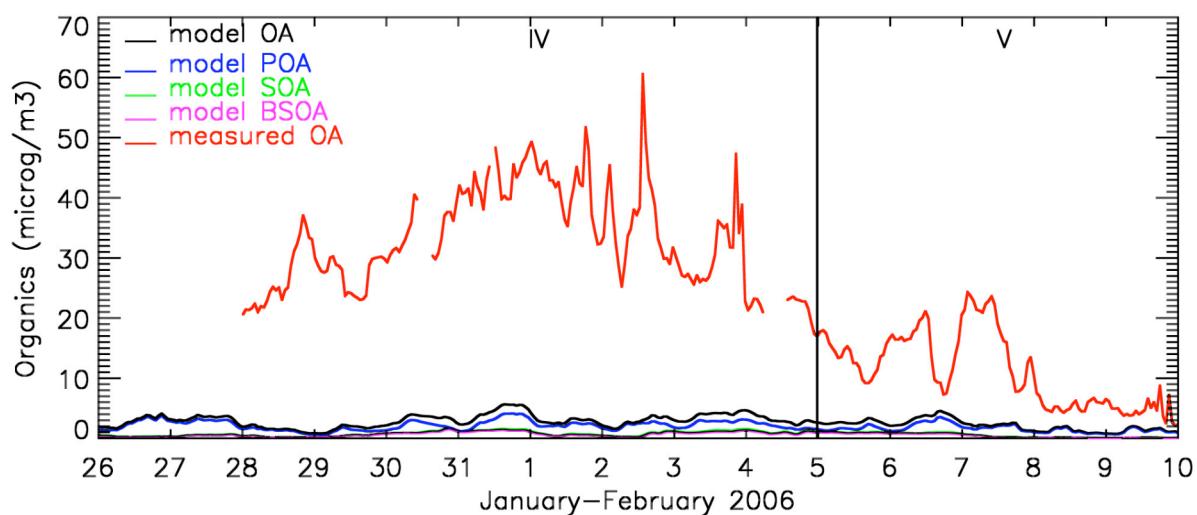


Figure 5.3.7: Comparison of modelled and measured organic aerosols ($\mu\text{g m}^{-3}$) as well as modelled POA (primary organic aerosols), SOA (secondary organic aerosols) and BSOA (biogenic secondary organic aerosols) at Reiden in January-February 2006.

Black carbon was measured by aethalometer at Zurich and Reiden, in January and February, respectively. The measurements indicate increased concentrations at the end of January and beginning of February. The modelled elemental carbon (EC) concentrations match measurements reasonably well in January at Zurich (Fig. 5.3.8). However, EC seems to be underestimated at Reiden, which is a site beside a motorway (Fig. 5.3.9).

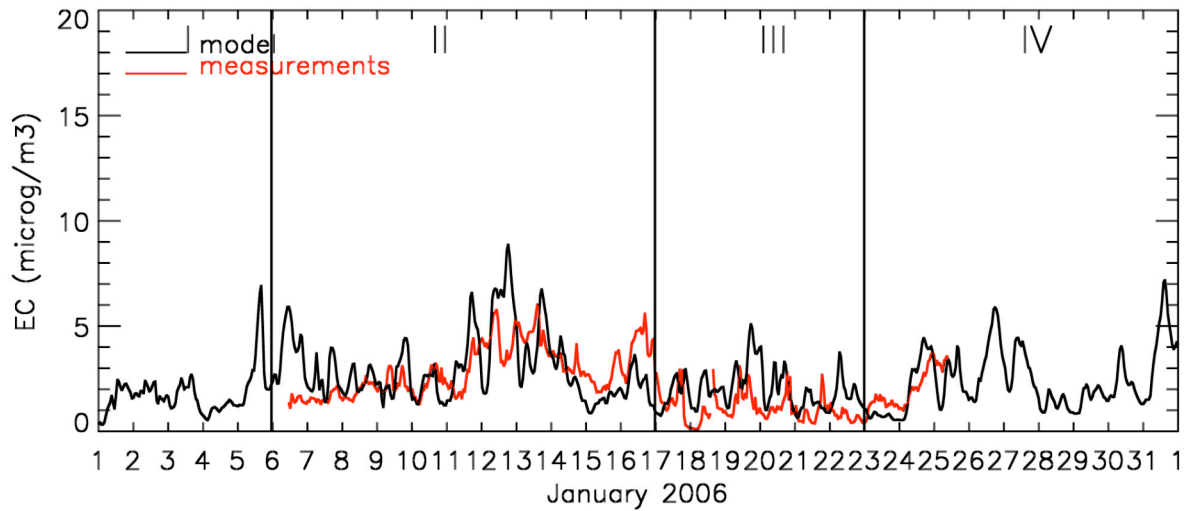


Figure 5.3.8: Comparison of modelled and measured Elemental Carbon, EC ($\mu\text{g m}^{-3}$) at Zurich in January 2006.

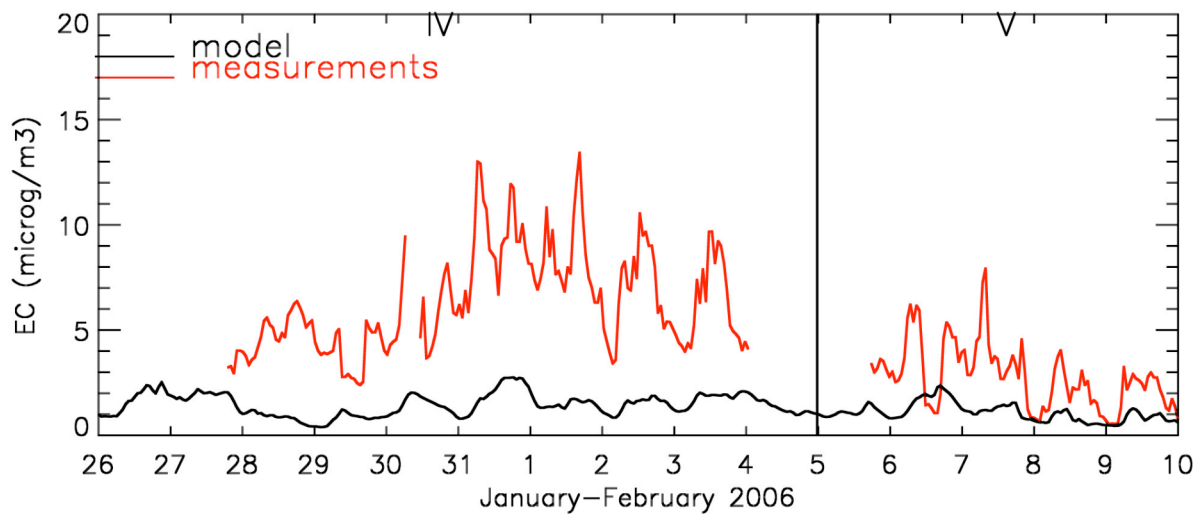


Figure 5.3.9: Comparison of modelled and measured Elemental Carbon, EC ($\mu\text{g m}^{-3}$) at Reiden in January-February.

The scatter plots of observations and predictions show the extent of error in the hourly predicted-observed pairs. The modelled versus measured concentrations of inorganic and organic aerosols at Zurich in January 2006 are shown in Figure 5.3.10. The largest deviations from the perfect correlation line are for the periods II and IV and the best correlation is in the third period.

After the investigation of the model performance at specific locations, the next step is to look at the distribution of predicted aerosol concentrations over domain 3. The

highest predicted concentrations of inorganic aerosols are shown in Figures 5.3.11 - 5.3.13. The elevated concentrations can be seen along the Swiss Plateau and around the motorways. Higher particulate nitrate concentrations are also noticeable in northern Italy, near Milan (Fig. 5.3.12). The peak values for particulate nitrate and ammonium were predicted to be at night whereas highest levels for sulphate were earlier, in the late afternoon. The highest primary aerosol concentrations were predicted around Milan, which is just below the southern border of the domain (Fig. 5.3.14). The concentrations of secondary organic aerosols on the other hand are very low and they are coming mainly from biogenic precursors (Fig. 5.3.15-5.3.17). The anthropogenic SOA is noticeable only in northern Italy. The figure showing the general distribution of total modelled aerosol concentrations over the model domain suggests that the highest levels are along the Swiss Plateau and northern Italy (Fig. 5.3.18).

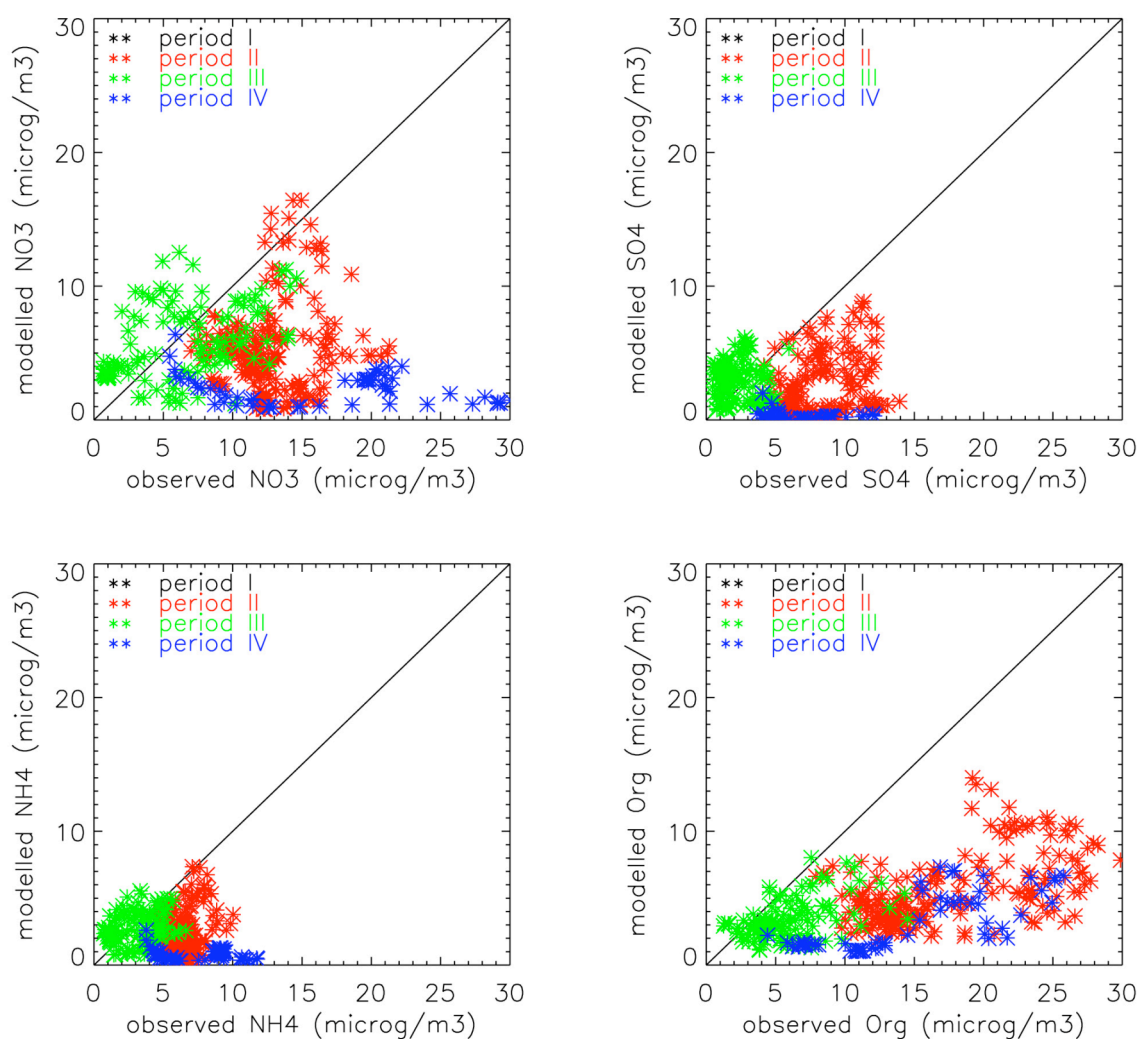


Figure 5.3.10: Modelled versus measured inorganic and organic aerosols ($\mu\text{g m}^{-3}$) at Zurich in January 2006.

A comparison of absolute as well as fractional composition of aerosols modelled and measured at Zurich is shown in Figure 5.3.19 for various periods in January 2006. Both measurements and model results suggest that the main components of the

winter aerosols in Zurich are particulate nitrate and organic aerosols. The model underestimates the organic aerosols. The agreement between measurements and model predictions for inorganic aerosols and elemental carbon (EC) is reasonably good. The predicted fraction of EC seems to be higher with respect to measurements. However, the bar charts showing the absolute values suggest that model predicts EC quite well. The underestimation of other particles (especially organic aerosols) by the model leads to apparently higher EC fraction over the total aerosol mass. In general, the best agreement between the modelled and measured concentrations of particles is for the third period.

In addition to the graphical comparison between measured and simulated concentrations at some specific locations, some statistical parameters were calculated to evaluate the model performance as described in Section 4. Table 5.1 shows the observed and predicted average concentrations, the Root Mean Square Error (RMSE), correlation coefficients, Mean Fractional Bias (MFB) and Mean Fractional Error (MFE) for particulate species. The values refer to 1-h concentration average excluding the first day of simulation. The values proposed as acceptable for PM modelling are 60% and 75% for MFB and MFE, respectively (*Boylan and Russell, 2006*). The Root Mean Square Error (RMSE) and correlation coefficients were estimated as well because they are widely used in model evaluation studies. The model performance criteria are met only during the third period (17-23 January 2006) for the inorganic and organic aerosols. However, model results for EC fulfil the requirements throughout the whole episode.

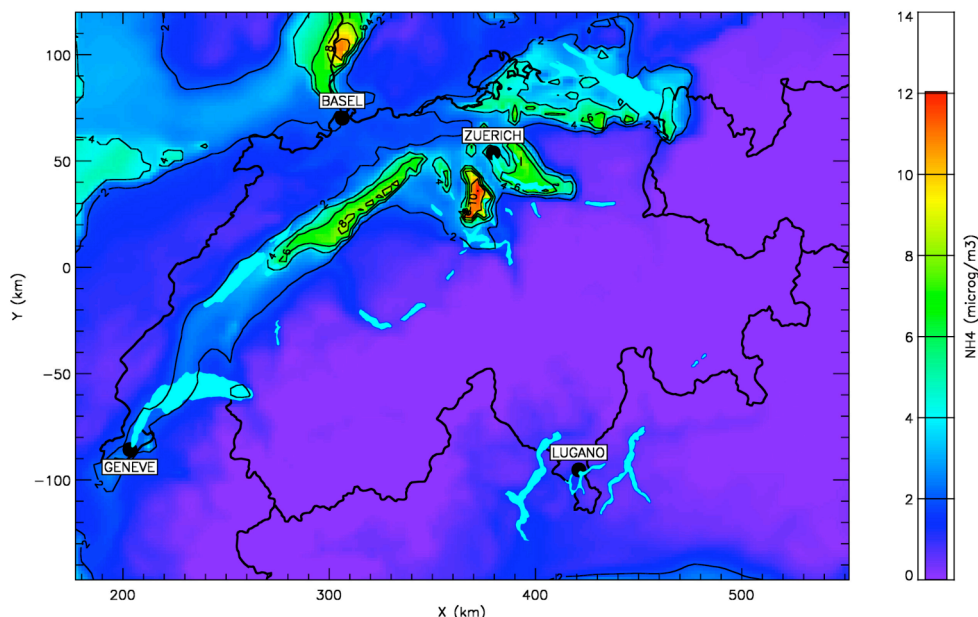


Figure 5.3.11: The highest predicted NH_4 concentrations ($\mu\text{g m}^{-3}$) on 19 January 2006, 20:00 UTC.

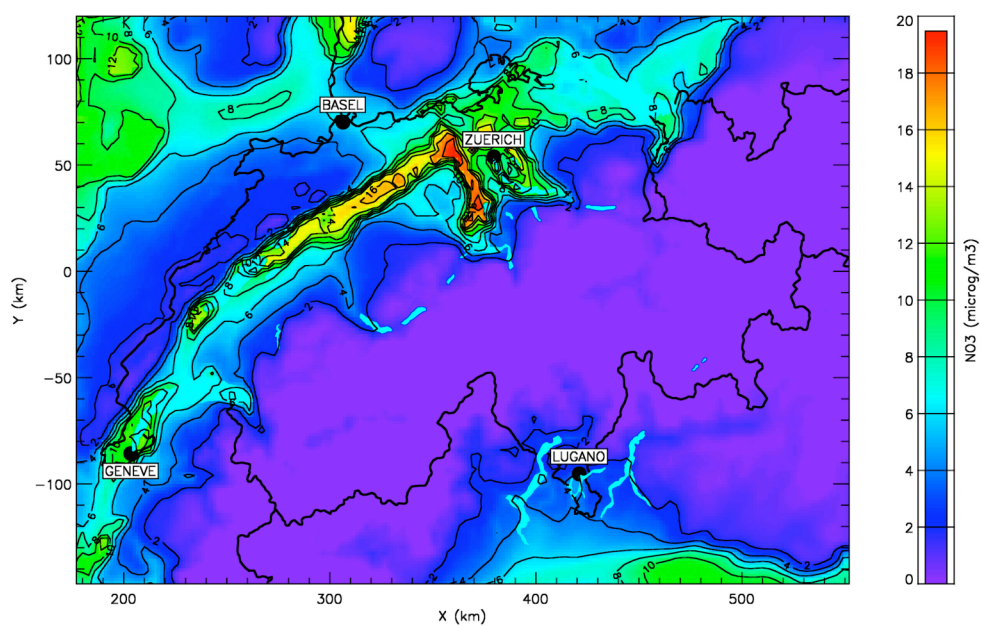


Figure 5.3.12: The highest predicted NO_3 concentrations ($\mu\text{g m}^{-3}$) on 19 January 2006, 24:00 UTC.

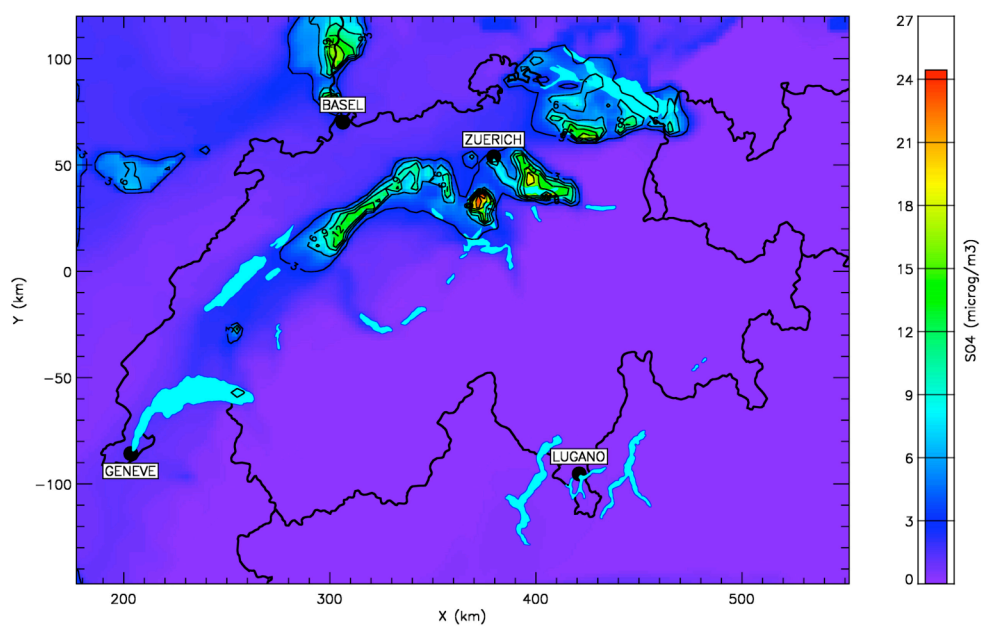


Figure 5.3.13: The highest predicted SO_4 concentrations ($\mu\text{g m}^{-3}$) on 19 January 2006, 18:00 UTC.

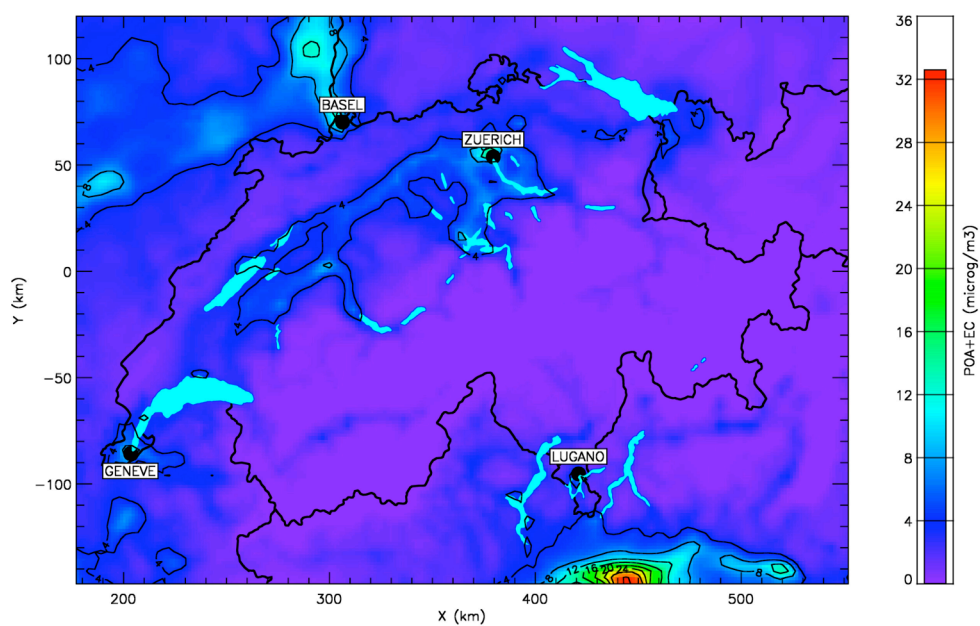


Figure 5.3.14: The highest predicted concentrations of primary aerosols (POA + EC) ($\mu\text{g m}^{-3}$) on 19 January 2006, 19:00 UTC.

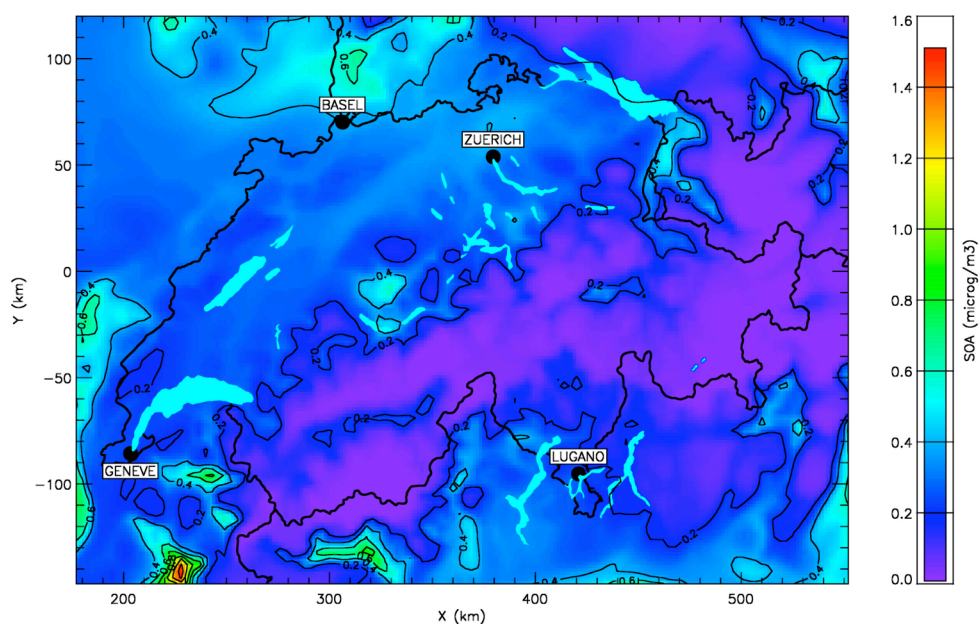


Figure 5.3.15: The highest predicted concentrations of secondary organic aerosols, SOA ($\mu\text{g m}^{-3}$) on 19 January 2006, 16:00 UTC.

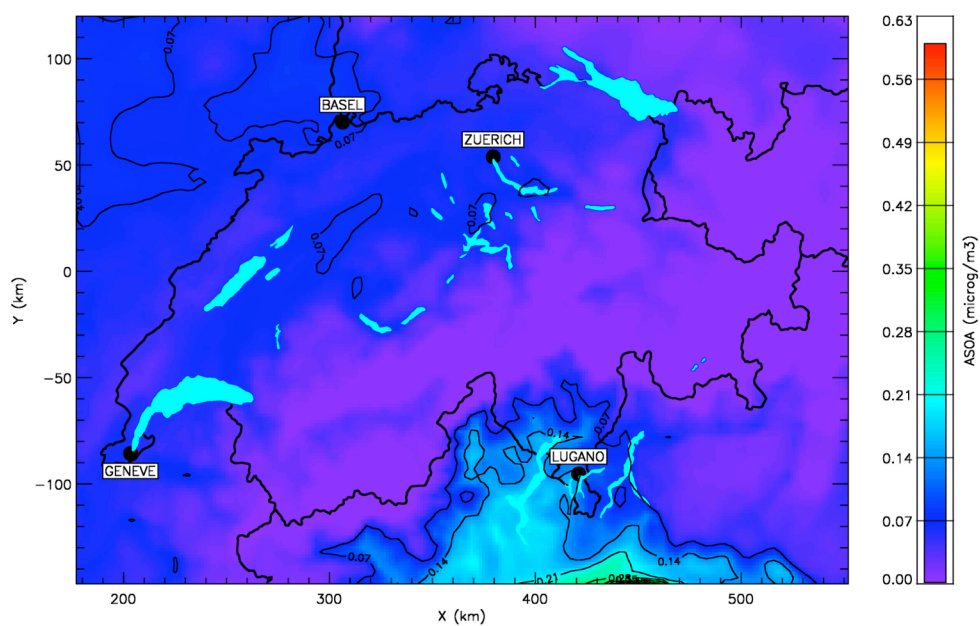


Figure 5.3.16: The highest predicted anthropogenic SOA concentrations ($\mu\text{g m}^{-3}$) on 19 January 2006, 16:00 UTC.

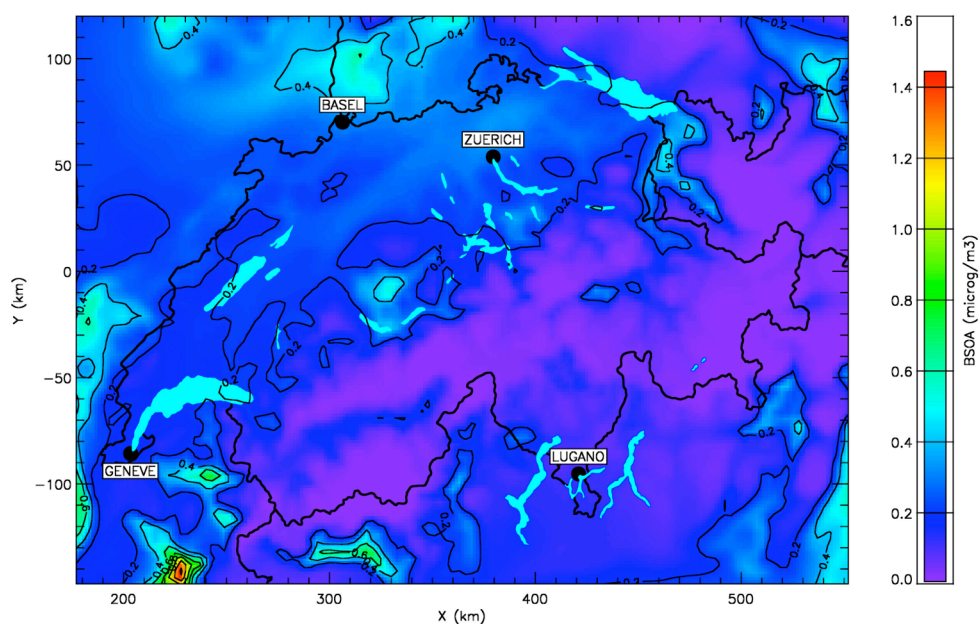


Figure 5.3.17: The highest predicted biogenic SOA concentrations ($\mu\text{g m}^{-3}$) on 19 January 2006, 16:00 UTC.

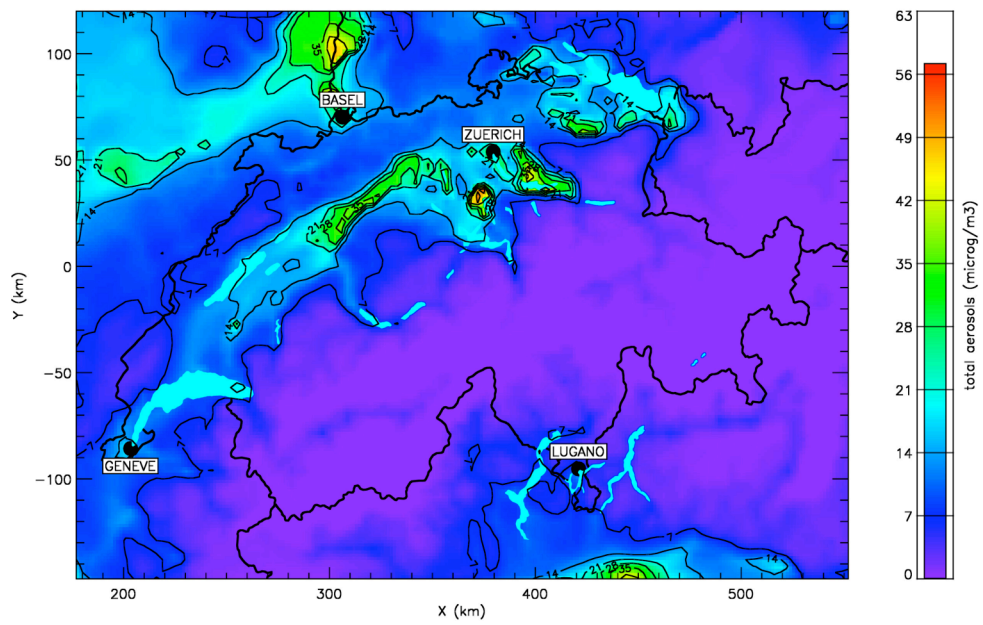


Figure 5.3.18: The highest predicted total aerosol concentrations ($\mu\text{g m}^{-3}$) on 19 January 2006, 18:00 UTC.

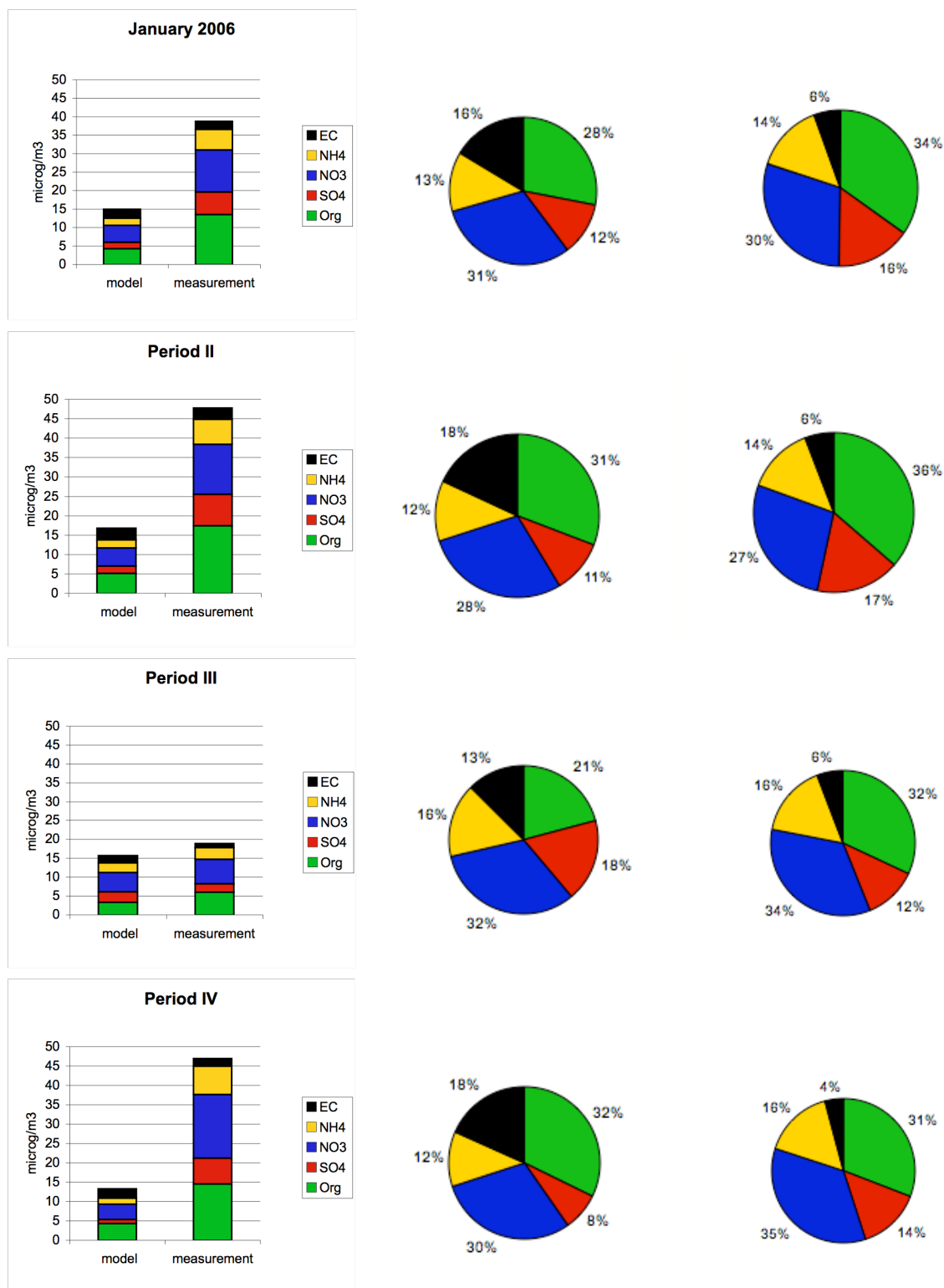


Figure 5.3.19: Comparison of absolute (left) as well as the fractional composition of modelled (middle) and measured (right) aerosols at Zurich. From top to down: whole January 2006, 6-16 January, 17-22 January, 23-31 January

Table 5.1: Statistical parameters for aerosol components for January 2006 at Zurich. The bold numbers indicate the time when the model performance criteria are met ($MFE \leq +75\%$ and $MFB \leq \pm 60\%$).

species	Time	Number of data	observed mean ($\mu\text{g m}^{-3}$)	predicted mean ($\mu\text{g m}^{-3}$)	Pred./obs.	RMSE	Correlation Coefficient r	MFB (%)	MFE (%)
NO ₃	6-16 January	191	12.88	4.75	0.37	8.63	0.099	-89	89
	17-22 January	109	6.45	5.10	0.79	3.79	0.419	4.4	65
	23-31 January	56	16.42	3.95	0.24	15.9	-0.239	-139	140
	whole January	356	11.47	4.57	0.40	9.18	-0.091	-68	90
SO ₄	6-16 January	191	8.07	1.78	0.22	6.32	0.345	-124	125
	17-22 January	109	2.25	2.86	1.27	1.97	0.028	29	66
	23-31 January	56	6.64	1.08	0.16	6.80	-0.218	-181	181
	whole January	356	6.06	1.74	0.29	5.47	-0.022	-86	116
NH ₄	6-16 January	191	6.49	2.02	0.31	4.49	0.148	-101	101
	17-22 January	109	3.07	2.51	0.82	1.65	0.287	-4.8	52
	23-31 January	56	7.37	1.54	0.21	7.05	-0.249	-156	156
	whole January	356	5.58	1.96	0.35	4.41	-0.159	-80	95
Organics	6-16 January	191	17.39	5.14	0.30	12.8	0.495	-105	105
	17-22 January	109	6.01	3.25	0.54	3.57	0.451	-52	59
	23-31 January	56	14.50	4.27	0.30	12.3	0.720	-131	131
	whole January	356	13.45	4.20	0.31	10.8	0.583	-93	95
EC	6-16 January	253	2.85	3.01	1.06	1.58	0.395	0.20	41
	17-22 January	143	1.10	1.98	1.80	1.67	0.137	57	71
	23-31 January	58	1.94	2.42	1.25	0.933	0.725	-27	50
	whole January	454	2.17	2.44	1.12	1.54	0.462	15	52

6 Episode 2: June 2006

6.1 Meteorology

Based on the time series of measured and predicted wind direction, wind speed, air temperature, precipitation and CO mixing ratio at the NABEL station Payerne (Figure 6.1.1) June 2006 was divided into 3 periods:

Period I: 1-11 June

Period II: 12-16 June

Period III: 17-30 June

The first half of the month was a dry period with increasing temperature and moderate to strong winds. The temperature increase was a result of the Azores High moving towards the Iberian Peninsula causing ridging across Western Europe. Measurements and model results of CO from 1 to 11 June (period I) match reasonably well (see bottom panel in Figure 6.1.1). From 12 to 16 June the measured wind speed was lower than in the previous period. There was no cloud cover and the measured temperatures at night were lower than the predicted ones. This implies that radiative cooling during night is underestimated in the model. Strong radiative cooling at night leads to strong stratification, which in turn is associated with high pollution levels. Inadequate representation of this phenomenon in the model leads to underestimation of pollution levels after 12 June. During period I the surface inversion during night was not so strong. In period II however, there was a surface inversion with a strong gradient that was not properly reproduced by the model. Note that in low-wind conditions, pollution levels during the day build up nighttime pollution. Therefore, errors in air pollution estimates at night continue affecting the results during the next day. The reason for the underestimation of the surface inversion strength in MM5 is probably because in the first half of the month, clear skies and high temperatures led to evaporation of soil moisture which was not captured by the land surface model of MM5. This in turn leads to incorrect partitioning between sensible and latent heat flux and underestimation of radiative cooling during night. After 17 June (period III) model performance varied as a result of varying meteorological conditions.

In general, weather conditions and CO levels were much more uniform than in January 2006 and different periods less distinct. High concentrations of CO were only observed in isolated peaks (e.g. 14 and 29 June). Examination of the origin of those peaks by using backward trajectories did not show any influence from distant sources. Therefore those peaks probably reflect the presence of plumes from local sources, which are very difficult to capture in meso-scale modelling.

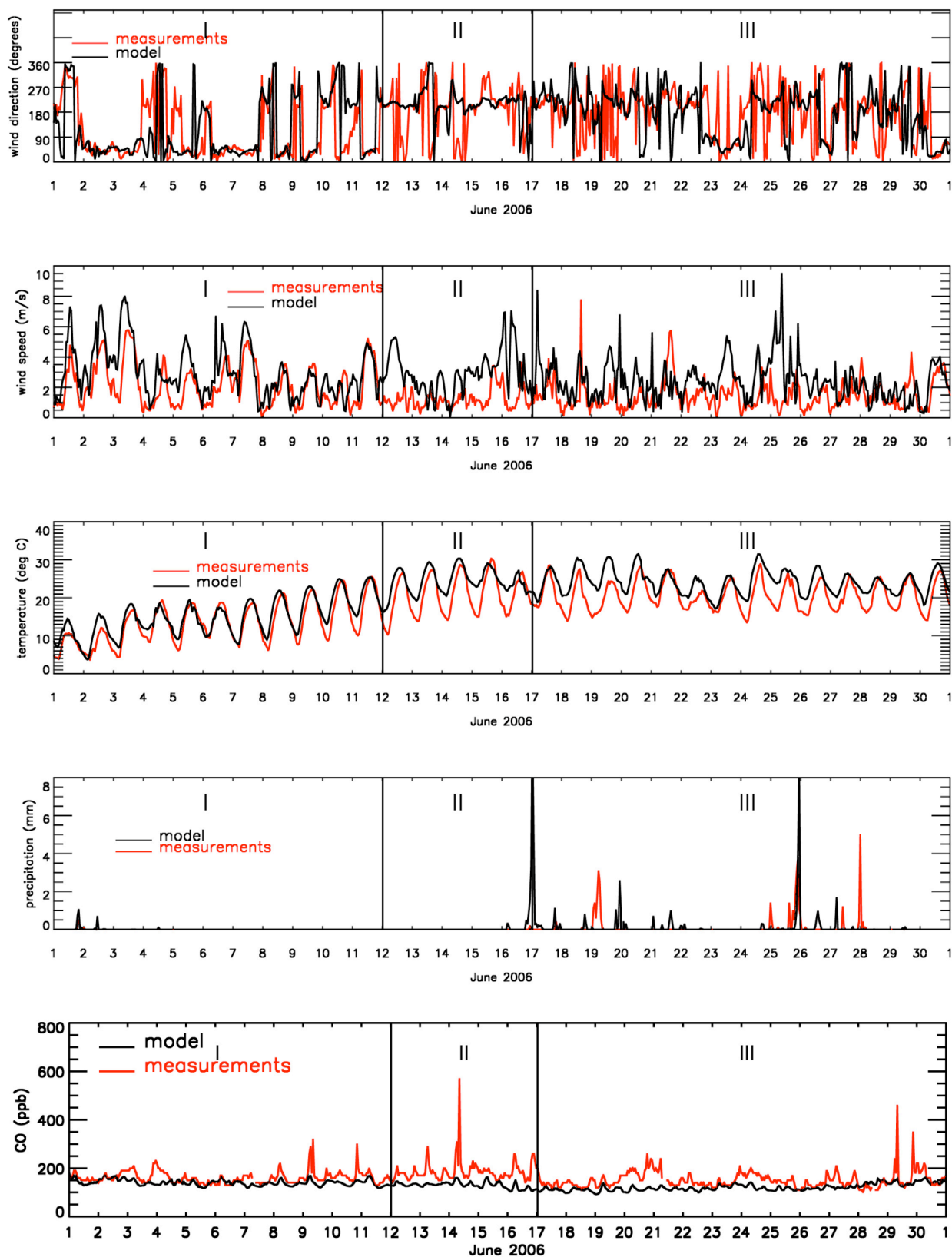


Figure 6.1.1: The comparison of measured and modelled wind speed (m s^{-1}), precipitation (mm) and temperature (C) at Payerne (NABEL station) in June 2006 as well as the CO concentrations (ppb).

Figures A8 to A14 in the Appendix show the time series of surface wind speed, wind direction, air temperature, specific humidity, global irradiance, planetary boundary layer height, and precipitation rate at CHA, PAY, KLO, STG, SIO and MAG for domain 3. Again, wind speed at the mountain station CHA is strongly under-predicted by both models. The same is true for the valley station SIO where the peaks at noon are not captured. MM5 temperature variations follow the observations very well, whereas COSMO 7 fails to predict minimum or maximum temperatures correctly. Modelled and measured specific humidity agrees fairly well during the first 10 days. MM5 simulations, however, peak in early afternoon. For clear days the shortwave downward irradiance of MM5 is similar to the observed global irradiance. PBL height varies qualitatively in accordance with solar radiation. However, it is surprising that the values at SIO and MAG are much smaller than expected from the irradiance time series. CBL heights based on soundings at Payerne are greater than MM5 simulations on nearly every day. This is particularly true from 5 to 22 June. Unlike in January 2006, the agreement between the modelled and observed rain rates is moderate.

The correlation coefficient of wind speed is largest in period I when the mean speed was relatively high, and close to zero for the low wind period II (Table 6.1.1). MBE is below 1 m s^{-1} for every period. Regarding wind direction, MBE of wind direction is comparable with the values in January, the numbers of the first period being about 10° smaller than those of period II and III. The variability of DiST is about the same as in winter 2006. Temperature has a high correlation (between 0.76 and 0.91) and its MBE is below 3°C . It is worth mentioning that MM5 performance is better (smaller MBE and MGE) than COSMO 7 although the data of the latter is reanalyzed. The performance of specific humidity in terms of MBE, MGE and correlation coefficient is best in period I. For June as a whole, the agreement between model and observations is slightly worse than for the winter 2006 episode. Global irradiance correlates quite well ($0.61 < r < 0.85$) mainly due to the large number of clear days.

6.2 Gaseous pollutants

The time series of some of the gaseous species are plotted in Figures 6.2.1 and 6.2.2 at Zurich and Payerne, respectively. At both sites, the peak ozone is underestimated during the low wind period between 12 and 17 June. The improved agreement at night in O_x plots with respect to O_3 plots indicates the effect of ozone titration at the urban site Zurich (Fig. 6.2.1). On the other hand, O_x results do not show much improvement in the night at the rural site Payerne where NO_x concentrations are relatively lower. The less pronounced diurnal pattern by the model is noticeable at Payerne.

The predicted peak ozone concentrations on 15 June 2006, at 15:00 UTC are shown in Figure 6.2.3. The highest levels are in the southern part of Switzerland. The elevated ozone concentrations can also be seen along the Swiss Plateau.

The scattered plots of predicted and observed concentrations of NO_x , O_3 , SO_2 and CO are shown for each period at Zurich and Payerne (Figures 6.2.4, 6.2.5, respectively). The best correlation seems to be in the first period for the gaseous species. These plots indicate overestimation of ozone at low concentrations and underestimation at high concentrations.

The statistical parameters for ozone were calculated using the model performance measures described in Section 4. Table 6.2.1 shows these parameters for ozone at various NABEL stations. The numbers refer to daytime values throughout June 2006. The model performance criteria are met at some rural sites such as Chaumont, Laegern,

Payerne, and Taenikon as well as urban and suburban sites like Lugano and Duebendorf, respectively. Some elevated sites such as Davos and Rigi are also among the locations where the model performance is acceptable. The worst performance was obtained at Basel (suburban), Bern (urban) and Haerkingen (motorway).

Table 6.1.1: Mean observation MOBS, mean bias error MBE and its 95% confidence interval (Δ MBE), mean gross error MGE, correlation coefficient r and direction weighted wind error DIST of modelled vs. measured meteorological quantities measured at 14 ANETZ stations. Periods of June 2006 episode, domain 3. FFSFC: wind speed ($m s^{-1}$), DDSFC: wind direction ($^{\circ}$), UVSFC: wind vector (for dist) ($m s^{-1}$), TSFC: air temperature ($^{\circ}C$), QSFC: specific humidity ($kg kg^{-1}$), G: global irradiance ($W m^{-2}$). The desired accuracy: $2^{\circ}C$ for temperature, $1 m s^{-1}$ for wind speeds, 30° for wind direction. See text for details.

variable	model	period	MOBS	MBE	Δ MBE	MGE	r	DIST
FFSFC	MM5	1-11 Jun 2006	2.30	0.26	0.06	1.36	0.45	n.a.
FFSFC	COSMO	1-11 Jun 2006	2.29	0.11	0.10	1.25	0.44	n.a.
FFSFC	MM5	12-16 Jun 2006	1.65	0.39	0.09	1.44	-0.03	n.a.
FFSFC	COSMO	12-16 Jun 2006	1.62	-0.17	0.14	1.05	0.00	n.a.
FFSFC	MM5	17-30 Jun 2006	1.85	0.49	0.05	1.31	0.32	n.a.
FFSFC	COSMO	17-30 Jun 2006	1.85	-0.15	0.08	1.09	0.23	n.a.
DDSFC	MM5	1-11 Jun 2006	n.a.	58.3	n.a.	58.3	n.a.	n.a.
DDSFC	COSMO	1-11 Jun 2006	n.a.	55.8	n.a.	55.8	n.a.	n.a.
DDSFC	MM5	12-16 Jun 2006	n.a.	65.8	n.a.	65.8	n.a.	n.a.
DDSFC	COSMO	12-16 Jun 2006	n.a.	65.5	n.a.	65.5	n.a.	n.a.
DDSFC	MM5	17-30 Jun 2006	n.a.	68.7	n.a.	68.7	n.a.	n.a.
DDSFC	COSMO	17-30 Jun 2006	n.a.	63.6	n.a.	63.6	n.a.	n.a.
UVSFC	MM5	1-11 Jun 2006	n.a.	n.a.	n.a.	n.a.	n.a.	2.25
UVSFC	COSMO	1-11 Jun 2006	n.a.	n.a.	n.a.	n.a.	n.a.	2.08
UVSFC	MM5	12-16 Jun 2006	n.a.	n.a.	n.a.	n.a.	n.a.	2.23
UVSFC	COSMO	12-16 Jun 2006	n.a.	n.a.	n.a.	n.a.	n.a.	1.78
UVSFC	MM5	17-30 Jun 2006	n.a.	n.a.	n.a.	n.a.	n.a.	2.33
UVSFC	COSMO	17-30 Jun 2006	n.a.	n.a.	n.a.	n.a.	n.a.	1.89
TSFC	MM5	1-11 Jun 2006	13.81	-0.41	0.08	1.85	0.91	n.a.
TSFC	COSMO	1-11 Jun 2006	13.72	-2.64	0.23	3.31	0.81	n.a.
TSFC	MM5	12-16 Jun 2006	20.89	0.05	0.60	2.44	0.80	n.a.
TSFC	COSMO	12-16 Jun 2006	20.91	-2.68	0.43	3.69	0.78	n.a.
TSFC	MM5	17-30 Jun 2006	20.89	0.46	0.09	2.40	0.76	n.a.
TSFC	COSMO	17-30 Jun 2006	20.91	-1.60	0.21	2.92	0.77	n.a.
QSFC	MM5	1-11 Jun 2006	0.00565	0.00025	0.00005	0.00108	0.66	n.a.
QSFC	COSMO	1-11 Jun 2006	0.00564	-0.00030	0.00008	0.00096	0.59	n.a.
QSFC	MM5	12-16 Jun 2006	0.00884	0.00011	0.00010	0.00160	0.43	n.a.
QSFC	COSMO	12-16 Jun 2006	0.00882	-0.00077	0.00019	0.00187	0.47	n.a.
QSFC	MM5	17-30 Jun 2006	0.01092	-0.00055	0.00006	0.00160	0.41	n.a.
QSFC	COSMO	17-30 Jun 2006	0.01093	-0.00041	0.00011	0.00178	0.58	n.a.
G	MM5	1-11 Jun 2006	504.6	37.7	8.3	137.8	0.78	n.a.
G	MM5	12-16 Jun 2006	519.6	22.9	9.7	111.3	0.85	n.a.
G	MM5	17-30 Jun 2006	471.8	49.4	9.6	182.8	0.61	n.a.

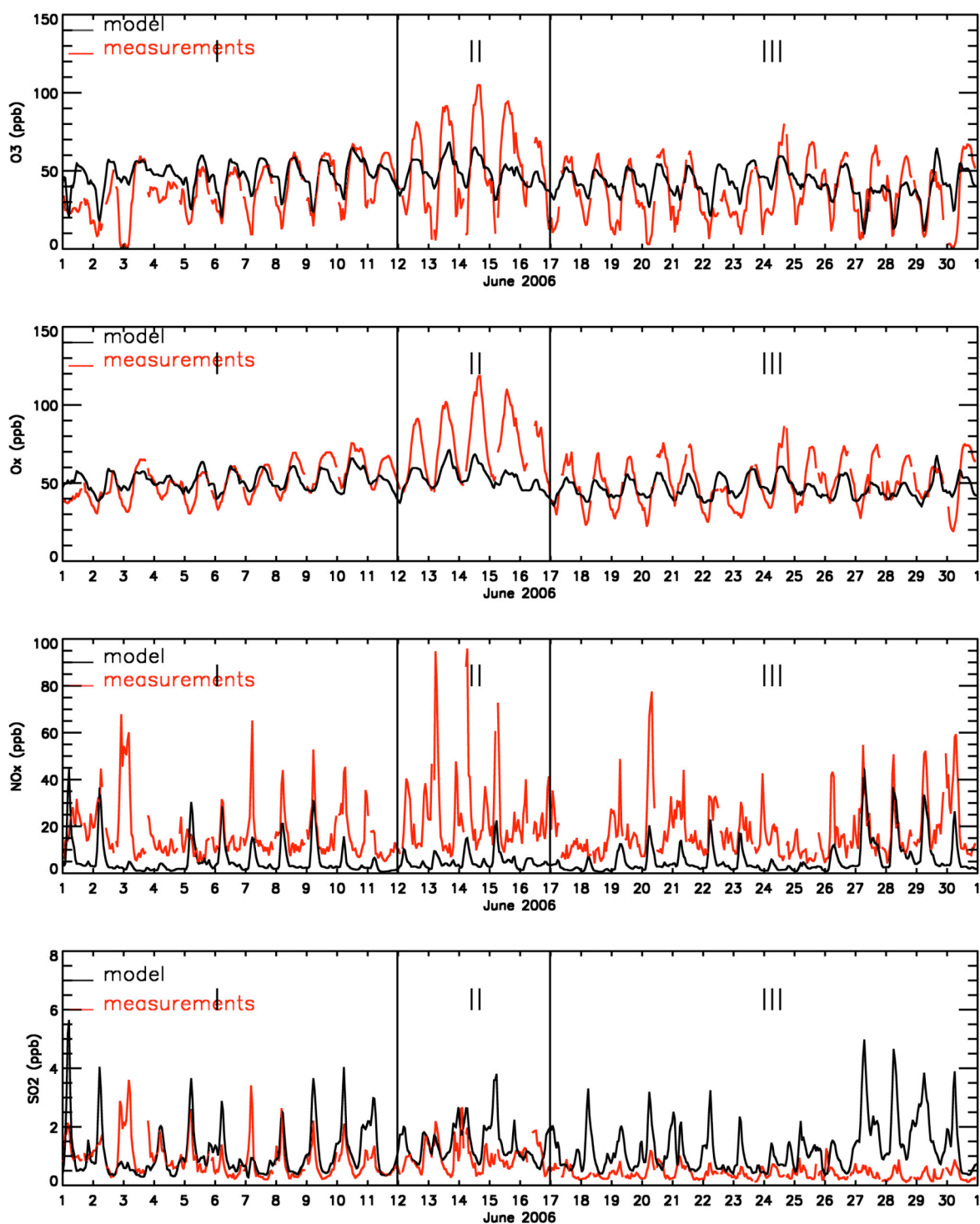


Figure 6.2.1: Comparison of modelled and measured (NABEL) gas-phase species concentrations (ppb) at Zurich in June 2006 ($O_x = O_3 + NO_2$).

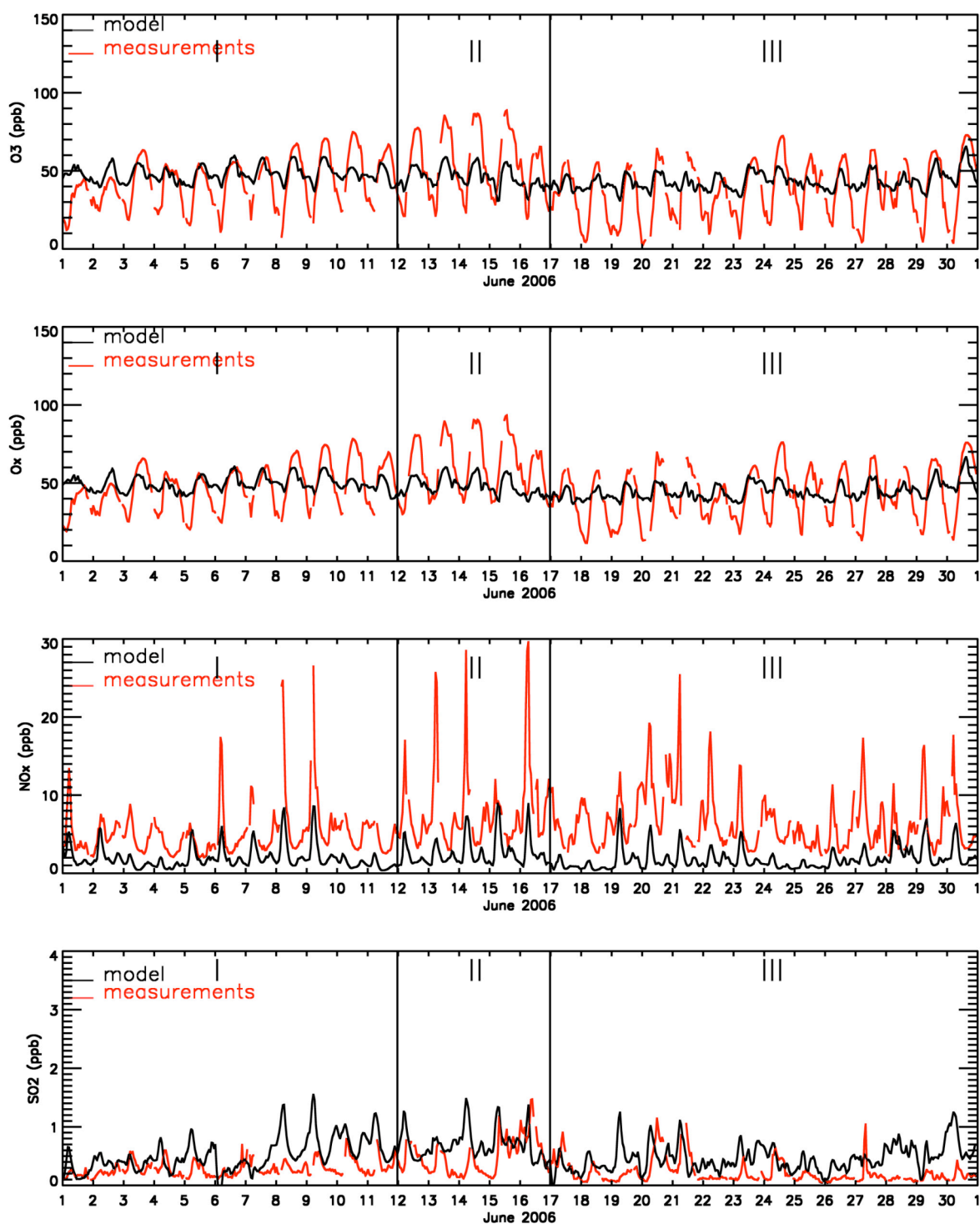


Figure 6.2.2. Comparison of modelled and measured (NABEL) gas-phase species concentrations (ppb) at Payerne in June 2006 ($O_x = O_3 + NO_2$).

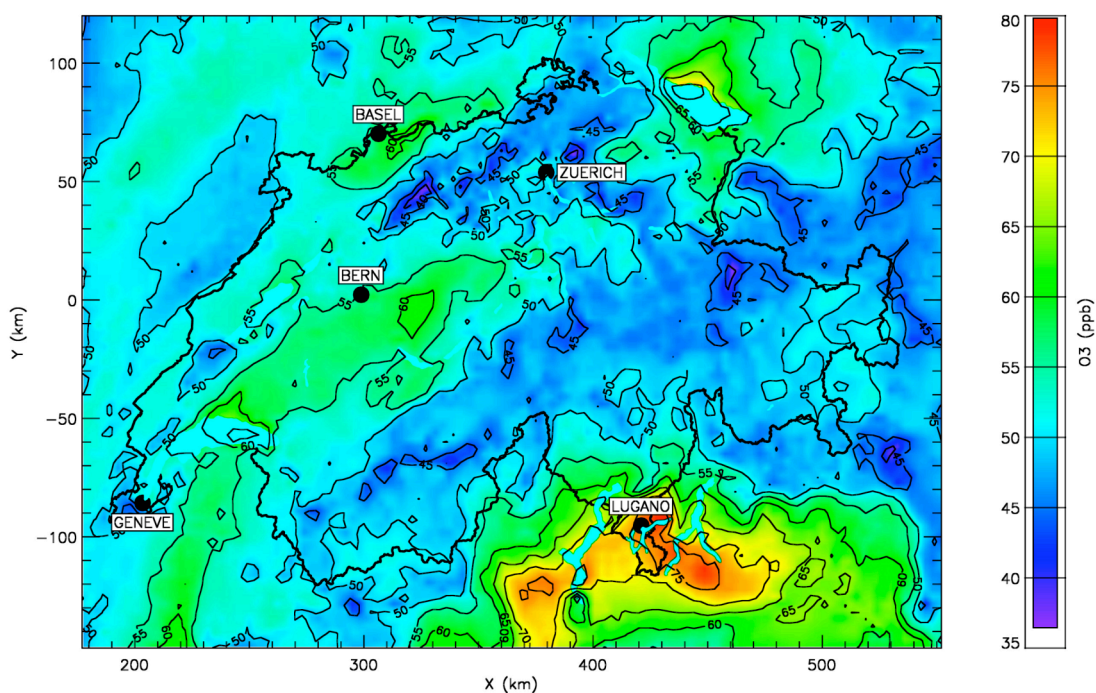


Figure 6.2.3: The highest predicted ozone concentrations (ppb) on 15 June 2006, 15:00 UTC.

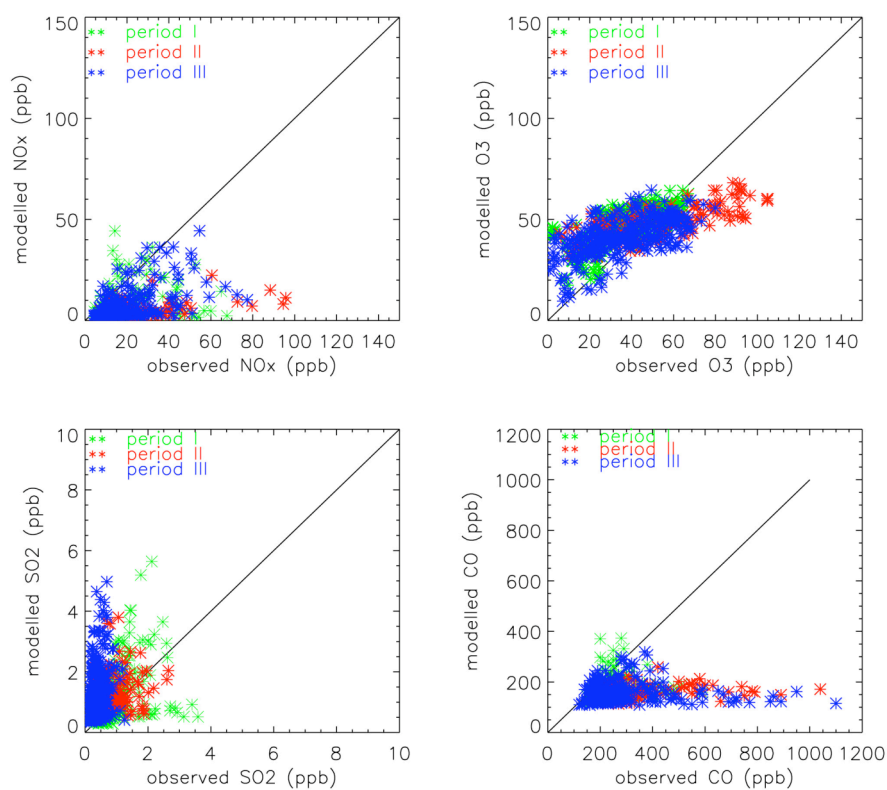


Figure 6.2.4. Modelled versus observed concentrations of NO_x, O₃, SO₂ and CO (ppb) at Zurich in June 2006.

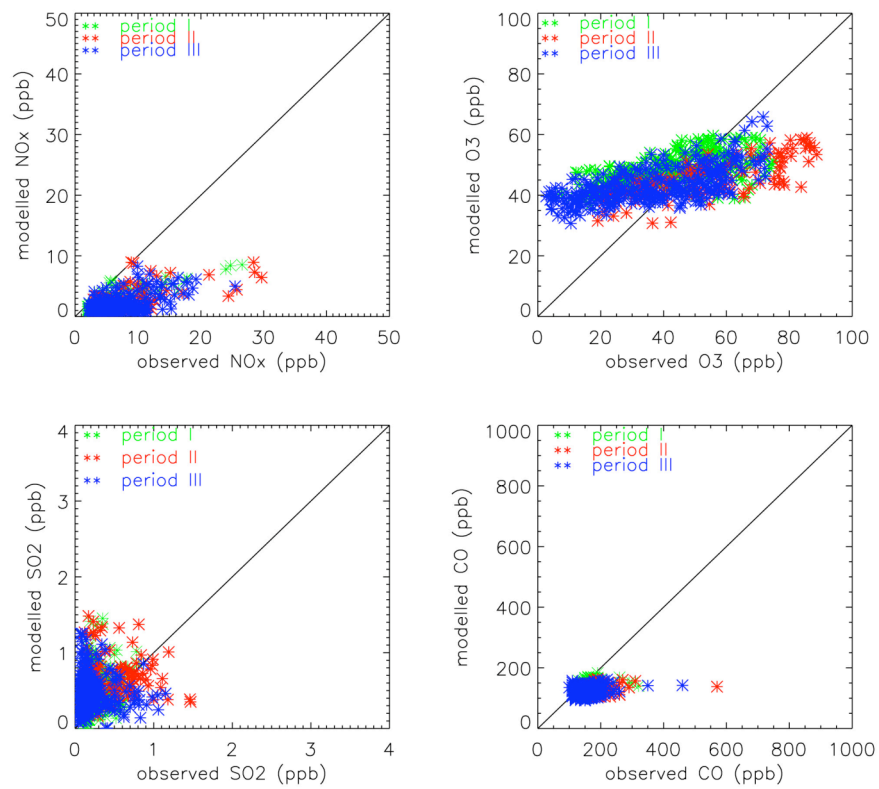


Figure 6.2.5. Modelled versus observed concentrations of NO_x, O₃, SO₂ and CO (ppb) at Payerne in June 2006.

Table 6.2.1: Statistics for ozone concentrations in June 2006. The ranges recommended by US EPA (1991) are ± 5 -15 % for MNBE and 30-35 % for MNGE. Bold letters show where the model performance criteria are met according to the US EPA regulations.

Station	Type	Altitude m a.s.l.	Observed mean	Predicted mean	predicted/ observed	MNBE (%)	MNGE (%)	RMSE (ppb)	Correlation Coefficient r
Basel	suburban	320	48.9	48.7	0.99	237	256	15.5	0.635
Bern	urban	540	36.3	50.9	1.40	88.4	91.5	19.7	0.538
Chaumont	rural	1140	55.5	49.6	0.89	-7.30	16.1	12.8	0.398
Davos	alpine	1669	55.8	47.9	0.86	-11.0	18.1	13.0	0.057
Duebendorf	suburban	430	51.6	49.2	0.95	11.4	34.2	16.9	0.460
Haerkingen	motorway	430	42.1	47.4	1.12	77.1	91.0	17.5	0.574
Jungfrauoch	alpine	3580	60.7	49.4	0.81	-16.8	20.0	14.6	-0.025
Laegern	rural	732	55.5	49.4	0.89	-3.86	23.0	15.9	0.417
Lausanne	urban	530	39.3	51.3	1.30	49.0	50.9	15.8	0.626
Lugano	urban	280	67.3	52.8	0.78	-14.6	24.1	23.0	0.646
Magadino	rural	200	63.8	49.5	0.78	-15.8	24.0	22.3	0.579
Payerne	rural	490	52.7	48.8	0.93	2.29	25.9	14.2	0.481
Rigi	elevated	1030	58.1	51.4	0.88	-7.16	21.0	14.7	0.410
Sion	motorway	480	46.7	48.4	1.04	29.5	47.3	16.5	0.436
Taenikon	rural	540	53.3	50.2	0.94	2.66	24.5	15.4	0.414
Zurich	urban	410	49.6	50.2	1.01	20.2	38.5	16.4	0.516

6.3 Aerosols

The total aerosol concentrations calculated by the model refer to the particles smaller than 2.5 μm (PM_{2.5}). The daily concentrations of PM₁, PM_{2.5} and PM₁₀ were measured on filters at NABEL station Payerne. Figure 6.3.1 shows the daily average concentrations for PM₁, PM_{2.5} and PM₁₀ as well as the modelled hourly average concentrations of PM_{2.5}. All measurements with different size fractions and model predictions look very similar during the first period between 1 and 12 June although they refer to different particle size. After the first period, measurements show an increasing trend and the difference in concentrations of different sizes is noticeable with PM₁₀ being highest. However, model results remain low.

There are other PM₁₀ measurements with higher time resolution (Figure 6.3.2). The model results were compared also with those PM₁₀ measurements as well as the high-resolution AMS data, which refer to PM₁ fraction. The collection efficiency of AMS in this period was 1. The AMS measurements (PM₁) and model results (PM_{2.5}) are close to each other, whereas PM₁₀ values lie slightly over them during the first 12 days, indicating that particles were mainly in the smaller size fraction. Both PM₁ and PM₁₀ measurements show an increase during the low-wind period, while model results fail to follow it. Very high PM₁₀ levels around 20 June are most likely due to the strong Saharan dust event observed at that time. The aerosol concentrations dropped during the last week of June. We can see the detailed results for inorganic and organic aerosols in Figs. 6.3.3 - 6.3.5. The model underestimates aerosol concentrations during the low wind period (12-17 June). Model predictions for the first 12 days are reasonably good. However, the modelled particulate concentrations are higher than measured values during the first 7 days especially for nitrate. The total nitrate concentrations averaged over the first 7 days (Figure 6.3.4) suggest that model had more particulate nitrate during that time. The average predicted a concentration is 0.81 mg N m⁻³ whereas the average of measured total nitrate is 0.50 mg N m⁻³. Considering the overestimated wind speed by the model during the first 7 days (see Fig. 6.1.1) transport of precursors from another site might be a reasonable explanation for the overestimated nitrate and sulphate levels at Payerne at the beginning of June. On the other hand, the results look different for the organic aerosols (Fig. 6.3.5). The model results are slightly lower than the AMS measurements during the first week, but then measurements show an increase. They are about 3 times higher than the modelled values during 12-17 June. Analysis of AMS data indicates that more than 80% of the organic aerosol mass is secondary at Payerne. It seems that model can reproduce the primary organic aerosol concentrations reasonably well, fails however, to predict secondary organic aerosols. In addition to the problems of meteorological model for the low wind period, some other causes might lead to underestimation. The SOA formation from other sources (sesquiterpenes) and oligomerization, which are not yet treated in the model, are likely to be some of the reasons. The predicted concentrations for EC are very close to the measured ones in the first period (Fig. 6.3.6). They are underestimated in the second period. Measurements indicate elevated EC concentrations during the Saharan event on 20 June.

The locations of highest aerosol concentrations predicted by the model are evident from Figures 6.3.7-6.3.11. The elevated particulate concentrations are along the Swiss Plateau and in the area between southern Switzerland and northern Italy.

The absolute and fractional compositions of modelled and measured aerosols in whole June 2006 as well as in three periods are shown in Fig. 6.3.12. The largest difference

between observations and predictions is in the low-wind period II. The best agreement is obtained in Period I. Both measurements and model predictions suggest that the main components of the aerosols in June are organic compounds by about 60%, although model underestimates organic aerosol concentrations. Inorganic aerosols and EC could be predicted reasonably well. The scatter plots show clearly that model underestimates the particulate concentrations in the low-wind period II (Fig. 6.3.13). Organic aerosols are underestimated over the whole episode.

The statistical parameters of particles were calculated for each of the periods in June 2006 in Payerne (Table 6.2). The model performance criteria recommended by *Boylan and Russell* (2006) are met between 2 and 11 June for all particulate species except organic aerosols and particulate nitrate. The best performance criteria have been obtained for EC. All species have their worst performance between 12 and 16 June when the wind speed was low.

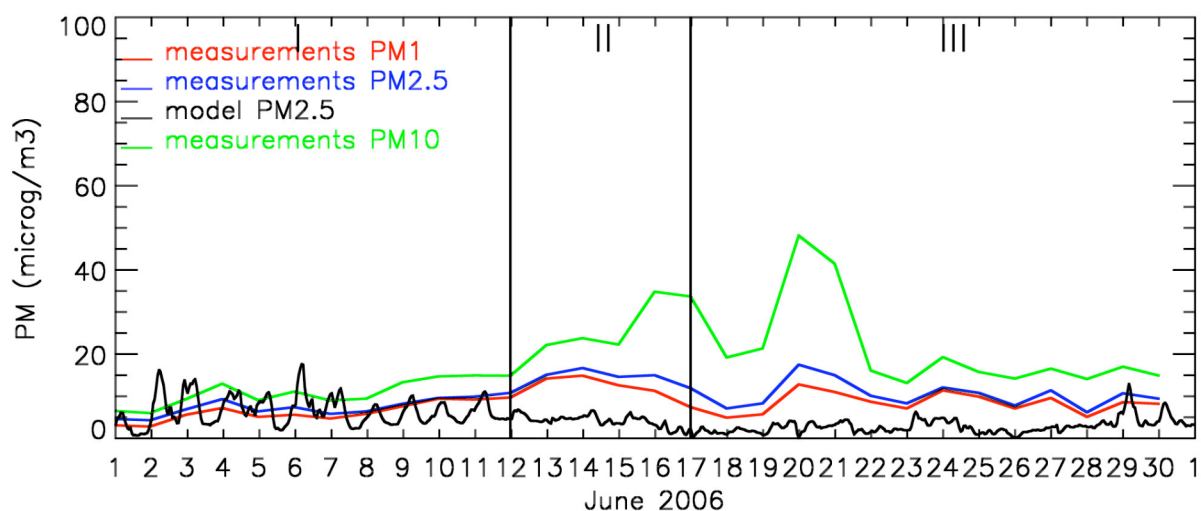


Figure 6.3.1: Comparison of PM1, PM2.5 and PM10 (daily filter measurements), and PM2.5 (model) at Payerne, in June 2006 ($\mu\text{g m}^{-3}$)

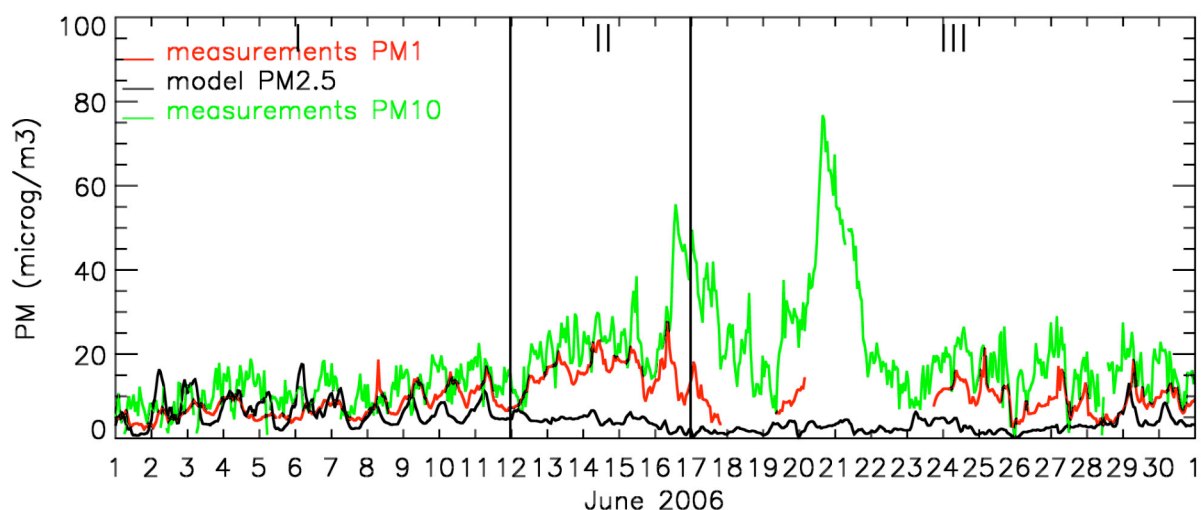


Figure 6.3.2: Comparison of PM1 (AMS measurements), PM2.5 (model) and PM10 (NABEL measurements) at Payerne in June 2006 ($\mu\text{g m}^{-3}$)

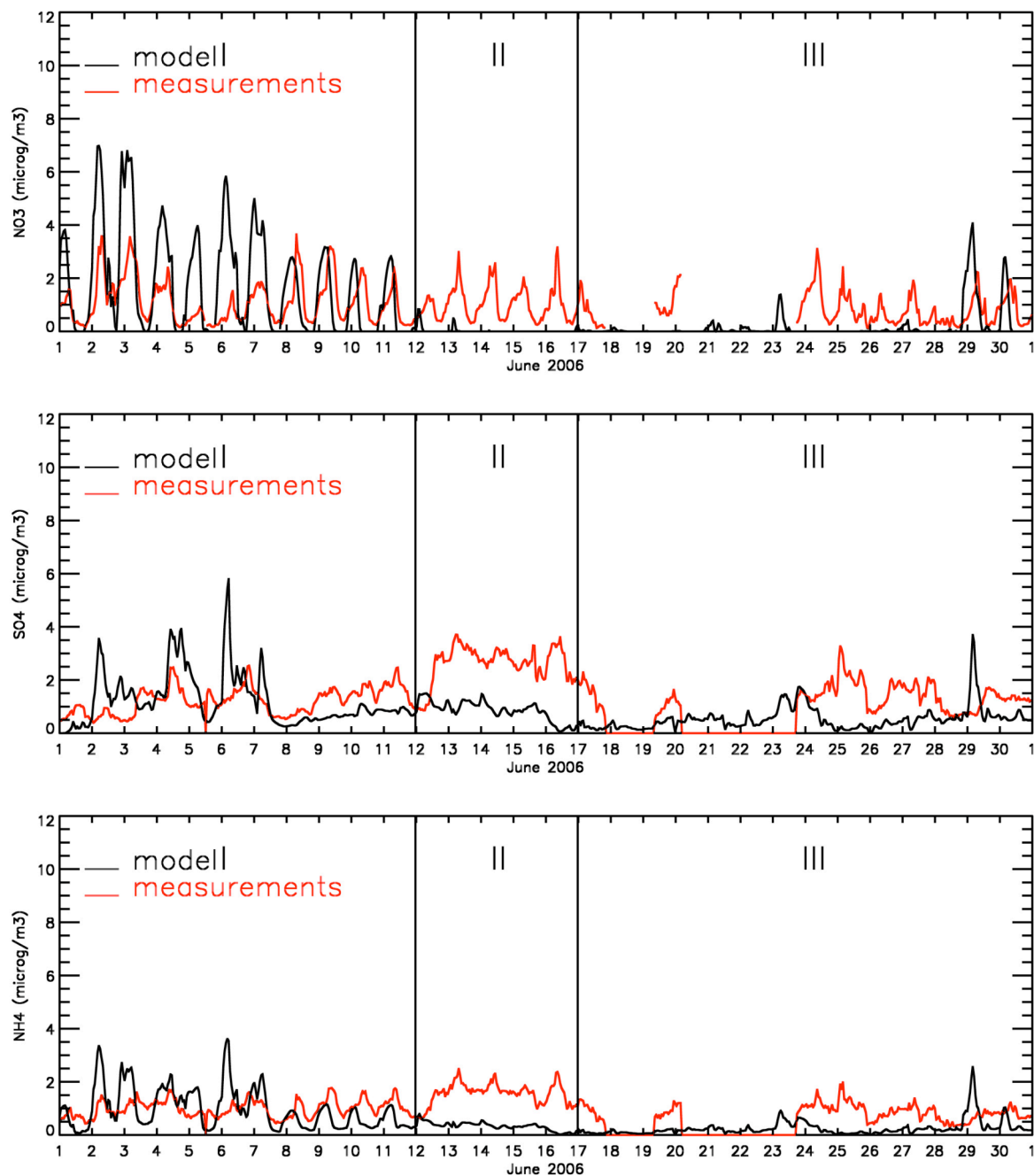


Figure 6.3.3: Comparison of modelled and measured inorganic aerosols ($\mu\text{g m}^{-3}$) at Payerne in June 2006.

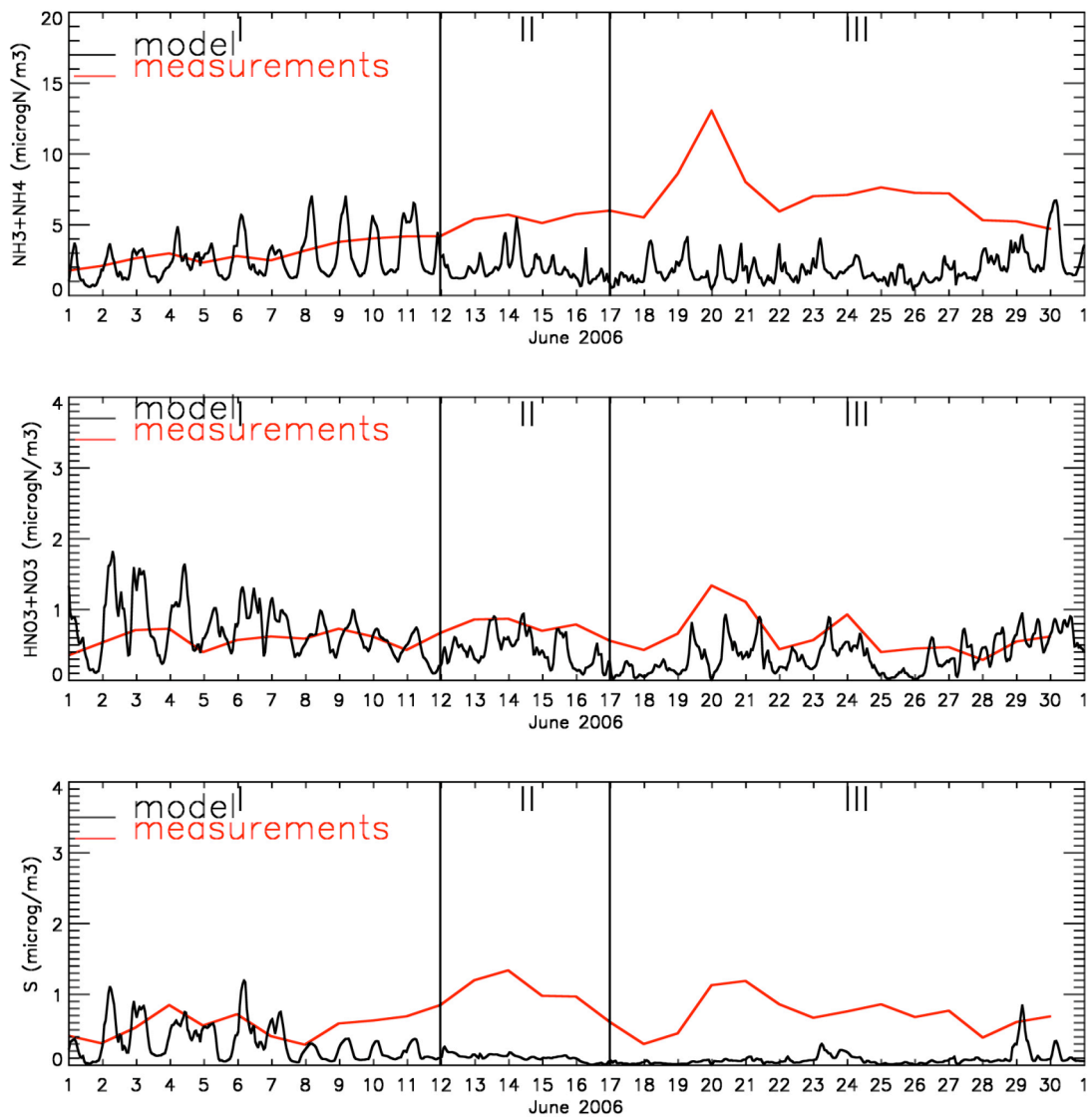


Figure 6.3.4: Comparison of modelled and measured total ammonia (upper panel), total nitrate ($\mu\text{g N/m}^3$) (middle panel) and S ($\mu\text{g m}^{-3}$) (lower panel) at Payerne in June 2006.

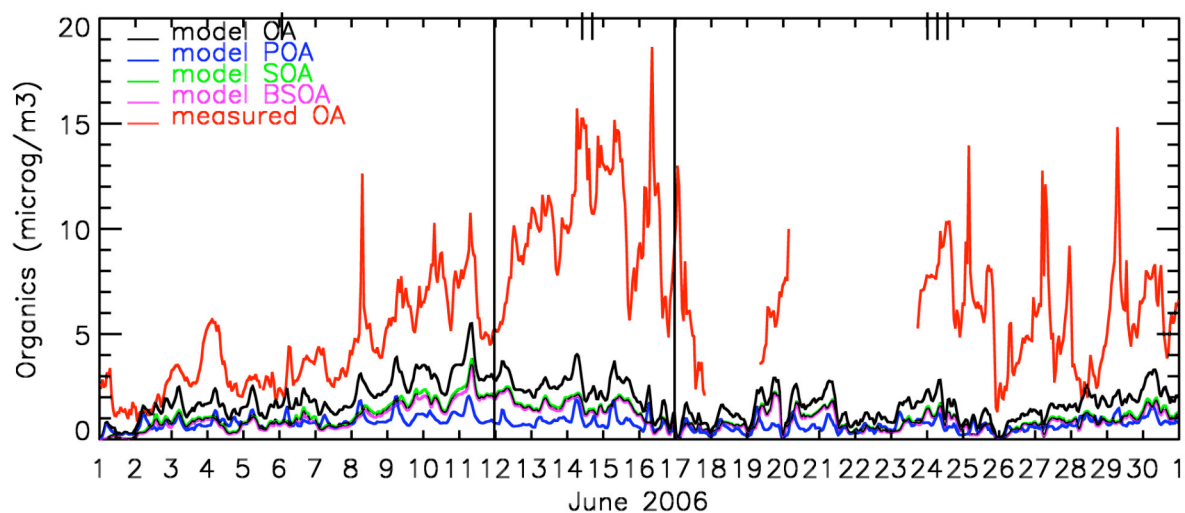


Figure 6.3.5: Comparison of modelled and measured organic aerosols ($\mu\text{g m}^{-3}$) at Payerne in June 2006.

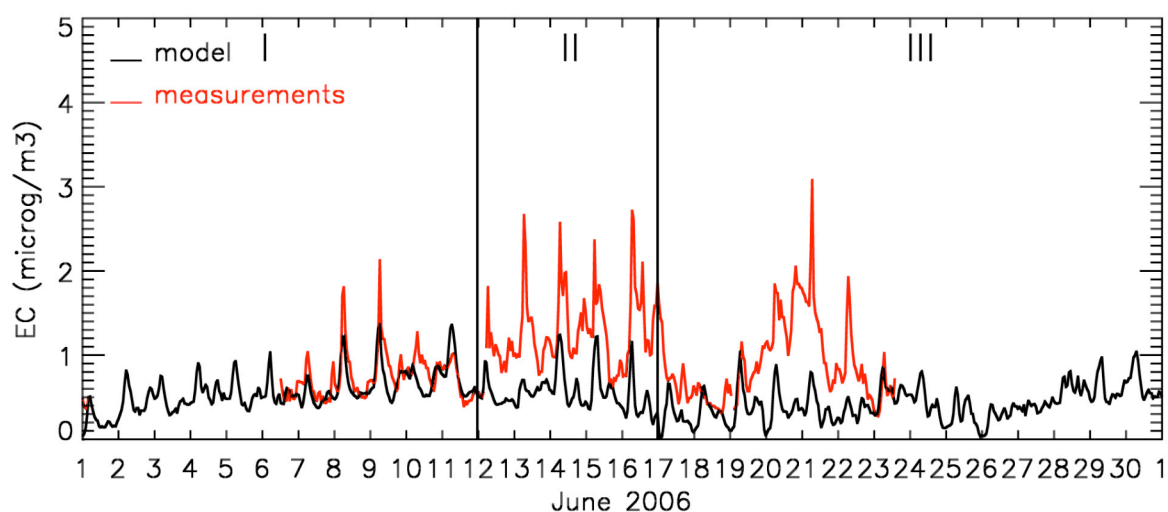


Figure 6.3.6: Comparison of modelled and measured Elemental Carbon, EC ($\mu\text{g m}^{-3}$) at Payerne in June 2006.

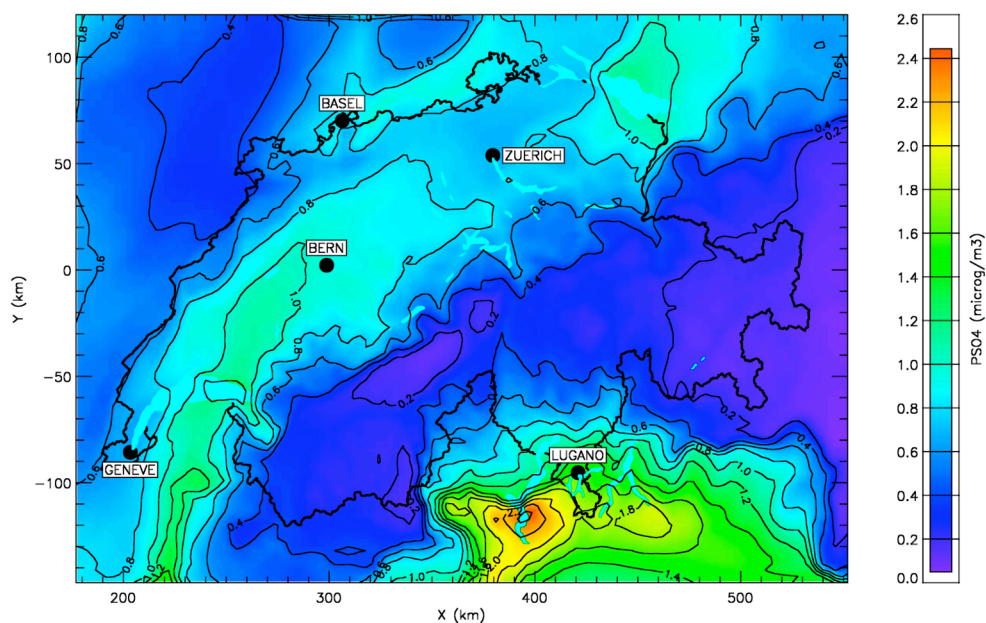


Figure 6.3.7: The highest predicted concentrations of particulate sulphate (SO_4) ($\mu\text{g m}^{-3}$) on 15 June 2006, 16:00 UTC.

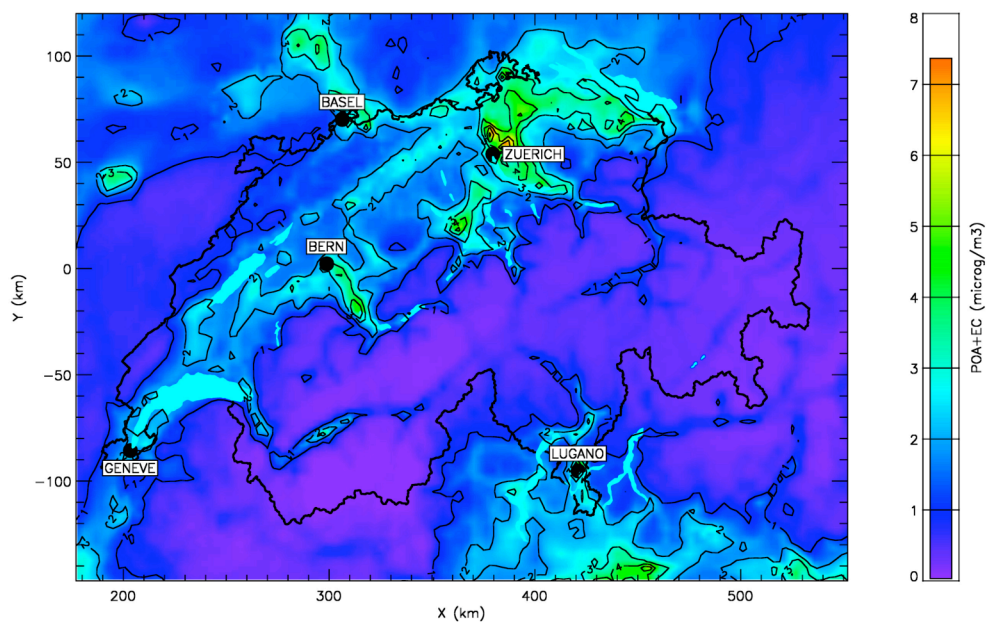


Figure 6.3.8: The highest predicted concentrations of primary aerosols (POA+EC) ($\mu\text{g m}^{-3}$) on 15 June 2006, 06:00 UTC.

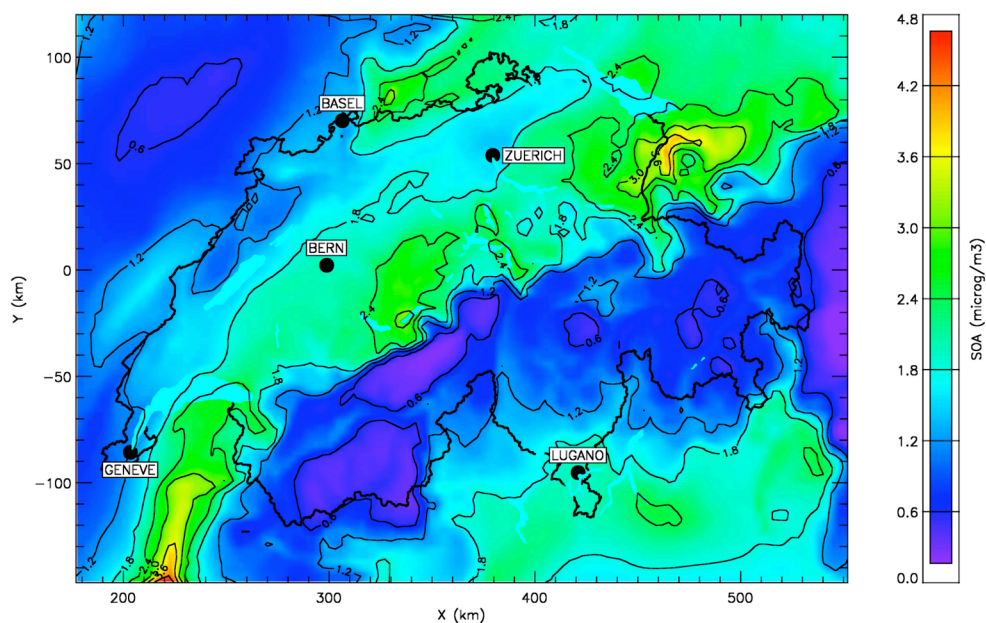


Figure 6.3.9: The highest predicted concentrations of secondary organic aerosols (SOA) ($\mu\text{g m}^{-3}$) on 15 June 2006, 16:00 UTC.

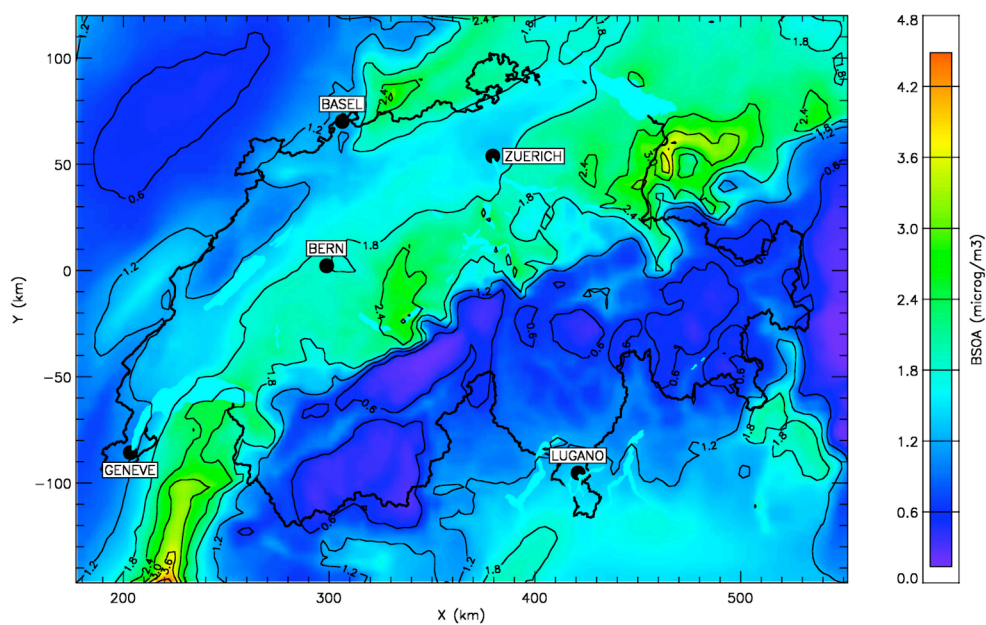


Figure 6.3.10: The highest predicted concentrations of biogenic secondary organic aerosols (BSOA) ($\mu\text{g m}^{-3}$) on 15 June 2006, 16:00 UTC.

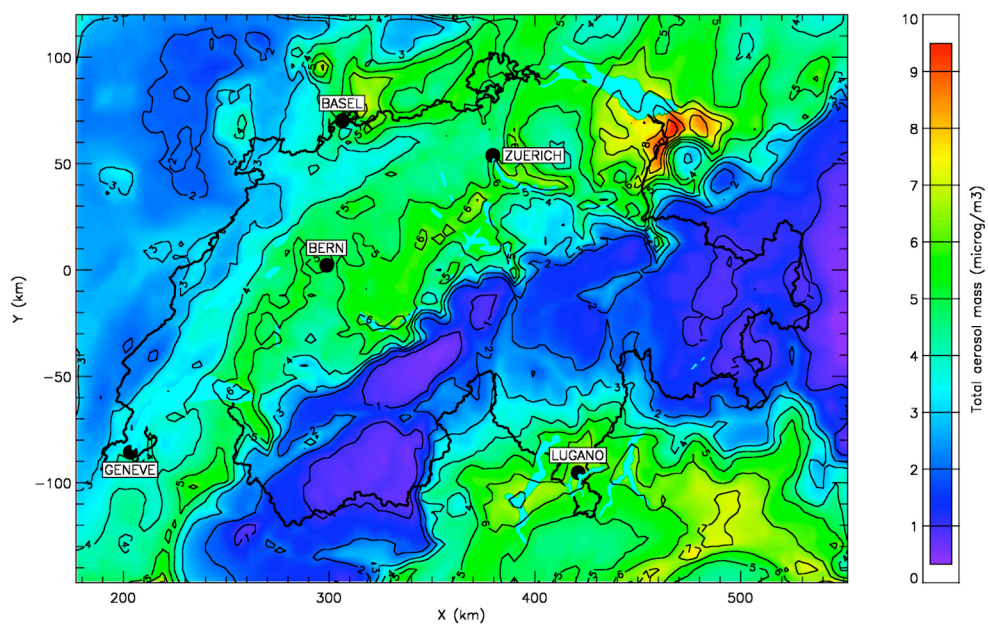


Figure 6.3.11: The highest predicted concentrations of total aerosol mass concentration ($\mu\text{g m}^{-3}$) on 15 June 2006, 18:00 UTC.

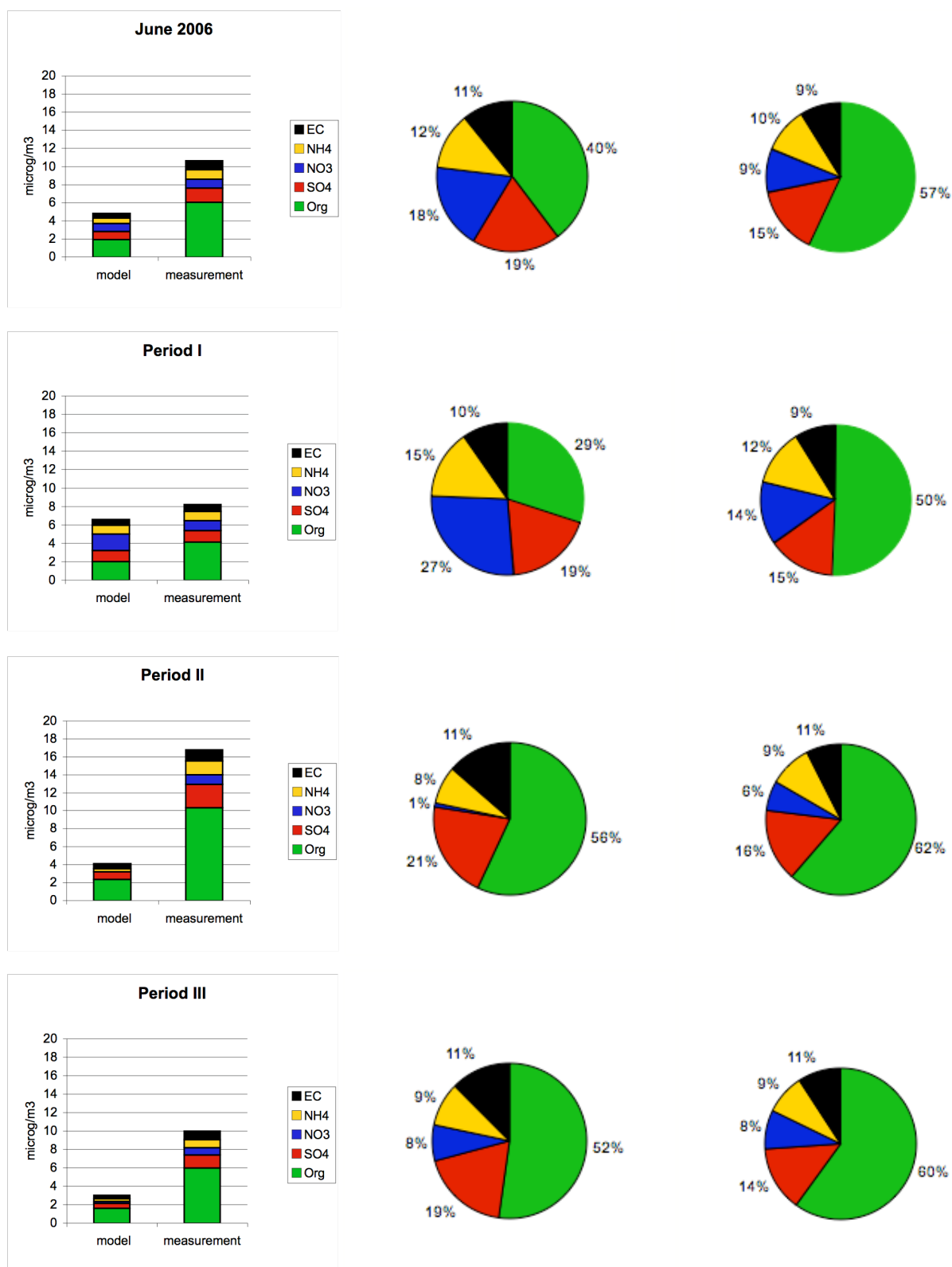


Figure 6.3.12: Comparison of absolute (left) as well as the fractional composition of modelled (middle) and measured (right) aerosols at Payerne in June 2006. From top to down: whole June 2006, 1-11 June, 12-16 June, 17-30 June.

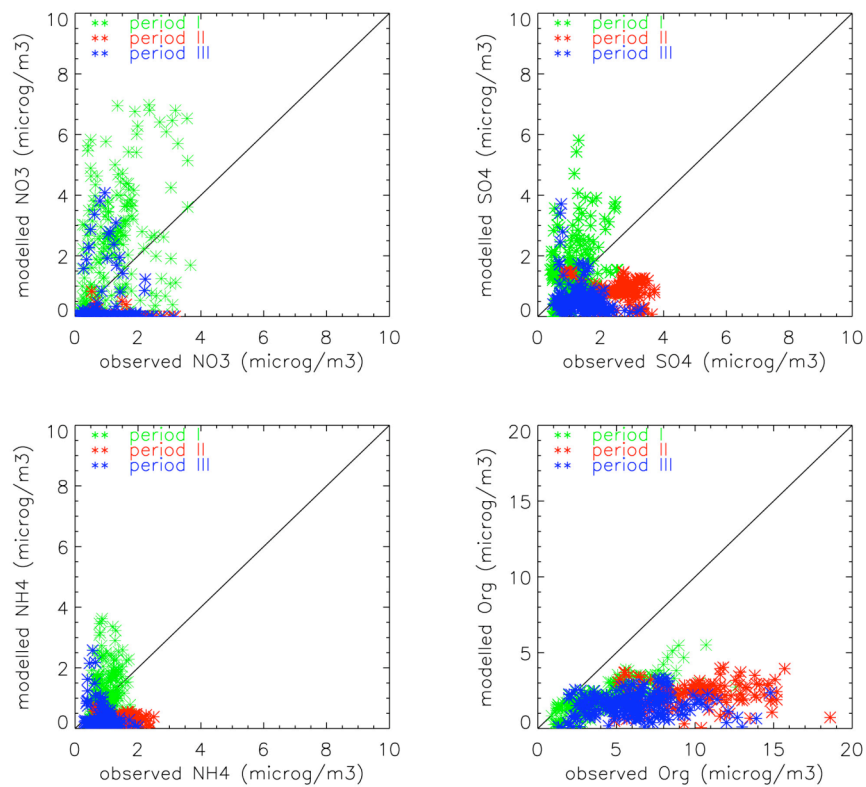


Figure 6.3.13. Modelled versus observed concentrations of inorganic and organic aerosols ($\mu\text{g m}^{-3}$) at Payerne in June 2006.

Table 6.3.1: Statistical parameters for aerosol components for June 2006 at Payerne. The bold numbers indicate the time when the model performance criteria are met ($MFE \leq +75\%$ and $MFB \leq \pm 60\%$).

species	time	Number of data	observed mean ($\mu\text{g m}^{-3}$)	predicted mean ($\mu\text{g m}^{-3}$)	pred./obs.	RMSE	Correlation Coefficient r	MFB (%)	MFE (%)
NO ₃	2-11 June	264	1.11	1.78	1.60	1.82	0.423	-25	115
	12-16 June	121	1.04	0.03	0.03	1.21	-0.069	-190	192
	17-30 June	213	0.808	0.225	0.28	1.06	0.075	-165	179
	whole June	598	0.990	0.871	0.88	1.47	0.341	-108	153
SO ₄	2-11 June	264	1.21	1.22	1.00	1.01	0.225	-22	68
	12-16 June	121	2.62	0.85	0.32	1.97	-0.281	-100	107
	17-30 June	213	1.40	0.56	0.40	1.16	-0.276	-90	99
	whole June	598	1.56	0.91	0.58	1.31	-0.048	-62	87
NH ₄	2-11 June	264	1.00	0.97	0.98	0.78	0.178	-27	66
	12-16 June	121	1.56	0.33	0.21	1.32	-0.258	-128	129
	17-30 June	213	0.87	0.27	0.32	0.78	-0.231	-113	124
	whole June	598	1.07	0.59	0.56	0.92	-0.030	-78	99
Organics	2-11 June	264	4.13	1.98	0.48	2.62	0.807	-69	70
	12-16 June	121	10.3	2.33	0.23	8.48	0.017	-124	124
	17-30 June	213	5.97	1.57	0.26	5.03	0.123	-113	113
	whole June	598	6.04	1.90	0.32	5.15	0.386	-96	96
EC	2-11 June	137	0.740	0.642	0.87	0.27	0.541	-15	28
	12-16 June	119	1.246	0.556	0.45	0.83	0.184	-73	75
	17-30 June	158	0.915	0.372	0.41	0.74	0.148	-77	82
	whole June	414	0.952	0.514	0.54	0.66	0.165	-55	62

7 Episode 3: January 2007

7.1 Meteorology

The meteorological conditions in January 2007 were different from those of the previous year. Figure 7.1.1 shows the time series of the meteorological quantities and of CO at Payerne where aerosol measurements are available. For the sake of comparison with the analysis of January 2006 discussed in Sec. 5, the data for Zurich are given as well (Figure 7.1.2). Four periods were specified:

Period I: 1-12 January

Period II: 13-16 January

Period III: 17-25 January

Period IV: 26-31 January

In January, Europe was affected by a high-pressure system over the Iberian Peninsula bringing warm and humid maritime tropical air from low latitudes of the Atlantic Ocean. Temperatures were above zero most of the time except in the fourth week. The wind speed was moderate to strong until 12 January (period I) and then decreased (period II). Winds were again slightly stronger after 17 January and remained variable (period III). The wind speed decreased again in the last period (IV). The low-wind period between 13 and 16 January (period II) was dry and temperatures were above zero. The measured and modelled CO concentrations agree well with each other during the first 12 days. The deviations from the measured values occur whenever the wind speed decreases (13-17, 22, 26-31 January). As we discussed in Section 5, the performance of the MM5 model seems to become worse under low-wind conditions. Unlike January 2006, there was no pollution episode where CO built up over periods of many days. In period II three isolated peaks were observed. Another peak was observed on 28 January at midnight (period IV). Model predictions of key meteorological variables for air pollution in winter, such as wind direction, vertical profile of potential temperature and precipitation were very good. However, the model did not capture the observed peaks. This indicates that even with good meteorological predictions, sharp peaks cannot be reproduced at a model resolution of a few kilometres.

Figures A15 to A21 in the Appendix show the time series of surface wind velocity, wind direction, air temperature, specific humidity, global irradiance, planetary boundary layer height, and precipitation rate at CHA, PAY, KLO, STG, SIO and MAG for domain 3. Again, wind speed at the mountain station CHA is strongly under-predicted by both models. The degree of agreement is similar to that in January 2006. The low wind time interval from 4 to 11 January is more evident at SIO and MAG than at stations north of the Alps. Wind directions at those northern sites are surprisingly well captured. Specific humidity modelled by MM5 agrees less than in January 2006. Like in the previous year MM5 has difficulties to predict realistic PBL heights. The predicted timing of precipitation is not as good as in January 2006.

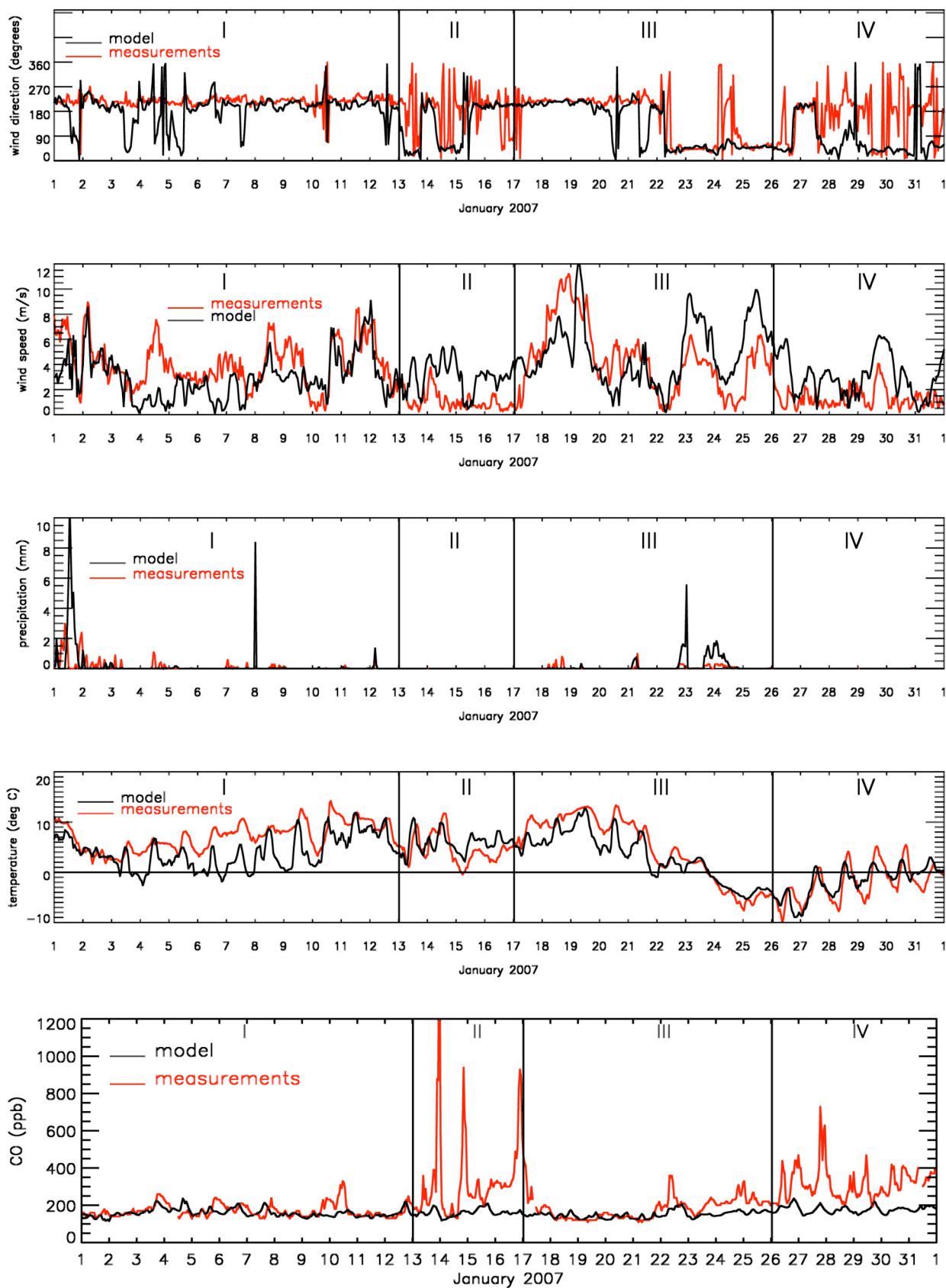


Figure 7.1.1: Comparison of measured and modelled wind direction (degrees), wind speed (m s^{-1}), precipitation (mm) and temperature (C) as well as CO concentrations (ppb) at Payerne (NABEL station) in January 2007.

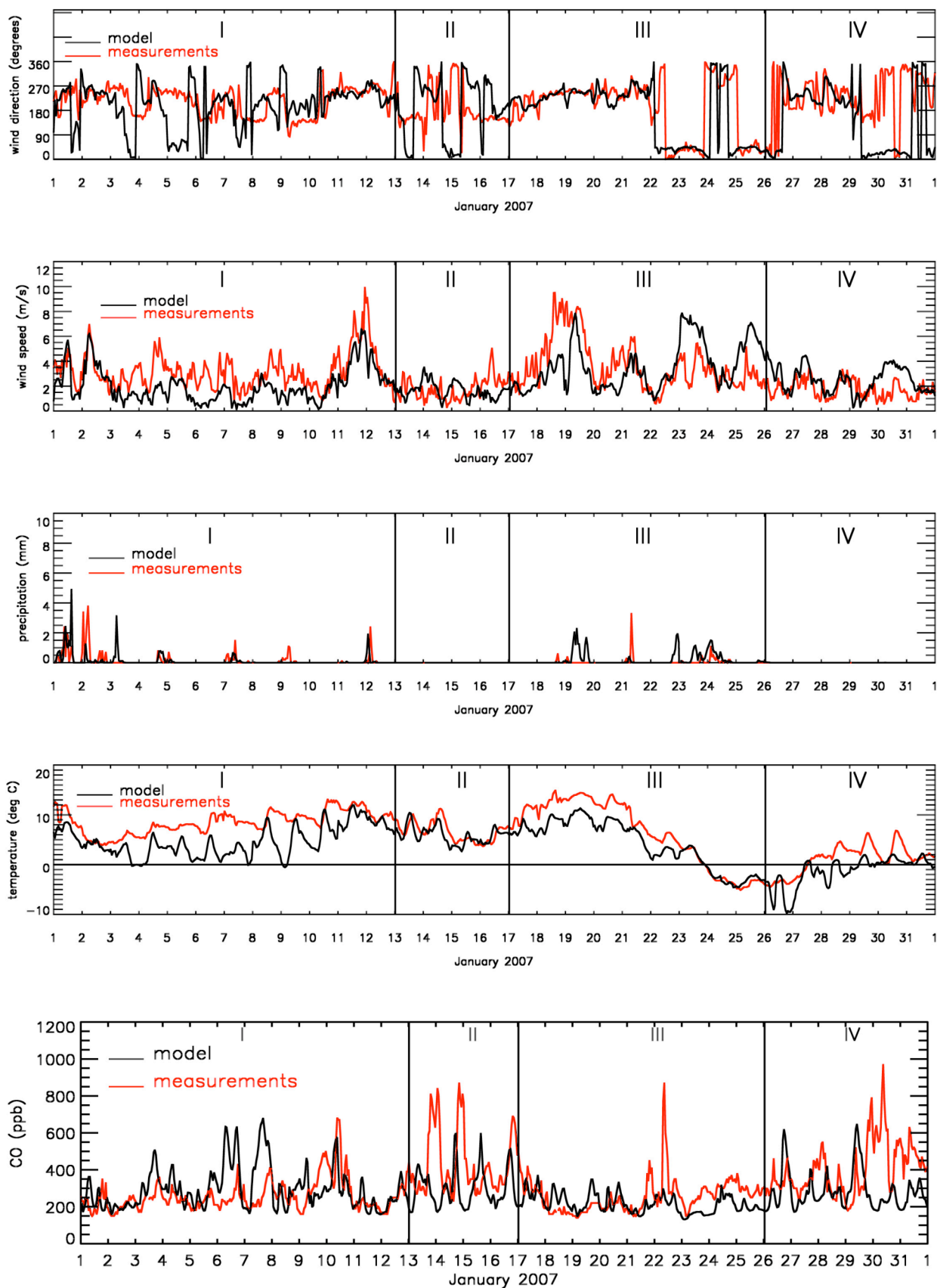


Figure 7.1.2: Comparison of measured and modelled wind direction (degrees), wind speed (m s^{-1}), precipitation (mm) and temperature (C) as well as CO concentrations (ppb) at Zurich (NABEL station) in January 2007

The performance of wind speed is best in the high wind periods I and III (Table 7.1.1). COSMO 7 data are better correlated and are afflicted with smaller errors than MM5 results. This is also true for wind direction. The variability of DIST is similar to the values found for 2006.

The mean observed temperatures during the periods I - III are 4 to 6°C, i.e. higher than in January 2006. Modelled and measured temperatures match best in period III ($r > 0.84$). MM5 data have better performance than COSMO 7 data in all periods. There is evidence that the bias is more negative in less cold winter periods. Specific humidity is also best correlated in the third period, but in general more biased than in the previous winter. Finally, the performance of irradiance is similar to that obtained in January - February 2006.

7.2 Gaseous pollutants

The modelled concentrations of some gaseous compounds are compared with measurements at Payerne and Zurich in Figures 7.2.1 and 7.2.2, respectively. The NO_x concentrations at Payerne are relatively low and the model could reproduce them reasonably well in the first and the third periods. The model underestimates them in the second and the fourth periods. On the other hand, the modelled ozone concentrations are higher than observed levels. Slightly higher SO₂ concentrations were predicted by the model as seen in the other episodes. At the urban site Zurich, the model predictions for NO_x concentrations are good during the first period. It is quite obvious that the disagreement between predictions and observations occur each time when the wind speed goes down. The model predicts too high SO₂ concentrations at Zurich as well. This could be related to the emissions.

In Figures 7.2.3 and 7.2.4, predictions versus observations are plotted for each period at Payerne and Zurich, respectively. The overestimation of ozone and SO₂ is clearly seen. In case of NO_x and CO, the deviation from the perfect correlation line occurs mainly in the low-wind periods.

Table 7.1.1: Mean observation MOBS, mean bias error MBE and its 95% confidence interval, mean gross error MGE, correlation coefficient r and direction weighted wind error DIST of modelled vs. measured meteorological quantities measured at 14 ANETZ stations. Periods of January 2007 episode, domain 3. FFSFC: wind speed ($m s^{-1}$), DDSFC: wind direction ($^{\circ}$), UVSFC: wind vector (for dist) ($m s^{-1}$), TSFC: air temperature ($^{\circ} C$), QSFC: specific humidity ($kg kg^{-1}$), G: global irradiance ($W m^{-2}$). See text for details.

variable	model	period	MOBS	MBE	Δ MBE	MGE	r	DIST
FFSFC	MM5	1-12 Jan 2007	2.39	0.14	0.08	1.59	0.36	n.a.
FFSFC	COSMO	1-12 Jan 2007	2.41	1.07	0.08	1.41	0.75	n.a.
FFSFC	MM5	13-16 Jan 2007	1.18	1.01	0.11	1.49	0.05	n.a.
FFSFC	COSMO	13-16 Jan 2007	1.16	0.59	0.11	0.97	0.46	n.a.
FFSFC	MM5	17-25 Jan 2007	2.93	0.58	0.10	2.04	0.43	n.a.
FFSFC	COSMO	17-25 Jan 2007	2.96	0.89	0.12	1.55	0.74	n.a.
FFSFC	MM5	26-31 Jan 2007	1.42	1.18	0.11	1.76	0.09	n.a.
FFSFC	COSMO	26-31 Jan 2007	1.43	0.57	0.12	1.15	0.39	n.a.
DDSFC	MM5	1-12 Jan 2007	n.a.	65.5	n.a.	65.5	n.a.	n.a.
DDSFC	COSMO	1-12 Jan 2007	n.a.	48.3	n.a.	48.3	n.a.	n.a.
DDSFC	MM5	13-16 Jan 2007	n.a.	77.7	n.a.	77.7	n.a.	n.a.
DDSFC	COSMO	13-16 Jan 2007	n.a.	69.7	n.a.	69.7	n.a.	n.a.
DDSFC	MM5	17-25 Jan 2007	n.a.	56.3	n.a.	56.3	n.a.	n.a.
DDSFC	COSMO	17-25 Jan 2007	n.a.	49.1	n.a.	49.1	n.a.	n.a.
DDSFC	MM5	26-31 Jan 2007	n.a.	80.1	n.a.	80.1	n.a.	n.a.
DDSFC	COSMO	26-31 Jan 2007	n.a.	67.0	n.a.	67.0	n.a.	n.a.
UVSFC	MM5	1-12 Jan 2007	n.a.	n.a.	n.a.	n.a.	n.a.	2.49
UVSFC	COSMO	1-12 Jan 2007	n.a.	n.a.	n.a.	n.a.	n.a.	2.12
UVSFC	MM5	13-16 Jan 2007	n.a.	n.a.	n.a.	n.a.	n.a.	2.26
UVSFC	COSMO	13-16 Jan 2007	n.a.	n.a.	n.a.	n.a.	n.a.	1.57
UVSFC	MM5	17-25 Jan 2007	n.a.	n.a.	n.a.	n.a.	n.a.	2.87
UVSFC	COSMO	17-25 Jan 2007	n.a.	n.a.	n.a.	n.a.	n.a.	2.36
UVSFC	MM5	26-31 Jan 2007	n.a.	n.a.	n.a.	n.a.	n.a.	2.60
UVSFC	COSMO	26-31 Jan 2007	n.a.	n.a.	n.a.	n.a.	n.a.	1.89
TSFC	MM5	1-12 Jan 2007	5.54	-1.46	0.11	2.97	0.59	n.a.
TSFC	COSMO	1-12 Jan 2007	5.55	-2.75	0.14	3.08	0.78	n.a.
TSFC	MM5	13-16 Jan 2007	4.08	2.34	0.23	3.51	0.32	n.a.
TSFC	COSMO	13-16 Jan 2007	4.08	-2.46	0.35	3.63	0.64	n.a.
TSFC	MM5	17-25 Jan 2007	4.07	-0.27	0.12	2.48	0.86	n.a.
TSFC	COSMO	17-25 Jan 2007	4.17	-2.10	0.22	3.17	0.84	n.a.
TSFC	MM5	26-31 Jan 2007	-1.17	0.89	0.19	3.19	0.58	n.a.
TSFC	COSMO	26-31 Jan 2007	-1.17	-2.07	0.33	3.73	0.53	n.a.
QSFC	MM5	1-12 Jan 2007	0.00471	-0.00084	0.00004	0.00105	0.48	n.a.
QSFC	COSMO	1-12 Jan 2007	0.00471	-0.00038	0.00006	0.00084	0.67	n.a.
QSFC	MM5	13-16 Jan 2007	0.00437	-0.00046	0.00005	0.00078	0.60	n.a.
QSFC	COSMO	13-16 Jan 2007	0.00437	-0.00053	0.00011	0.00098	0.60	n.a.
QSFC	MM5	17-25 Jan 2007	0.00433	-0.00050	0.00004	0.00096	0.66	n.a.
QSFC	COSMO	17-25 Jan 2007	0.00436	-0.00031	0.00006	0.00076	0.77	n.a.
QSFC	MM5	26-31 Jan 2007	0.00280	0.00002	0.00003	0.00054	0.61	n.a.
QSFC	COSMO	26-31 Jan 2007	0.00280	-0.00025	0.00007	0.00076	0.41	n.a.
G	MM5	1-12 Jan 2007	174.7	20.9	8.8	93.0	0.23	n.a.
G	MM5	13-16 Jan 2007	220.7	-40.9	11.8	100.7	0.14	n.a.
G	MM5	17-25 Jan 2007	179.0	-21.9	11.2	85.9	0.47	n.a.
G	MM5	26-31 Jan 2007	262.5	-19.8	9.5	77.1	0.60	n.a.

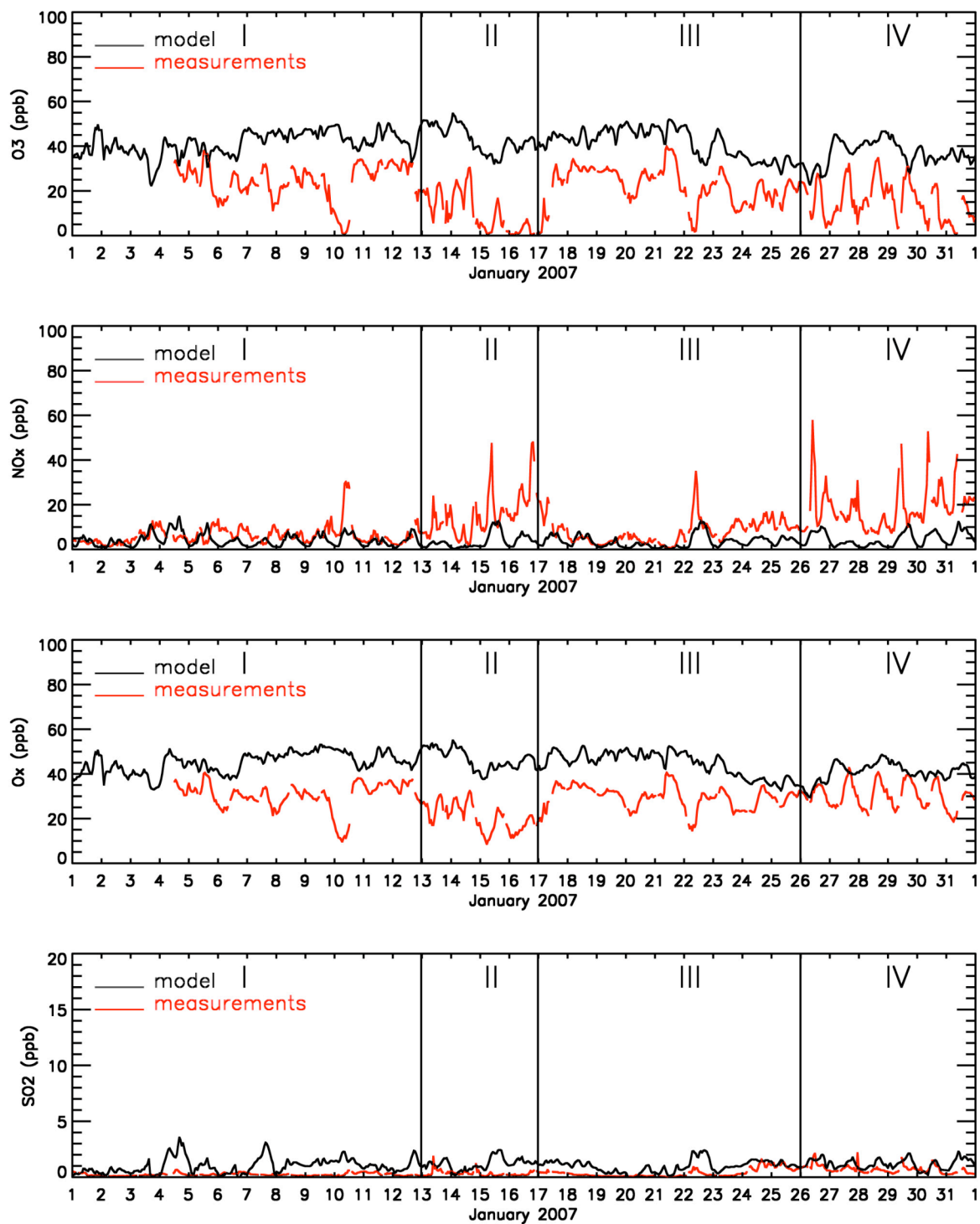


Figure 7.2.1 Comparison of modelled and measured (NABEL) gas-phase species concentrations (ppb) at Payerne in January 2007 ($O_x = O_3 + NO_2$).

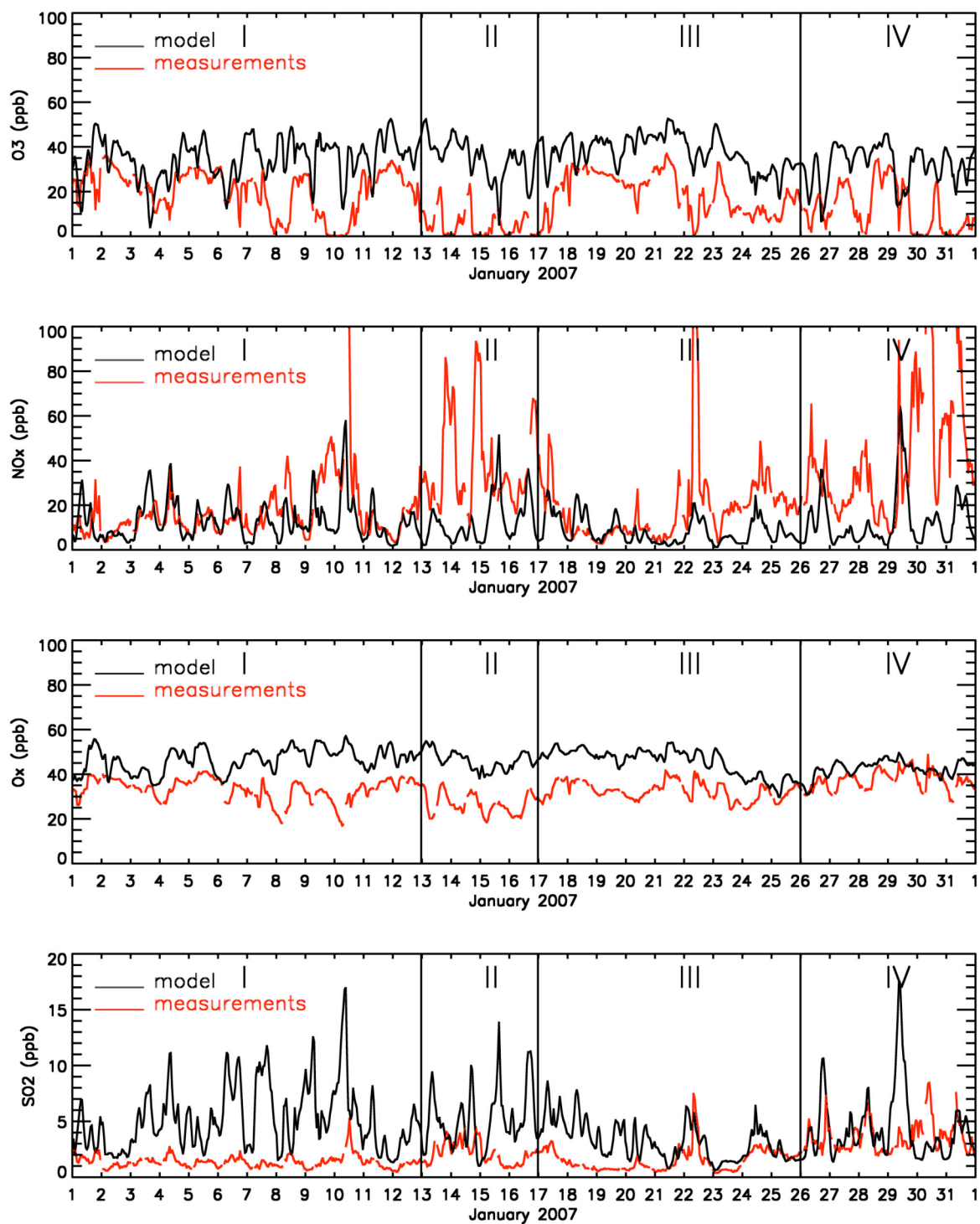


Figure 7.2.2: Comparison of modelled and measured (NABEL) gas-phase species concentrations (ppb) at Zurich in January 2007 ($O_x = O_3 + NO_2$).

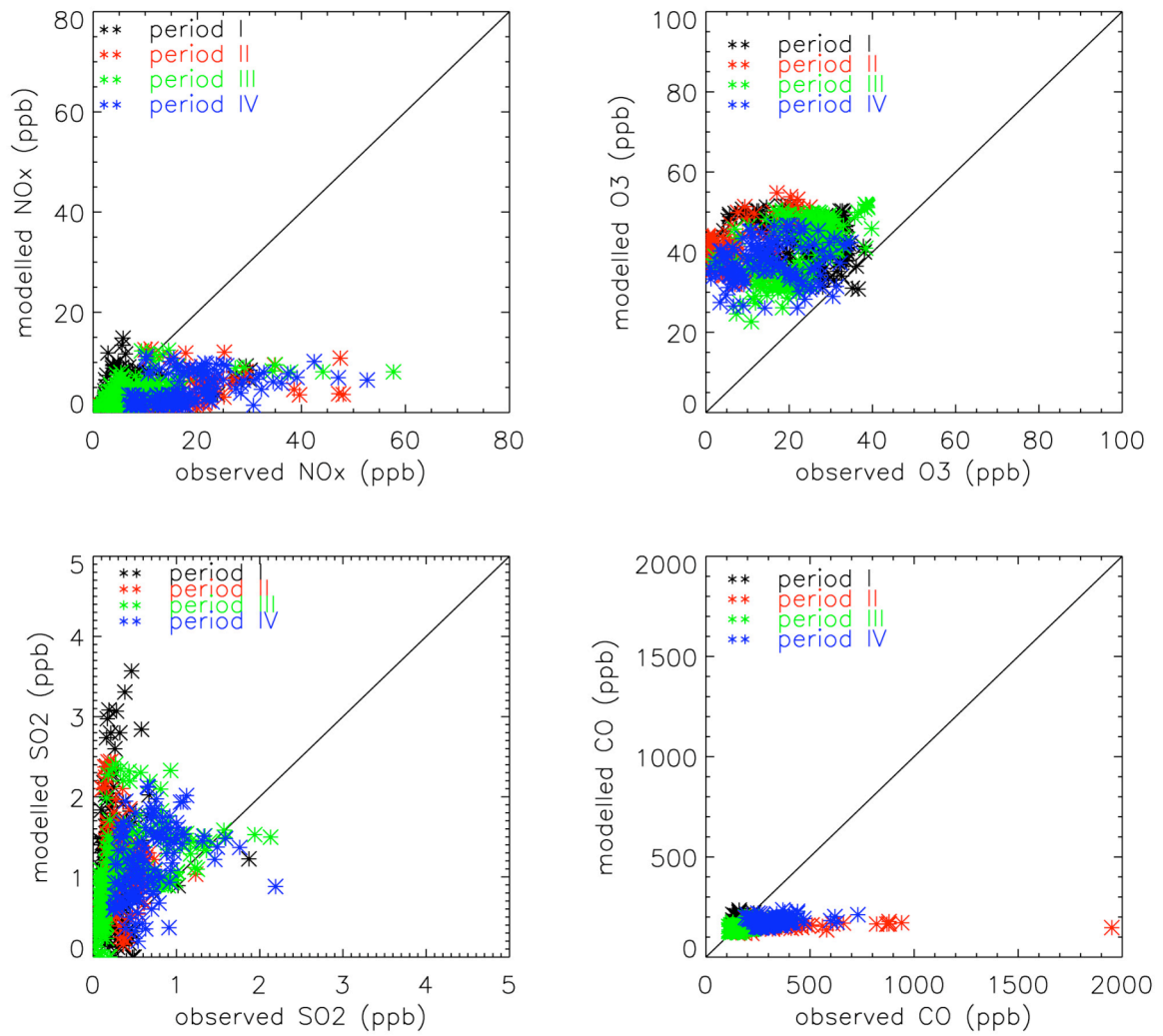


Figure 7.2.3: Modelled versus observed concentrations of NO_x, O₃, SO₂ and CO (ppb) at Payerne in January 2007.

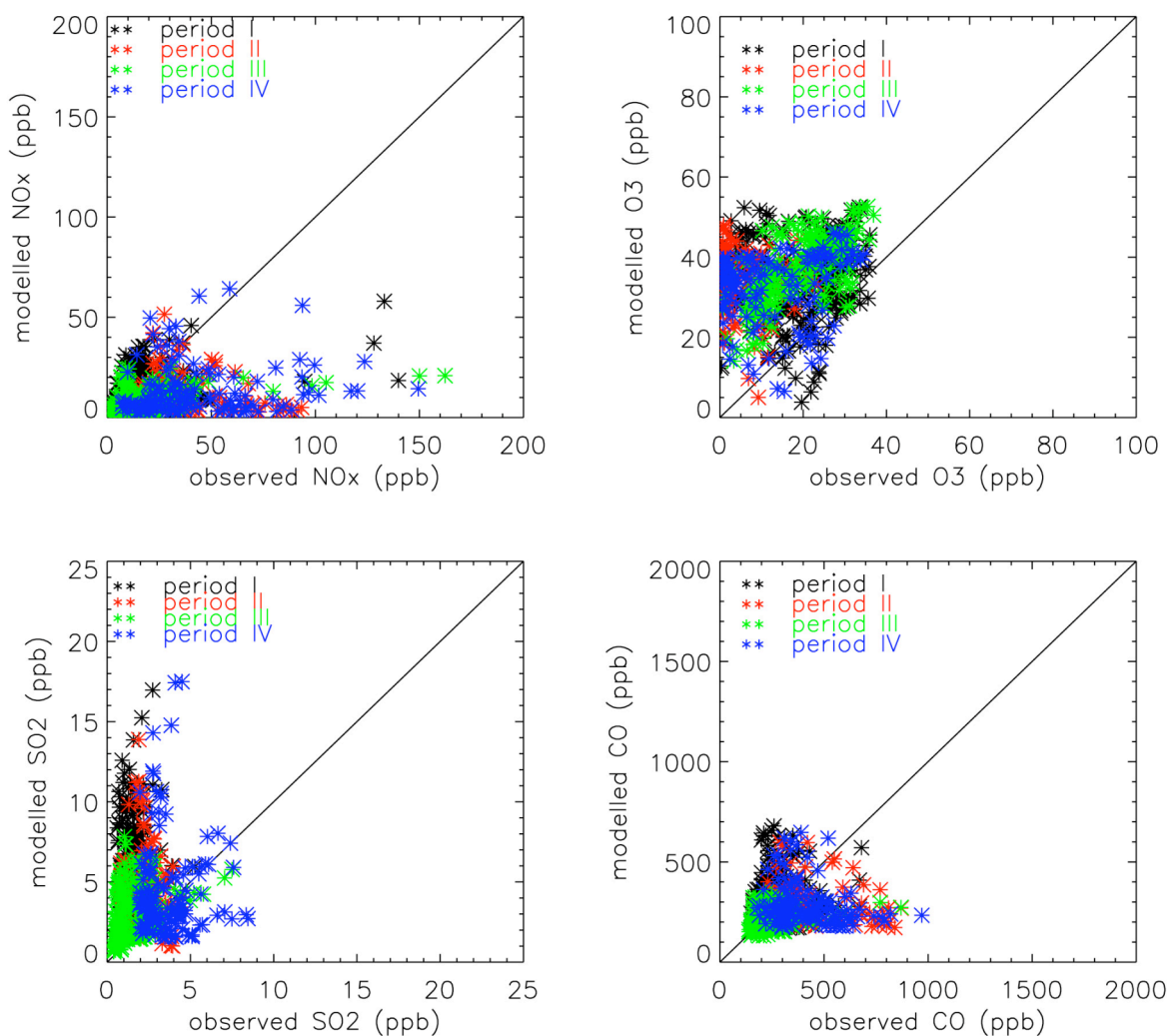


Figure 7.2.4: Modelled versus observed concentrations of NO_x, O₃, SO₂ and CO (ppb) at Zurich in January 2007.

7.3 Aerosols

The AMS measurements were carried out at the monitoring station of Payerne. A collection efficiency of 1 was used in this period. The model results, therefore, were evaluated for that site. A general comparison is done in Figure 7.3.1 using the daily average concentrations measured at Payerne. All measured size fractions (PM₁, PM_{2.5} and PM₁₀) are very close to each other and to the model PM_{2.5} results in the first period. A slight increase in concentration with size can be observed later. The model cannot capture the increased levels in the second and the fourth periods. A more detailed comparison is done with high-resolution data measured at the same station (Fig. 7.3.2). The AMS measurements started on 12 January and covered the rest of the month. There are also PM₁₀ measurements for whole episode. The model PM_{2.5} results are very similar to PM₁₀ measurements during the first period where there was no AMS measurement. In the second period when the wind was low, both PM₁₀ and PM₁ (AMS) measurements show an increase, but model results remain low. A similar case can be seen in the last period. The agreement between the model and measurements is better

during the third period when the wind was higher. As in the case of January 2006, model-measurement agreement seems to depend strongly on wind speed.

Evaluation of individual species gives more detailed information. The inorganic aerosols measured by AMS, are similar to model predictions in the third period (Fig. 7.3.3). However, towards the end of this period and in the following period, agreement becomes worse. Relatively higher inorganic aerosol concentrations in the first period predicted by the model cannot be compared with measurements because there was no AMS data. However, nitrogen in HNO_3 (gaseous) + NO_3 (particulate), NH_3 (gaseous) + NH_4 (particulate) and S in the particle phase were measured during January 2007 at Payerne. These data are daily average values. We compared these quantities with the modelled ones (Fig. 7.3.4). The model results are in general higher in the first week. On the other hand, model-measurement agreement for the rest of the time looks reasonably good, except for total nitrate in the second and the fourth periods.

The comparison of organic aerosols looks very similar to the case in winter 2006 although the concentrations were lower in 2007. The modelled organic aerosol concentrations are lower than the measured ones by AMS, especially in the second and the fourth periods (Fig. 7.3.5). The primary organic aerosols dominate the modelled OA fraction. On the other hand, the measured and modelled EC concentrations agree quite well with each other in the first and third periods (Fig. 7.3.6). Model slightly underestimates EC concentrations in the second and fourth periods.

The graphs of observed versus predicted aerosol concentrations shown in Figure 7.3.7 indicate that the deviation from the perfect correlation line occurs mainly in the second and fourth periods with prevailing low-wind conditions.

The highest particulate nitrate concentrations were predicted at night in Swiss Plateau especially around Basel (Fig. 7.3.8). Distribution of elevated sulphate levels look similar. However, much higher concentrations in northern Italy is noticeable (Fig. 7.3.9). Primary aerosols are especially high in northern Italy (Fig. 7.3.10). In general, aerosol concentrations are relatively higher in the Swiss Plateau and in northern Italy (Fig. 7.3.11).

A comparison of absolute as well as fractional composition of modelled and measured aerosols at Payerne is shown in Figure 7.3.12 for various periods in January 2007. The first period is not shown due to too small number of data pairs. The best agreement between measurements and model predictions seems to be in period III. Both measurements and model predictions suggest that the main components are organic aerosols and particulate nitrate.

The statistical parameters calculated for each period are shown in Table 7.3.1. Note that the number of data pairs is very low in period I. The model performance criteria are met for EC all the time during January 2007. Even the model performance goals ($\text{MFB} \leq \pm 30\%$, $\text{MFE} \leq 50\%$) were achieved for EC most of the time. The statistical parameters were close to the criteria in the third and fourth periods for the other aerosol species. The criteria for SO_4 and NH_4 seem to be achieved in the fourth period (26-31 January). The worst model performance was obtained for the second period with low wind.

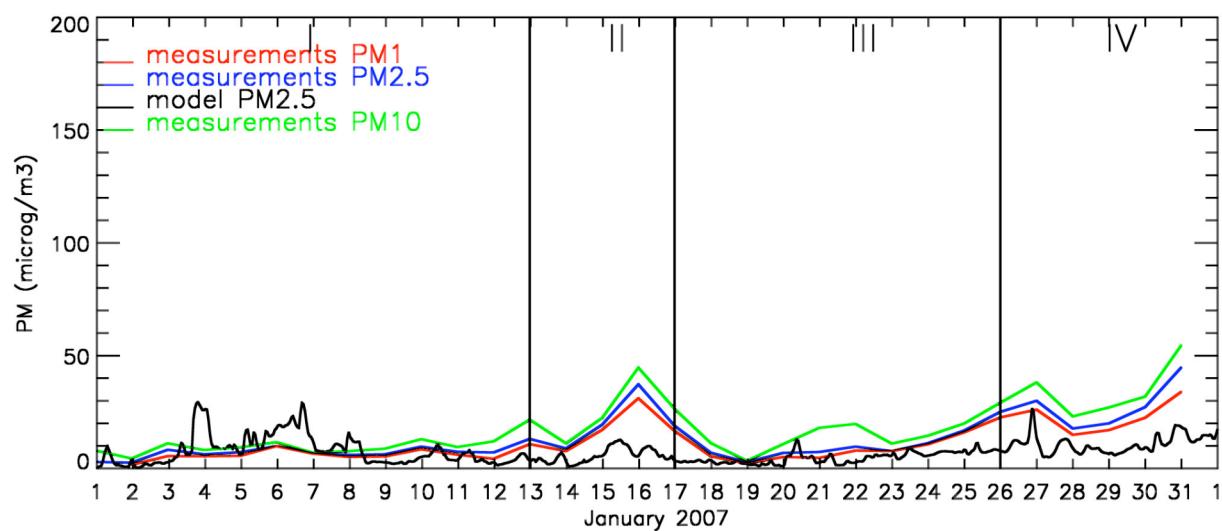


Figure 7.3.1: Comparison of PM1, PM2.5 and PM10 (daily filter measurements at NABEL station), and PM2.5 (model) at Payerne, in January 2007 ($\mu\text{g m}^{-3}$)

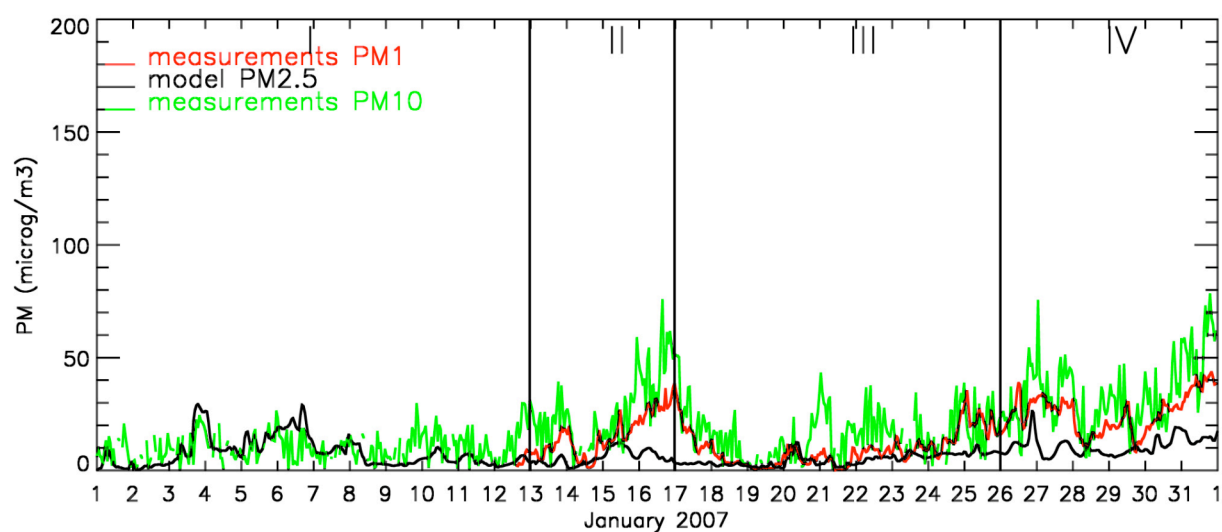


Figure 7.3.2: Comparison of PM1 (AMS measurements), PM2.5 (model) and PM10 (NABEL measurements) at Payerne, in January 2007 ($\mu\text{g m}^{-3}$)

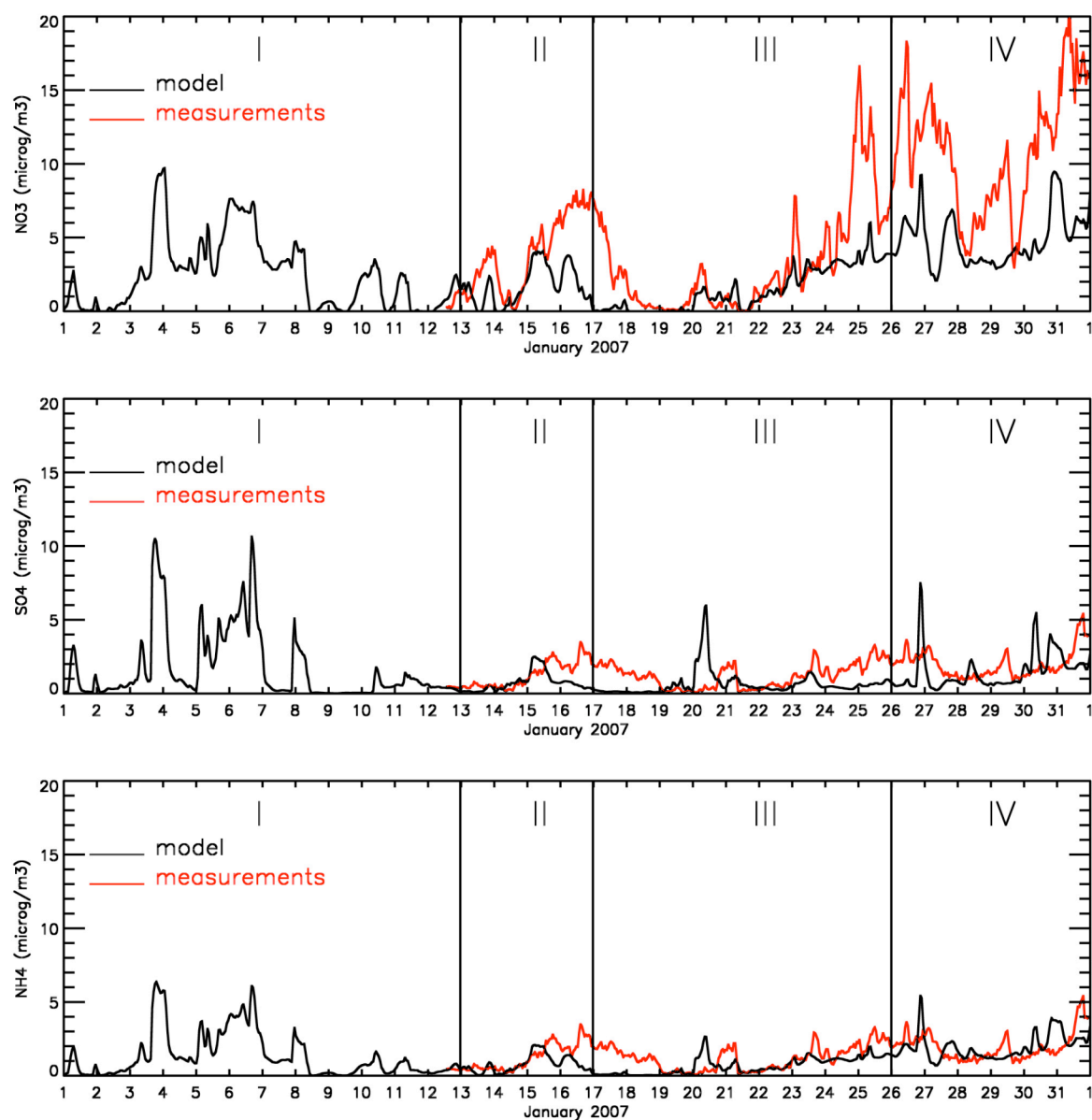


Figure 7.3.3: Comparison of modelled and measured inorganic aerosols ($\mu\text{g m}^{-3}$) at Payerne in January 2007.

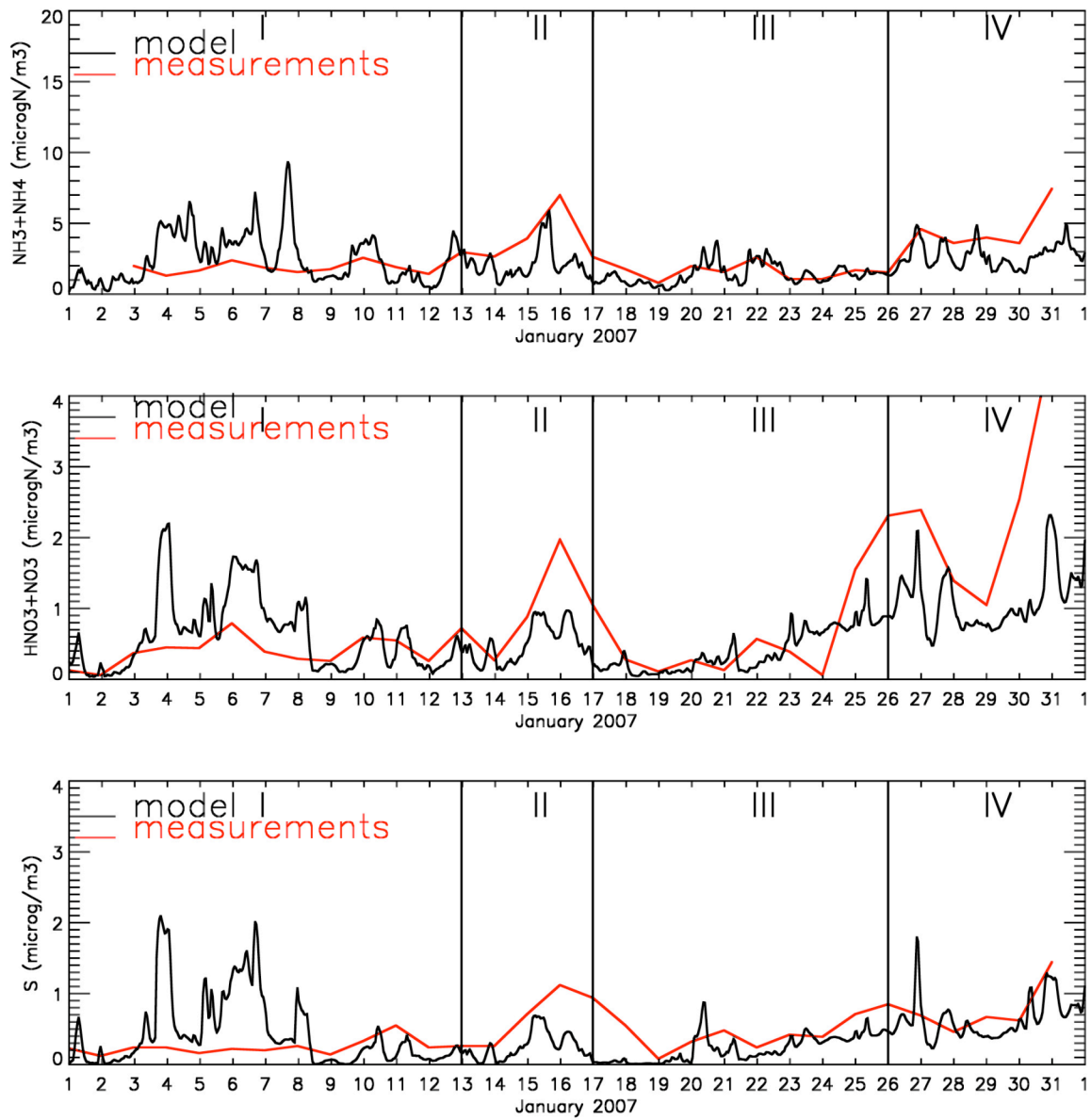


Figure 7.3.4: Comparison of modelled and measured total ammonia (upper panel), total nitrate ($\mu\text{gN m}^{-3}$) (middle panel) and S ($\mu\text{g m}^{-3}$) (lower panel) at Payerne in January 2007.

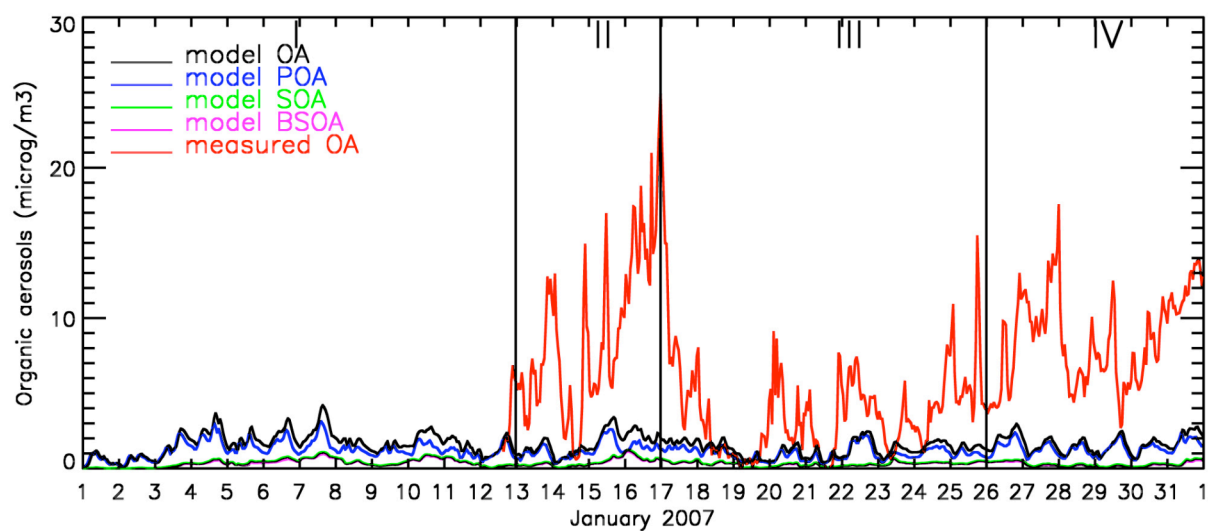


Figure 7.3.5: Comparison of modelled and measured organic aerosols ($\mu\text{g m}^{-3}$) at Payerne in January 2007.

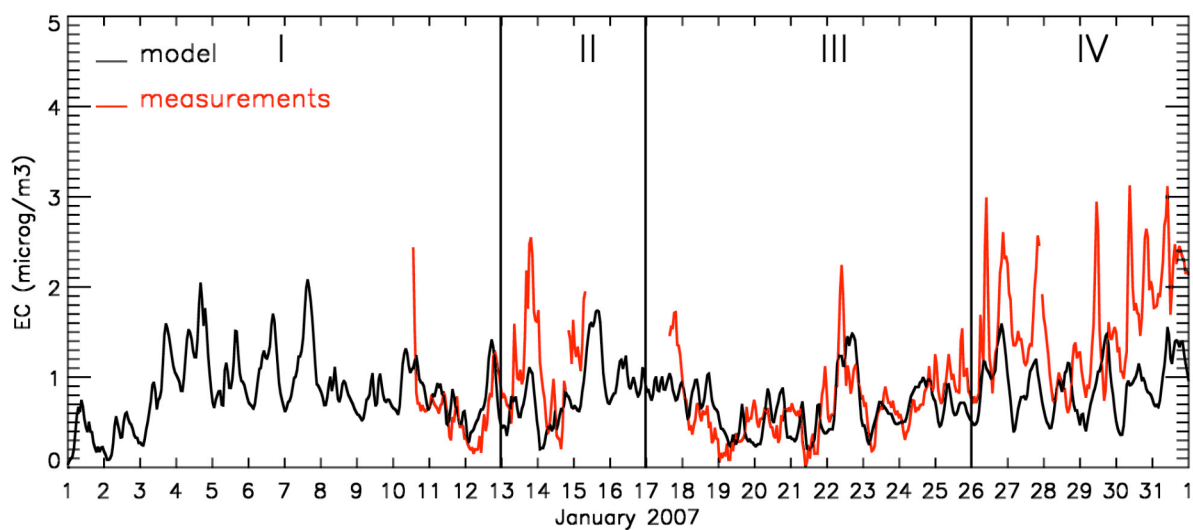


Figure 7.3.6: Comparison of modelled and measured Elemental Carbon, EC ($\mu\text{g m}^{-3}$) at Payerne in January 2007.

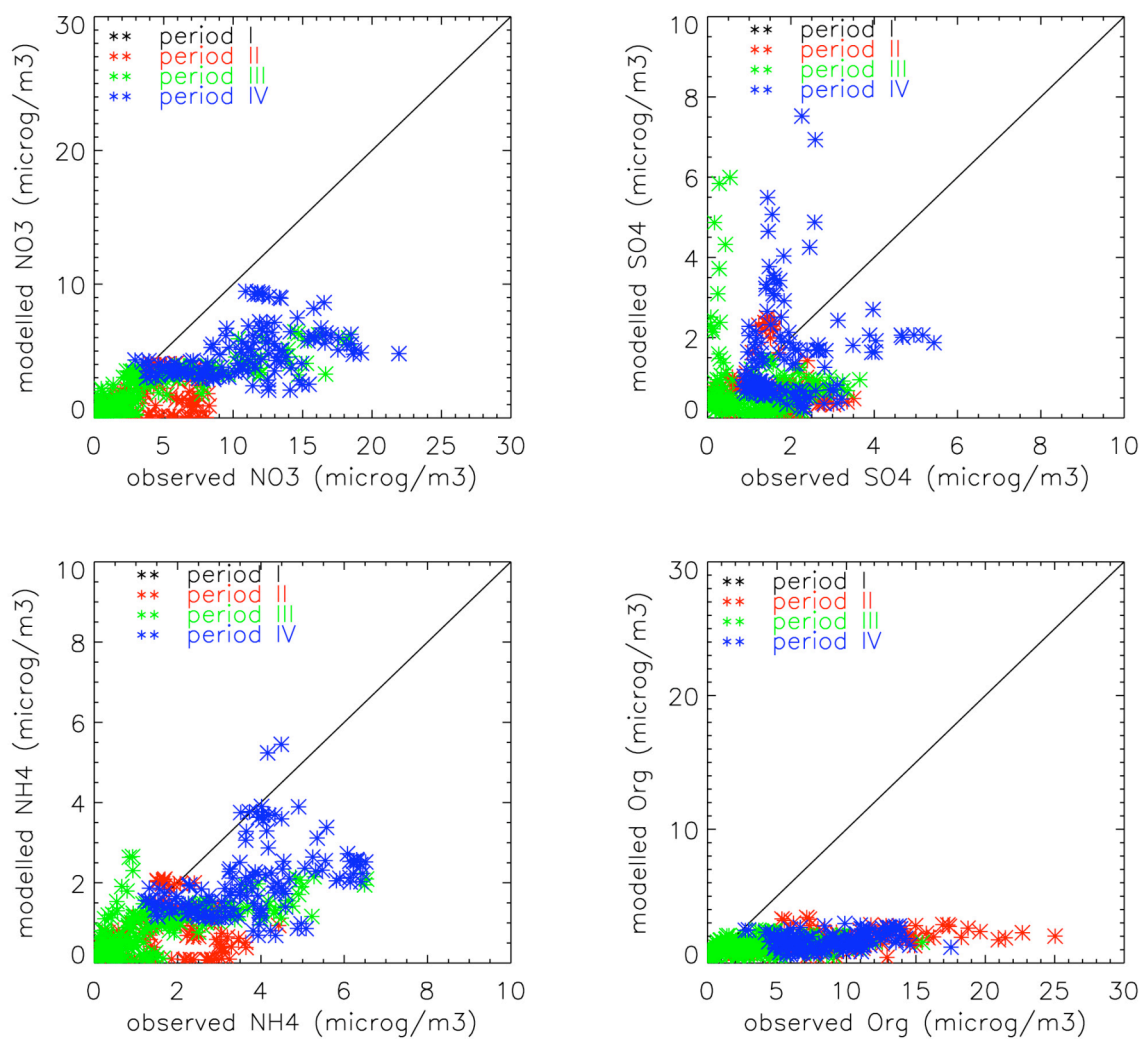


Figure 7.3.7: Modelled versus observed concentrations of inorganic and organic aerosols ($\mu\text{g m}^{-3}$) at Payerne in January 2007.

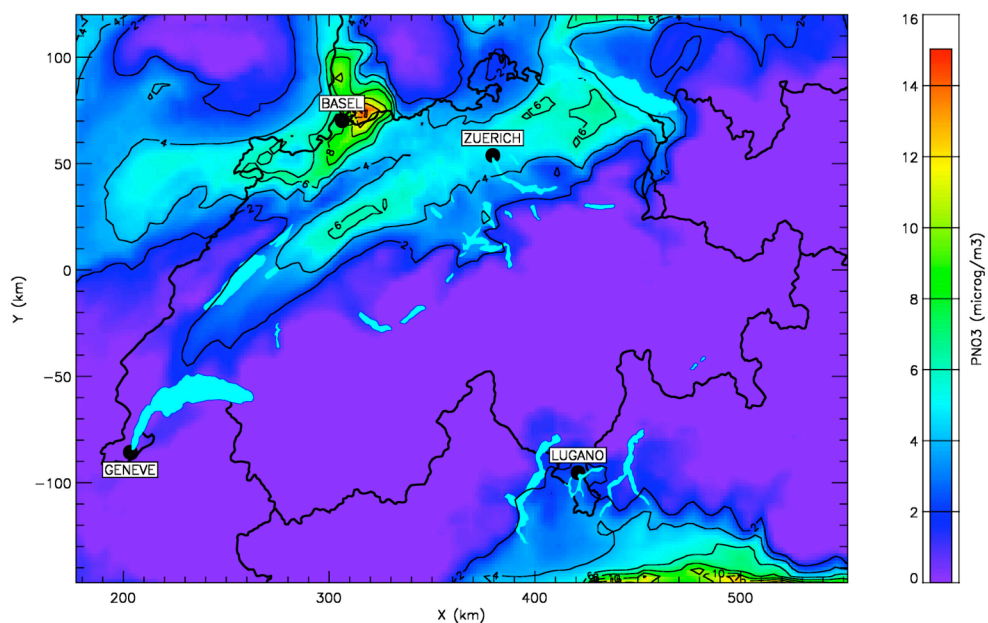


Figure 7.3.8: The highest predicted NO_3 concentrations ($\mu\text{g m}^{-3}$) on 15 January 2007, 03:00 UTC

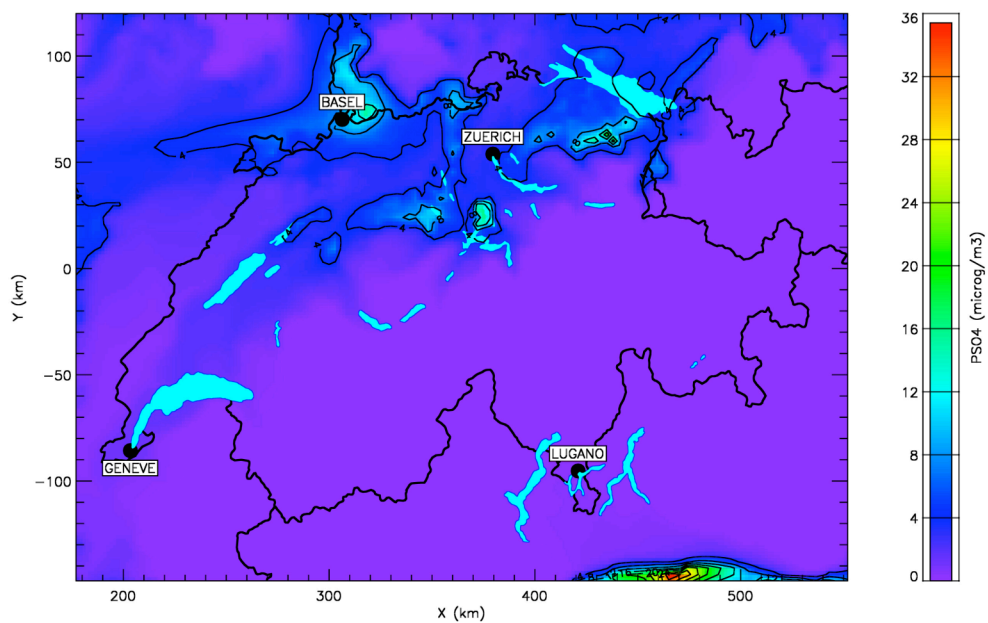


Figure 7.3.9: The highest predicted SO_4 concentrations ($\mu\text{g m}^{-3}$) on 15 January 2007, 09:00 UTC

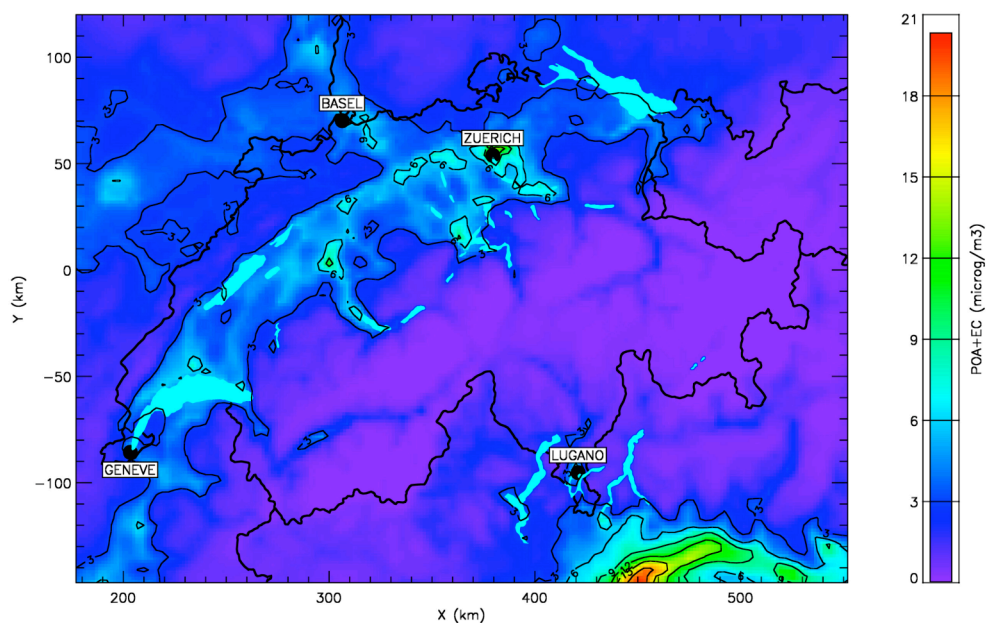


Figure 7.3.10: The highest predicted concentrations of primary aerosols (POA+EC) ($\mu\text{g m}^{-3}$) on 15 January 2007, 16:00 UTC

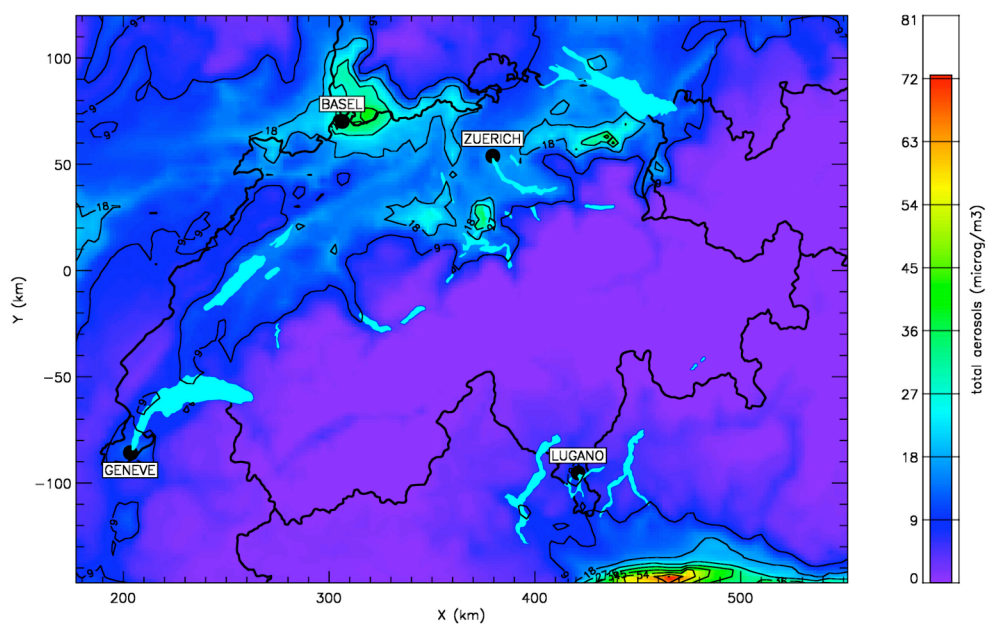


Figure 7.3.11: The highest predicted total aerosol concentrations ($\mu\text{g m}^{-3}$) on 15 January 2007, 09:00 UTC

Table 7.3.1: Statistical parameters for aerosol components for January 2007 at Payerne. The bold numbers indicate that the model performance criteria are met (MFE $\leq +75\%$ and MFB $\leq \pm 60\%$).

species	time	Number of data	observed mean ($\mu\text{g m}^{-3}$)	predicted mean ($\mu\text{g m}^{-3}$)	pred./obs.	RMSE	Correlation Coefficient r	MFB (%)	MFE (%)
NO ₃	2-12 January	11	0.74	2.57	3.47	1.11	-	88	88
	13-16 January	96	3.93	1.71	0.44	3.22	0.367	-69	90
	17-25 January	216	3.16	1.51	0.48	3.10	0.709	-70	95
	26-31 January	143	10.98	4.83	0.44	7.18	0.453	-73	74
	whole January	466	5.66	2.59	0.46	4.74	-	-67	88
SO ₄	2-12 January	11	0.43	1.73	4.04	0.17	-	-50	50
	13-16 January	96	1.27	0.74	0.58	1.12	0.201	-49	80
	17-25 January	216	1.18	0.63	0.54	1.36	-0.175	-55	107
	26-31 January	143	1.97	1.50	0.76	1.58	0.090	-39	69
	whole January	466	1.43	1.22	0.86	1.37	-	-49	89
NH ₄	2-12 January	11	0.28	1.39	4.91	0.37	-	77	80
	13-16 January	96	1.58	0.77	0.49	1.34	0.266	-54	85
	17-25 January	215	1.27	0.67	0.53	1.17	0.483	-41	91
	26-31 January	143	3.75	1.96	0.52	2.22	0.390	-60	63
	whole January	465	2.07	1.21	0.58	1.59	-	-47	81
Organics	2-12 January	11	3.73	1.74	0.47	3.26	-	-54	75
	13-16 January	96	9.08	1.71	0.19	8.97	0.468	-121	125
	17-25 January	213	3.80	1.30	0.34	3.80	0.369	-62	94
	26-31 January	143	8.66	1.67	0.19	7.58	0.254	-131	131
	whole January	463	6.37	1.59	0.25	6.43	-	-95	112
EC	2-12 January	59	0.65	0.76	1.17	0.32	0.609	24	37
	13-16 January	55	1.12	0.83	0.74	0.66	-	-47	59
	17-25 January	201	0.68	0.66	0.98	0.32	-	1.8	43
	26-31 January	143	1.61	0.91	0.57	0.88	-	-53	58
	whole January	458	1.02	0.77	0.76	0.60	-	-18	49

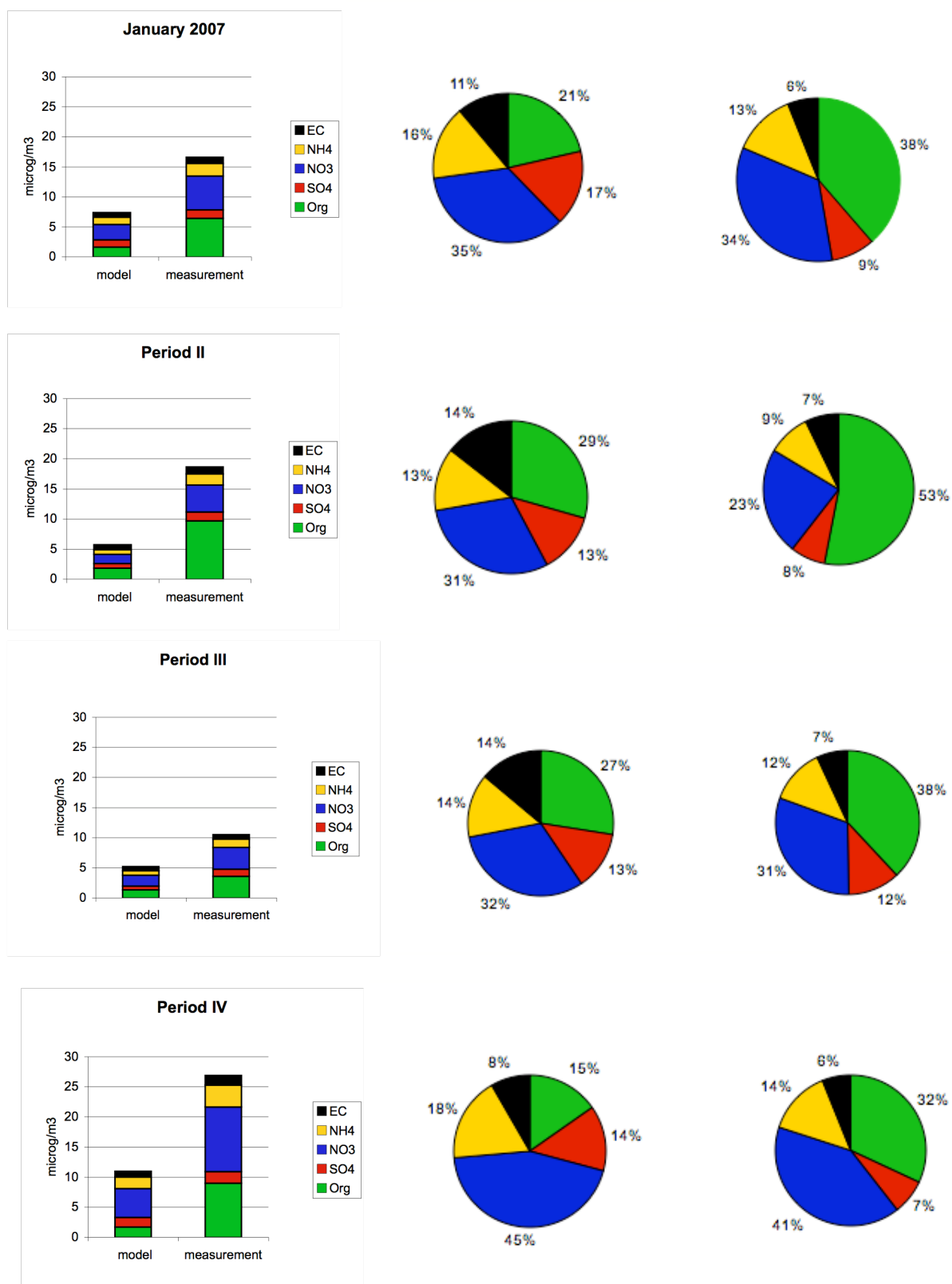


Figure 7.3.12: Comparison of absolute (left) as well as the fractional composition of modelled (middle) and measured (right) aerosols at Payerne. From top to down: whole January 2007, 13-16 January, 17-25 January, 26-31 January.

8 Conclusions

We performed air quality model simulations in Switzerland for three episodes: January-February 2006, June 2006 and January 2007. The availability of detailed measurements of both meteorological parameters as well as gaseous and aerosol concentrations provided us with the opportunity to evaluate and validate our models. The focus in this study was on the particulate matter concentrations, as well as ozone in summer. The Aerosol Mass Spectrometer (AMS) was operated during all three episodes. The other type of measurements used in this study are the air quality monitoring data from the NABEL stations, ANETZ data and the detailed measurements performed at Payerne within the frame of the EMEP monitoring programme. We carried out simulations using the 3-dimensional photochemical model CAMx (Comprehensive Air Quality Model with Extensions). We produced the meteorological input data for each grid cell using the MM5 meteorological model. There were 3 nested model domains covering a large part of Europe, central Europe and Switzerland with horizontal resolutions of $27\text{ km} \times 27\text{ km}$, $9\text{ km} \times 9\text{ km}$ and $3\text{ km} \times 3\text{ km}$, respectively. Both anthropogenic and biogenic emissions in all model domains were prepared using various datasets and procedures for Europe and Switzerland. Initial and boundary conditions were obtained from the global model MOZART that was run for similar periods. Evaluations of both meteorological and air quality model performances were carried out using various selected statistical parameters both in winter and summer.

In general, the model system is able to predict gaseous and particulate matter concentrations reasonably well except during low-wind conditions when the model performance gets worse. The concentrations of pollutants could be reproduced satisfactorily when the wind speed was moderate or strong. Investigation and comparison of vertical profiles with soundings suggest that the boundary layer height and vertical exchange cannot be represented by MM5 satisfactorily under stagnant conditions. MM5 fails to capture the structure of the atmospheric boundary layer and in particular temperature inversions. This in turn implies that vertical transport is not well estimated. The improvement of the meteorological model performance under stagnant conditions is the aim of another project in our group which is still going on.

The model performance for ozone in summer was acceptable at most of the NABEL stations. The peak ozone levels under stagnant conditions could not be captured by the model. The worst model performance was found for the urban sites Bern, Lausanne and Basel and the motorway site Härkingen.

The aerosol concentrations were very high at the end of January, beginning of February 2006. Some trajectory analyses were done to investigate the possibility of the transport of pollutants from abroad. There was no indication of an air mass coming from any polluted areas. Therefore it is unlikely that the elevated levels are associated with the transport of pollutants from abroad. The air quality model results for northern Switzerland suggest that the particulate nitrate and organic aerosols dominate the aerosol composition in winter, as shown also by measurements. The predicted organic aerosols seem to be mainly primary. In summer, the main component of aerosols is the organic aerosol fraction and it is mostly secondary. The model results suggest that secondary organic aerosols are produced mainly from the biogenic precursors such as monoterpenes. The main sources of monoterpene emissions in northern Switzerland are Norway Spruce forests. The model performance for primary aerosols such as elemental carbon looks quite good. The model underestimates the organic aerosol mass concentrations in winter as well as in summer as

other current regional models do. Analysis of AMS data suggested that about half of the particulate organic mass in winter was oxygenated organic aerosols (OOA), mostly representing SOA (Lanz et al., 2008). The fraction of SOA in summer is even larger (80%). It seems that the underestimation of organic aerosols is mainly due to secondary organic aerosols.

Recent measurements suggest that wood-burning emissions might be an important source of organic aerosols in Switzerland. The improvement of wood-burning emissions in our emission inventory is expected to enhance modelling of organic aerosols, especially in winter. Another important source of disagreement between measurements and model results might be the oligomerization of secondary organic aerosols (SOA) as shown by experiments. This mechanism had not yet been treated in the model during the time this study was carried out. However, the latest CAMx version 4.5, which became recently available, contains the improved gas-phase mechanism CB05 as well as the new SOA mechanism allowing oligomerization of aerosols, together with the new pathways to SOA formation such as from isoprene and sesquiterpenes. Another recent finding in SOA formation is the pathway from primary organic-particulate emissions (Robinson et al., 2007) and this new mechanism is planned to be implemented in our model in the near future. The aerosol modelling performance of CAMx is therefore expected to improve in future studies. In addition, a recently initiated PhD project aims to improve the meteorological parameterization and to reduce the disagreement of model results and observations under low-wind conditions. In the near future, using improved meteorological and SOA models, we believe to get much better model performance for air pollutants.

Acknowledgements

This study was financially supported by the Federal Office of Environment (FOEN).

We are grateful to the following people and institutions for providing weather, emission and air quality data:

F. Schubiger and C. Voisard (MeteoSwiss) for COSMO 7 analysis data,
R. Stern (FUB), A. Graff (UBA) and M. van Loon (TNO) for European emissions,
R. Zbinden, M. Keller and J. Heldstab (INFRAS) for Swiss road traffic data,
Th. Kuenzle and B. Rihm (METEOTEST) for updated Swiss NO_x and NH₃ data and for the TRACT emission inventory,
M. Schultz (MPI Hamburg) for MOZART model output data,
Wenche Aas for EMEP data,
IIASA (Z. Klimont) for the web access to the national emission projections 2000-2010 (<http://www.iiasa.ac.at/web-apps/tap/RainsWeb>)

NABEL data was provided by FOEN and Empa, ANETZ data by MeteoSwiss.

We would like also to thank R. Weber (FOEN) for the fruitful co-operation during this project.

Acronyms

AMS	Aerosol Mass Spectrometer
ANETZ	Automatische Wetterbeobachtungsnetz
BAFU	Bundesamt fuer Umwelt
BSOA	Biogenic Secondary Organic Aerosols
CAMx	Comprehensive Air quality Model with eXtensions
CBM-IV	Carbon Bond Mechanism, version 4
CB05	2005 Version of Carbon Bond Mechanism
CBL	Convective Boundary Layer
CBM	Carbon Bond Mechanism
CEST	Central European Summer Time (daylight saving time for Switzerland, 2 h ahead of UTC)
CET	Central European Time (winter time for Switzerland, 1 h ahead of UTC)
COSMO 7	COnsortium for Small scale Modelling, ~ 7 km grid spacing
DIST	Direction Weighted Wind Error
EC	Elemental Carbon
ECMWF	European Centre for Medium-Range Weather Forecasts
EMEP	European Monitoring and Evaluation Programme (Cooperative Programme for Monitoring and Evaluation of the Long-range Transmission of Air Pollutants in Europe)
FDDA	Four-Dimensional Data Assimilation
FOEN	Federal Office for the Environment
FUB	Freie Universitaet Berlin
GDAS	Global Data Assimilation System
HYSPLIT	Hybrid Single-Particle Lagrangian Integrated Trajectory Model
IIASA	International Institute for Applied Systems Analysis
LAC	Laboratory of Atmospheric Chemistry
MBE	Mean Bias Error
MFB	Mean Fractional Bias
MFE	Mean Fractional Error
MGE	Mean Gross Error
MM5	Meso-scale Model 5
MNBE	Mean Normalized Bias Error
MNGE	Mean Normalized Gross Error
MOBS	Mean Observation
MOZART	Model for OZone And Related chemical Tracers
MRF	Medium Range Forecast
NABEL	Nationales Beobachtungsstelle für Luftfremdstoffe

NCEP	National Centers for Environmental Prediction
NMVOC	Non-Methane Volatile Organic Compounds
OOA	Oxygenated Organic Aerosols
PBL	Planetary Boundary Layer
PM _{2.5}	Particulate Matter, $d < 2.5 \mu\text{m}$
PM ₁₀	Particulate Matter, $d < 10 \mu\text{m}$
PMF	Positive Matrix Factorization
POA	Primary Organic Aerosols
PSI	Paul Scherrer Institut
RADM	Regional Acid Deposition Model
RAINS	Regional Air Pollution Information and Simulation
RMSE	Root Mean Square Error
SAPRC	Statewide Air Pollution Research Center
SNAP	Selected Nomenclature for Air Pollution
SOA	Secondary Organic Aerosols
TNO	The Netherlands Organisation for Applied Scientific Research
TOMS	Total Ozone Mapping Spectrometer
UBA	Umweltbundesamt
UTC	Universal Time Coordinated

References

- Andreani-Aksoyoğlu, S., and J. Keller (1995), Estimates of monoterpene and isoprene emissions from the forests in Switzerland, *Journal of Atmospheric Chemistry*, 20, 71-87.
- Andreani-Aksoyoğlu, S., C.-H. Lu, J. Keller, A.S.H. Prévôt, and J. S. Chang (2001), Variability of indicator values for ozone production sensitivity: a model study in Switzerland and San Joaquin Valley (California), *Atmospheric Environment*, 35/32, 5593-5603.
- Andreani-Aksoyoğlu, S., J. Keller, J. Dommen, and A. S. H. Prévôt (2003), Modelling of air quality with CAMx: A case study in Switzerland, *Water, Air & Soil Pollution : FOCUS*, 3, 281-296.
- Andreani-Aksoyoğlu, S., A.S.H. Prévôt, U. Baltensperger, J. Keller, and J. Dommen (2004), Modeling of formation and distribution of secondary aerosols in the Milan area (Italy), *Journal of Geophysical Research*, 109, D05306, doi:10.1029/2003JD004231.
- Andreani-Aksoyoğlu, S., J. Keller, C. Ordóñez, M. Tinguely, M. Schultz, and A. S. H. Prevot (2008a), Influence of various emission scenarios on ozone in Europe, *Ecological Modelling*, 217, 209-218.
- Andreani-Aksoyoğlu, S., J. Keller, A. S. H. Prévôt, U. Baltensperger, and J. Flemming (2008b), Secondary aerosols in Switzerland and northern Italy: Modeling and sensitivity studies for summer 2003, *Journal of Geophysical Research*, 113, D06303, doi:10.1029/2007JD009053.
- Baertsch-Ritter, N., A.S.H.Prévôt, J.Dommen, S.Andreani-Aksoyoğlu, and J.Keller (2003), Model study with UAM-V in the Milan area (I) during PIPAPO: Simulations with changed emissions compared to ground and airborne measurements, *Atmospheric Environment*, 37, 4133-4147.
- Baertsch-Ritter, N., J. Keller, J. Dommen, and A. S. H. Prévôt (2004), Effects of various meteorological conditions and spatial emission resolutions on the ozone concentration and ROG/NOx limitation in the Milan area (I), *Atmos. Chem. Phys.*, 4, 423-438.
- Baltensperger, U., N.Streit, E.Weingartner, S.Nyeki, A.S.H.Prevot, R. V. Dingenen, A.Virkkula, J.-P.Putaud, A.Even, H. t. Brink, A.Blatter, A.Neftel, and H.W.Gäggeler (2002), Urban and rural aerosol characterization of summer smog events during the PIPAPO field campaign in Milan, Italy, *J. Geophys. Res.*, 107(D22), 8193, doi:10.1029/2001JD001292.
- Bessagnet, B., A. Hodzic, R. Vautard, M. Beekmann, S. Cheinet, C. Honore, C. Liousse, and L. Rouil (2004), Aerosol modeling with CHIMERE--preliminary evaluation at the continental scale, *Atmospheric Environment*, 38, 2803-2817.
- BFS (1999), *GEOSTAT Benutzerhandbuch*, Bern.
- Boylan, J. W., and A. G. Russell (2006), PM and light extinction model performance metrics, goals, and criteria for three-dimensional air quality models, *Atmospheric Environment*, 40, 4946-4959.
- Builtjes, P., M. van Loon, M. Schaap, S. Teeuwisse, A. J. H. Visschedijk, and J. P. Bloos (2002), The development of an emission data base over Europe and further contributions

- of TNO-MEP, 70 pp, Freie Universitaet Berlin / Institut fuer Meteorologie und Troposphaerischer Umweltforschung, Berlin.
- BUWAL (1995), Vom Menschen verursachte Luftschadstoffemissionen in der Schweiz von 1900 bis 2010, BUWAL, Bern.
- Carter, W. P. L. (2000), Programs and files implementing the SAPRC-99 mechanism and its associates emissions processing procedures for Models-3 and other regional models, <http://pah.cert.ucr.edu/~carter/SAPRC99/s99files.htm>.
- Chang, J. S., R.A. Brost, I.S.A. Isaksen, S. Madronich, P. Middleton, W.R. Stockwell, and C. J. Walcek (1987), A three-dimensional eulerian acid deposition model : Physical concepts and formulation, *Journal of Geophysical Research*, 92, 14,681-614,700.
- COSMO (2002), Newsletter No. 2, Deutscher Wetterdienst, Offenbach (D).
- Cousin, F., C. Liousse, H. Cachier, B. Bessagnet, B. Guillaume, and R. Rosset (2005), Aerosol modelling and validation during ESCOMPTE 2001, *Atmospheric Environment*, 39, 1539-1550.
- Cox, R., B. L. Bauer, and T. Smith (1998), A Mesoscale Model Intercomparison, *Bulletin of the American Meteorological Society*, 79, 265-283.
- Draxler, R. R., and G. D. Rolph (2008), HYSPLIT - Hybrid Single Particle Lagrangian Integrated Trajectory Model, edited by A. R. L. (ARL).
- Environ (2006), User's Guide, Comprehensive Air Quality Model with Extensions (CAMx), Version 4.4, Environ International Corporation, California.
- EPA (2005), CMAQ model performance evaluation for 2001: Update March 2005, 140 pp, EPA, Research Triangle Park.
- Gehrig, R., and B. Buchmann (2003), Characterising seasonal variations and spatial distribution of ambient PM₁₀ and PM_{2.5} concentrations based on long-term Swiss monitoring data, *Atmospheric Environment*, 37, 2571-2580.
- Gery, M. W., G. Z. Whitten, J.P. Killus, and M. C. Dodge (1989), A photochemical kinetics mechanism for urban and regional scale computer modeling, *Journal of Geophysical Research*, 94, 925-956.
- Held, T., Q. Ying, A. Kaduwela, and M. Kleeman (2004), Modeling particulate matter in the San Joaquin Valley with a source-oriented externally mixed three-dimensional photochemical grid model, *Atmospheric Environment*, 38, 3689-3711.
- Heldstab, J., P. de Haan van der Weg, T. Kuenzle, M. Keller, and R. Zbinden (2003), Modelling of PM₁₀ and PM_{2.5} ambient concentrations in Switzerland 2000 and 2010, Bundesamt fuer Umwelt, Wald und Landschaft (BUWAL), Bern.
- Heldstab, J., and P. Wuethrich (2006), Emissionsmuster. Raeumliche Verteilung und Ganglinien fuer CO- /NMVOC-Emissionen, 15 pp, BAFU, Bern / Zürich.
- Horowitz, L. W., S. Walters, D. L. Mauzerall, L. K. Emmons, P. J. Rasch, C. Granier, X. Tie, J.-F. Lamarque, M. G. Schultz, G. S. Tyndall, J. J. Orlando, and G. P. Brasseur (2003), A global simulation of tropospheric ozone and related tracers: Description and evaluation of MOZART, version 2. , *J. Geophys. Res.*, 108, 4784, doi:4710.1029/2002JD002853.

- Hueglin, C., R. Gehrig, U. Baltensperger, M. Gysel, C. Monn, and H. Vonmont (2005), Chemical characterisation of PM_{2.5}, PM₁₀ and coarse particles at urban, near-city and rural sites in Switzerland, *Atmospheric Environment*, 39, 637-651.
- IPCC (2007), Working Group 1 Report: The Physical Basis of Climate Change (Intergovernmental Panel on Climate Change, 2007) <http://ipcc-wg1.ucar.edu/wg1-report.html>.
- Janjić, Z. I. (1994), The Step-Mountain Eta Coordinate Model: Further Developments of the Convection, Viscous Sublayer, and Turbulence Closure Schemes, *Monthly Weather Review*, 122, 927-945.
- Kalberer, M., D. Paulsen, M. Sax, M. Steinbacher, J. Dommen, A. S. H. Prévôt, R. Fisseha, E. Weingartner, V. Frankevic, R. Zenobi, and U. Baltensperger (2004), Identification of polymers as major components of atmospheric organic aerosols, *Science*, 303, 1659-1662.
- Keller, J., S. Andreani-Aksoyoğlu, and U. Joss (1995), Inventory of natural emissions in Switzerland, paper presented at Air Pollution III, Computational Mechanics Publications, Porto Carras, Greece.
- Keller, J., S. Andreani-Aksoyoğlu, M. Tinguely, J. Flemming, J. Heldstab, M. Keller, R. Zbinden, and A. S. H. Prevot (2008), The impact of reducing the maximum speed limit on motorways in Switzerland to 80 km h⁻¹ on emissions and peak ozone, *Environ. Model. Softw.*, 23, doi:10.1016/j.envsoft.2007.04.008, 322-332.
- Keller, M., and P. de Haan (2004), Handbuch Emissionsfaktoren des Strassenverkehrs 2.1. Dokumentation, 127 pp, INFRAS / UBA Berlin / UBA Wien / BUWAL, Bern.
- Kropf, R. (2001), Massnahmen zur Reduktion der PM₁₀-Emissionen, 112 pp, Bundesamt fuer Umwelt (BAFU), Bern.
- Kuebler, J., A.G.Russell, A.Hakami, A.Clappier, and H. v. d. Bergh (2002), Episode selection for ozone modelling and control strategies analysis on the Swiss Plateau, *Atmospheric Environment*, 36, 2817-2830.
- Kumar, N., F. W. Lurmann, A. S. Wexler, S. N. Pandis, and J. H. Seinfeld (1996), Development and application of a three dimensional aerosol model, paper presented at A&WMA Specialty Conference on Computing in Environmental Resource Management, Research Triangle Park, NC (USA).
- Lanz, V. A., M. R. Alfarra, U. Baltensperger, B. Buchmann, C. Hueglin, and A. S. H. Prevot (2007), Source apportionment of submicron organic aerosols at an urban site by linear unmixing of aerosol mass spectra, *Atmos. Chem. Phys.*, 7, 1503-1522.
- Lanz, V. A., M. R. Alfarra, U. Baltensperger, B. Buchmann, C. Hueglin, S. Szidat, M. N. Wehrli, L. Wacker, S. Weimer, A. Caseiro, H. Puxbaum, and A. S. H. Prevot (2008), Source Attribution of Submicron Organic Aerosols during Wintertime Inversions by Advanced Factor Analysis of Aerosol Mass Spectra, *Environ. Sci. Technol.*, 42, 214-220.
- Liu, L., F. Flatøy, C. Ordoñez, G.O. Braathen, C. Hak, W. Junkermann, S. Andreani-Aksoyoğlu, J. Mellqvist, B. Galle, A.S.H. Prévôt, and I. S. A. Isaksen (2007a), Photochemical modelling in the Po basin with focus on formaldehyde and ozone, *Atmospheric Chemistry and Physics*, 7, 121-137.
- Liu, L., S. Andreani-Aksoyoğlu, J. Keller, G. O. Braathen, M. Schultz, A. S. H. Prévôt, and I. S. A. Isaksen (2007b), A photochemical modelling study of ozone and formaldehyde

- generation and budget in the Po basin, *J. Geophys. Res.*, **112**, doi:10.1029/2006JD008172.
- Madronich, S. (2002), The Tropospheric Visible Ultra-violet (TUV) model web page. , *National Center for Atmospheric Research, Boulder, CO.* , <http://www.acd.ucar.edu/TUV/>.
- Mahrer, F., and C. Vollenweider (1983), *Landesforstinventar LFI*, Eidgenössische Forschungsanstalt für Wald, Schnee und Landschaft (WSL), Birmensdorf.
- Martilli, A., A.Neftel, G.Favaro, S.Sillman, and A.Clappier (2002), Simulation of the ozone formation in the northern part of the Po Valley, *J. Geophys. Res.*, **107**(D22), 8195, doi:10.1029/2001JD000534.
- Morris, R. E., B. Koo, A. Guenther, G. Yarwood, D. McNally, T. W. Tesche, G. Tonnesen, J. Boylan, and P. Brewer (2006), Model sensitivity evaluation for organic carbon using two multi-pollutant air quality models that simulate regional haze in the southeastern United States, *Atmospheric Environment*, **40**, 4960-4972.
- NASA/GSFC (2005), Total ozone mapping spectrometer, <http://toms.gsfc.nasa.gov/ozone/ozone.html>.
- NCEP (2004), SSI Analysis System 2004. NOAA/NCEP/Environmental Modeling Center Office Note 443, 11 pp, Washington.
- Neftel, A., C.Spirig, A.S.H.Prevot, M.Furger, J.Stutz, B.Vogel, and J.Hjorth (2002), Sensitivity of photooxidant production in the Milan Basin: An overview of results from a EUROTRAC-2 Limitation of Oxidant Production field experiment, *J. Geophys. Res.*, **107**(D22), 8188, doi:10.1029/2001JD001263.
- Nenes, A., S. N. Pandis, and C. Pilinis (1998), ISORROPIA: A new thermodynamic equilibrium model for multiphase multicomponent inorganic aerosols, *Aquatic Geochemistry*, **4**, 123-152.
- Ordóñez, C., A. Richter, M. Steinbacher, C. Zellweger, H. Nuss, J. P. Burrows, and A. S. H. Prevot (2006), Comparison of 7 years of satellite-borne and ground-based tropospheric NO₂ measurements around Milan, Italy, *Journal of Geophysical Research*, **111**, D05310, doi:10.1029/2005JD006305.
- Passant, N. R. (2002), Speciation of UK emissions of non-methane volatile organic compounds, 289 pp, AEA Technology, Culham.
- PSU/NCAR (2004), MM5 Version 3 Tutorial Presentations.
- Putaud, J.-P., R. V. Dingenen, and F. Raes (2002), Submicron aerosol mass balance at urban and semirural sites in the Milan area (Italy), *J. Geophys. Res.*, **107**(D22), 8198, doi:10.1029/2000JD000111.
- Robinson, A. L., N. M. Donahue, M. K. Shrivastava, E. A. Weitkamp, A. M. Sage, A. P. Grieshop, T. E. Iane, J. R. Pierce, and S. N. Pandis (2007), Rethinking Organic Aerosols: Semivolatile emissions and photochemical aging *Science*, **315**, 1259-1262.
- Russell, L. M., S.N.Pandis, and J.H.Seinfeld (1994), Aerosol production and growth in the marine boundary layer, *Journal of Geophysical Research* **99**, 20989-21003.
- Schlünzen, H. (editor) (2008), Guideline for Mesoscale Model Evaluation, Report of COST728-WG4. University of Hamburg / COST 728, Hamburg.
- Schneider, A. (2007), Branchenspezifische VOC-Profil, BAFU, Bern / Basel.

- Seibert, P., F. Beyrich, S.-E. Gryning, S. Joffre, A. Rasmussen, and P. Tercier (2000), Review and intercomparison of operational methods for the determination of the mixing height, *Atmospheric Environment*, **34**, 1001-1027.
- Seinfeld, J. H., and S. N. Pandis (1998), *Atmospheric chemistry and physics*, Wiley, New York.
- Simpson, D., W. Winiwarter, G. Börjesson, S. Cinderby, A. Ferreiro, A. Guenther, N. C. Hewitt, R. Janson, M. A. K. Khalil, S. Owen, T. E. Pierce, H. Puxbaum, M. Shearer, U. Skiba, R. Steinbrecher, L. Tarrasón, and M. G. Öquist (1999), Inventorying emissions from nature in Europe, *Journal of Geophysical Research*, **104**, 8113-8152.
- Steinbacher, M., J. Dommen, C. Ordonez, S. Reimann, J. Staehelin, S. Andreani-Aksoyoğlu, and A. S. H. Prevot (2005), Volatile organic compounds in the Po basin. Part B: biogenic VOCs, *J. Atmos. Chem.*, **51**, 293-315.
- Stern, R. (2003), Erstellung einer europaweiten Emissionsdatenbasis mit Bezugsjahr 1995 und die Erarbeitung von Emissionsszenarien für die grossräumige Ausbreitungsrechnungen mit REM/CALGRID, 84 pp, Freie Universität Berlin / Institut fuer Meteorologie und Troposphärischer Umweltforschung, Berlin.
- Strader, R., C. Gurciullo, S.N. Pandis, N. Kumar, and F. W. Lurmann (1998), Development of gas-phase chemistry, secondary organic aerosol, and aqueous-phase chemistry modules for PM modeling, Sonoma Technology, Inc., Petaluma, CA, STI-97510-1822-FR.
- Thunis, P. (2002), CITY - DELTA European Modelling Exercise. An Inter-comparison of long-term model responses to urban-scale emission-reduction scenarios edited, Ispra (I).
- USEPA (1991), Guideline for regulatory application of the Urban Airshed Model, *USEPA Report No. EPA-450/4-91-013*.
- Vecchi, R., G. Marazzan, and G. Valli (2007), A study on nighttime-daytime PM₁₀ concentration and elemental composition in relation to atmospheric dispersion in the urban area of Milan (Italy), *Atmospheric Environment*, **41**, 2136-2144.
- Volkamer, R., J. L. Jimenez, F. S. Martini, K. Dzepina, Q. Zhang, D. Salcedo, L. T. Molina, D. R. Worsnop, and M. J. Molina (2006), Secondary organic aerosol formation from anthropogenic air pollution: Rapid and higher than expected, *Geophysical Research Letters*, **33**, doi:10.1029/2006GL026899.
- Wanner, H., E. Salvisberg, R. Rickli, and M. Schüepp (1998), 50 years of Alpine Weather Statistics (AWS), *Meteorologische Zeitschrift, N.F.*, **7**, 99-111.
- Weber, R. O., and A. S. H. Prevot (2002), Climatology of ozone transport from the free troposphere into the boundary layer south of the Alps during North Foehn, *Journal of Geophysical Research*, **107**, 4030, doi:10.1029/2001JD000987.
- Wesely, M. L. (1989), Parameterization of surface resistances to gaseous dry deposition in regional-scale numerical models, *Atmospheric Environment*, **23**, 1293-1304.
- Wetterzentrale (2008), Wetterzentrale, edited.
- Yin, D., W. Jiang, H. Roth, and E. Giroux (2004), Improvement of biogenic emissions estimation in the Canadian Lower Fraser Valley and its impact on particulate matter modeling results, *Atmospheric Environment*, **38**, 507-521.
- Zaengl, G. (2002), Stratified flow over a mountain with a gap. Linear theory and numerical simulations, *Quarterly Journal of the Royal Meteorological Society*, **128**, 927-949.

Zhang, Y., B. Pun, K. Vijayaraghavan, S.-Y. Wu, C. Seigneur, S. N. Pandis, M.Z. Jacobson, A. Nenes, J. H. Seinfeld, and F.S. Binkowski (2004), Development and application of the model of aerosol dynamics, reaction, ionization and dissolution (MADRID), *Journal of Geophysical Research*, 109, D01202, doi:10.1029/2003JD003501.

Appendix

**Time Series of
Wind Velocity, Wind Direction, Air Temperature,
Specific Humidity, Global Irradiance, Planetary Boundary Layer Height,
and Precipitation Rate
in January 2006, June 2006 and January 2007**

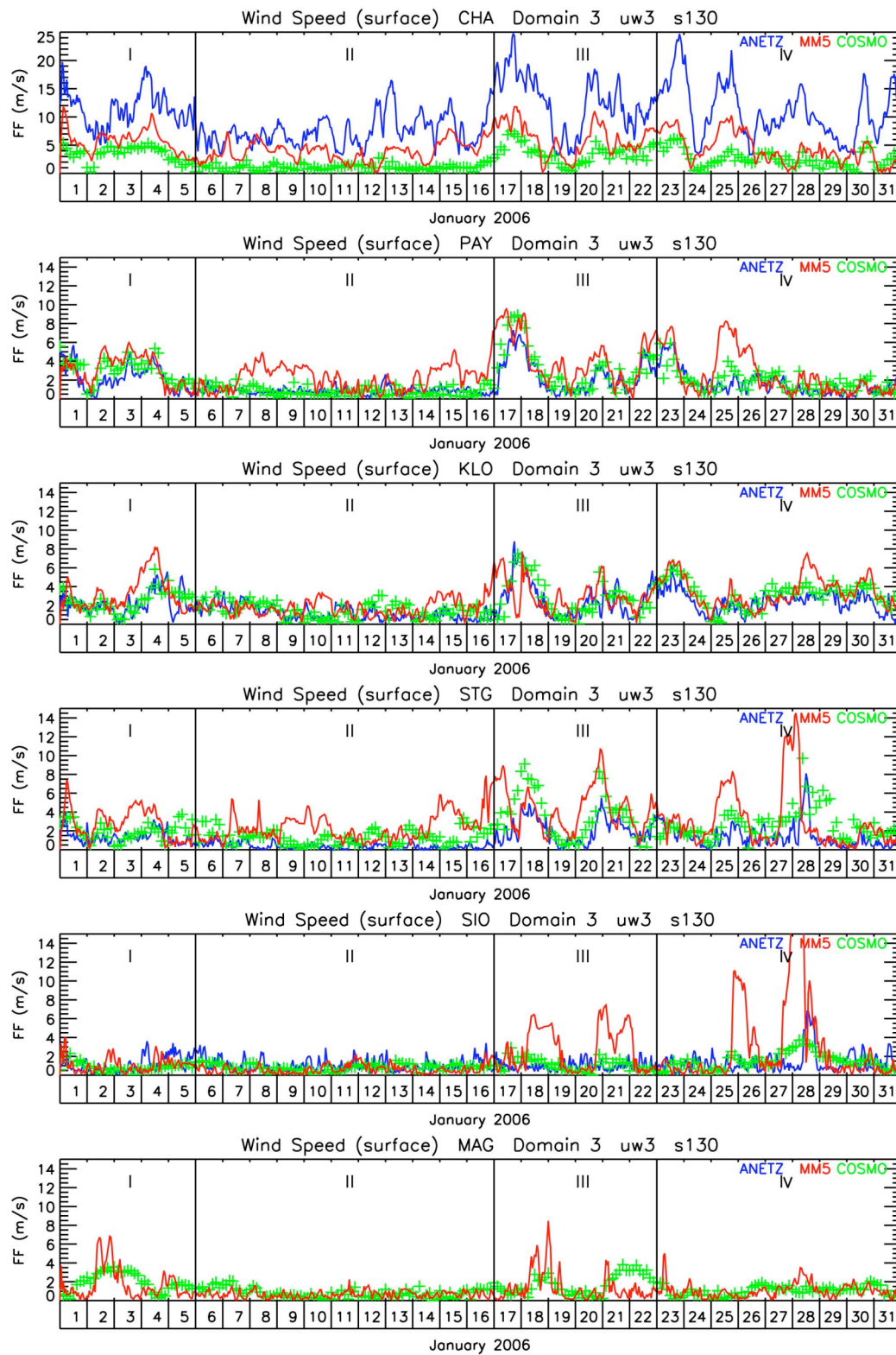


Figure A1: Surface measurements and simulations of wind velocity at the ANETZ sites Chasseral (CHA), Payerne (PAY), Zurich Airport (KLO), St. Gallen (STG), Sion (SIO) and Magadino (MAG) in January 2006. Blue: ANETZ, red: MM5, green: COSMO 7 (3h)

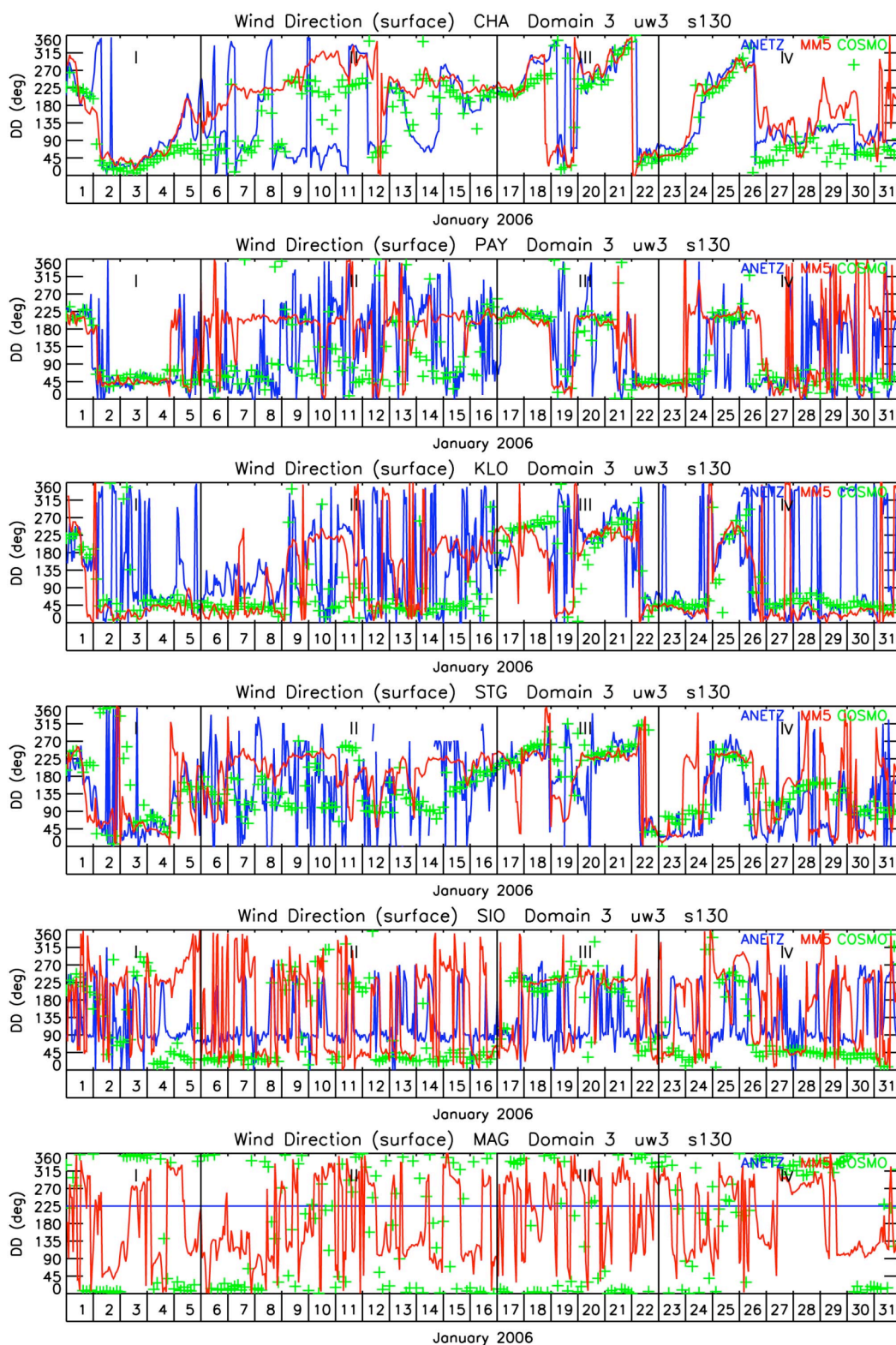


Figure A2: Surface measurements and simulations of wind direction at the ANETZ sites Chasseral (CHA), Payerne (PAY), Zurich Airport (KLO), St. Gallen (STG), Sion (SIO) and Magadino (MAG) in January 2006. Blue: ANETZ, red: MM5, green: COSMO 7 (3h)

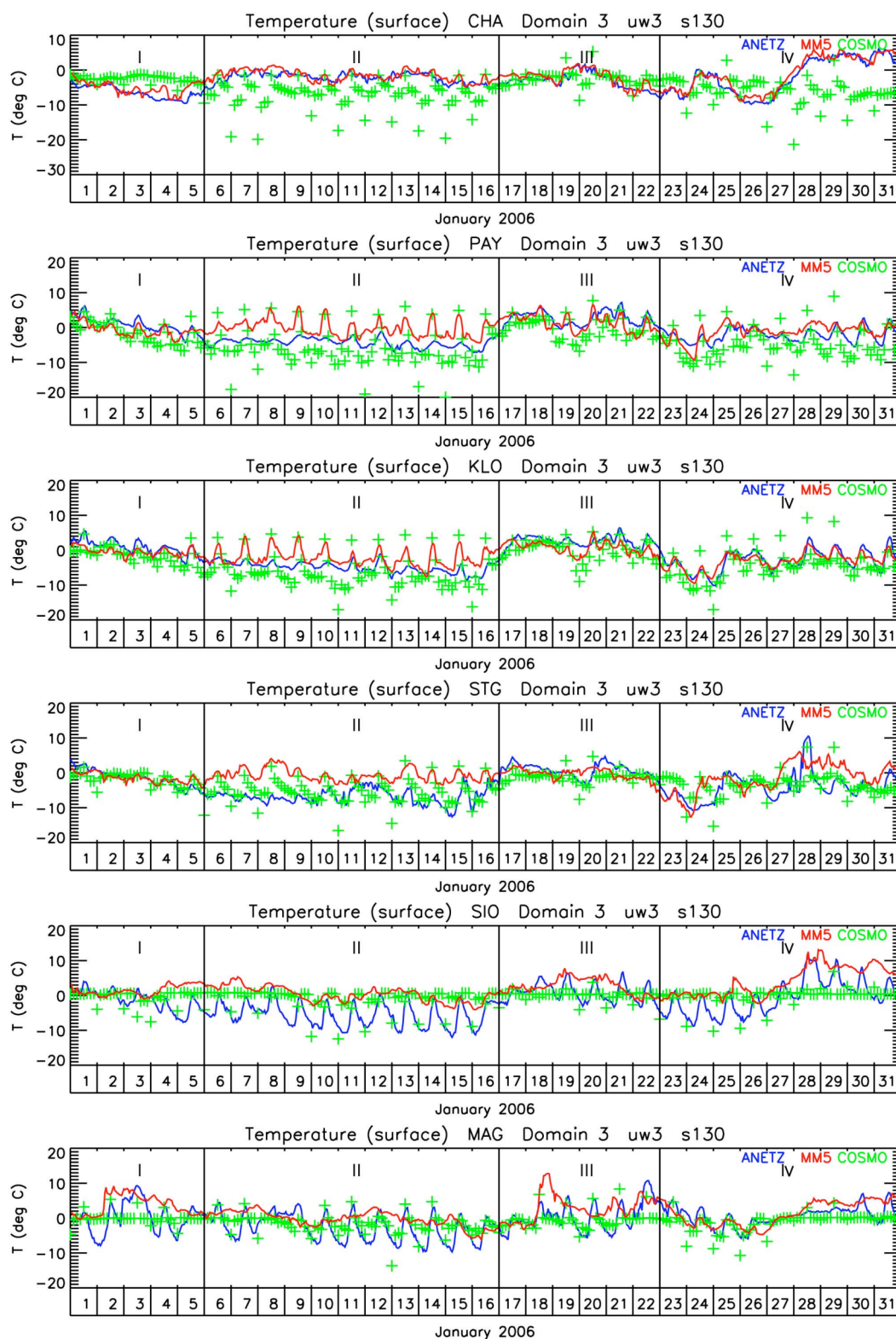


Figure A3: Surface measurements and simulations of air temperature at the ANETZ sites Chasseral (CHA), Payerne (PAY), Zurich Airport (KLO), St. Gallen (STG), Sion (SIO) and Magadino (MAG) in January 2006. Blue: ANETZ, red: MM5, green: COSMO 7 (3h)

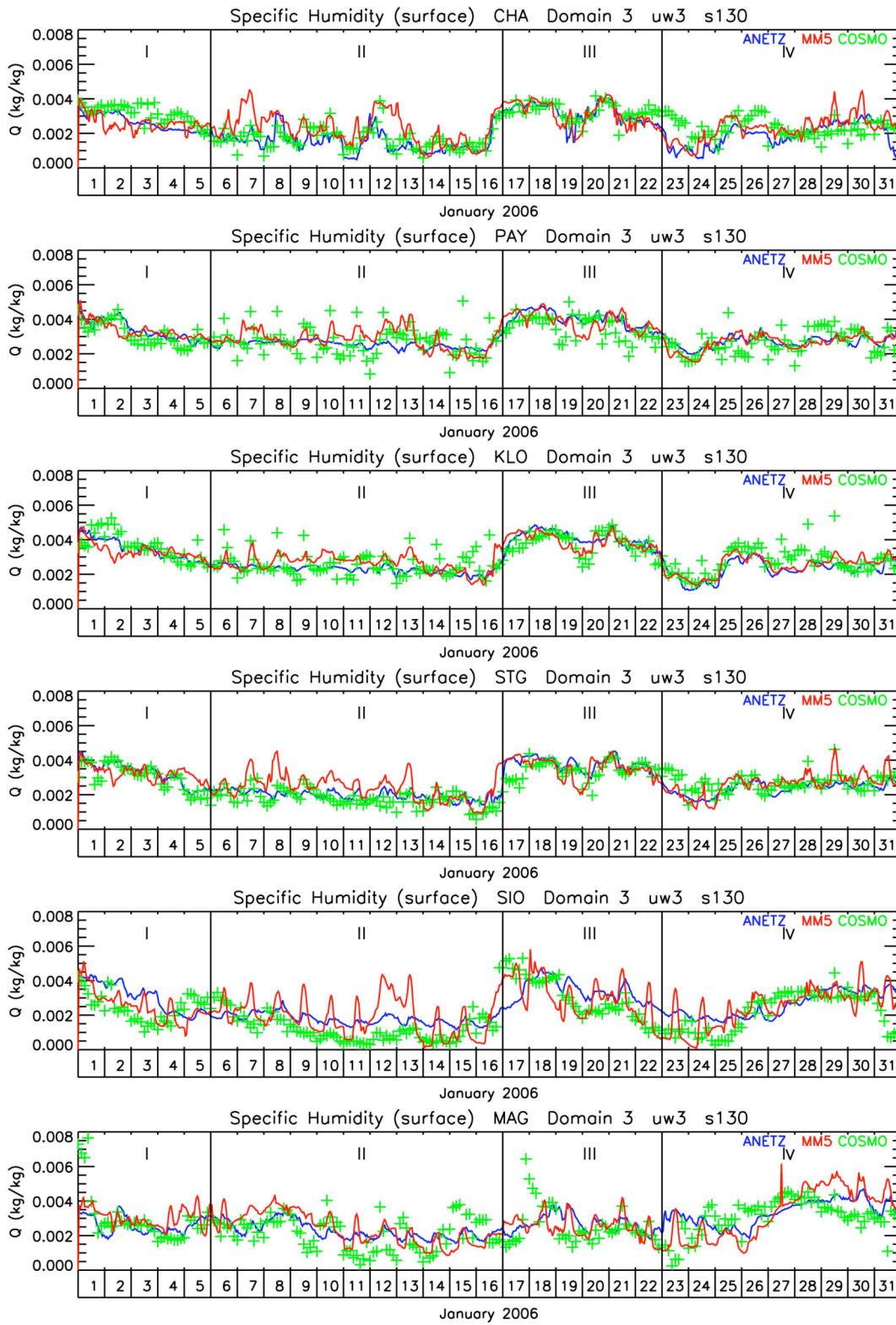


Figure A4: Surface measurements and simulations of specific humidity at the ANETZ sites Chasseral (CHA), Payerne (PAY), Zurich Airport (KLO), St. Gallen (STG), Sion (SIO) and Magadino (MAG) in January 2006. Blue: ANETZ, red: MM5, green: COSMO 7 (3h)

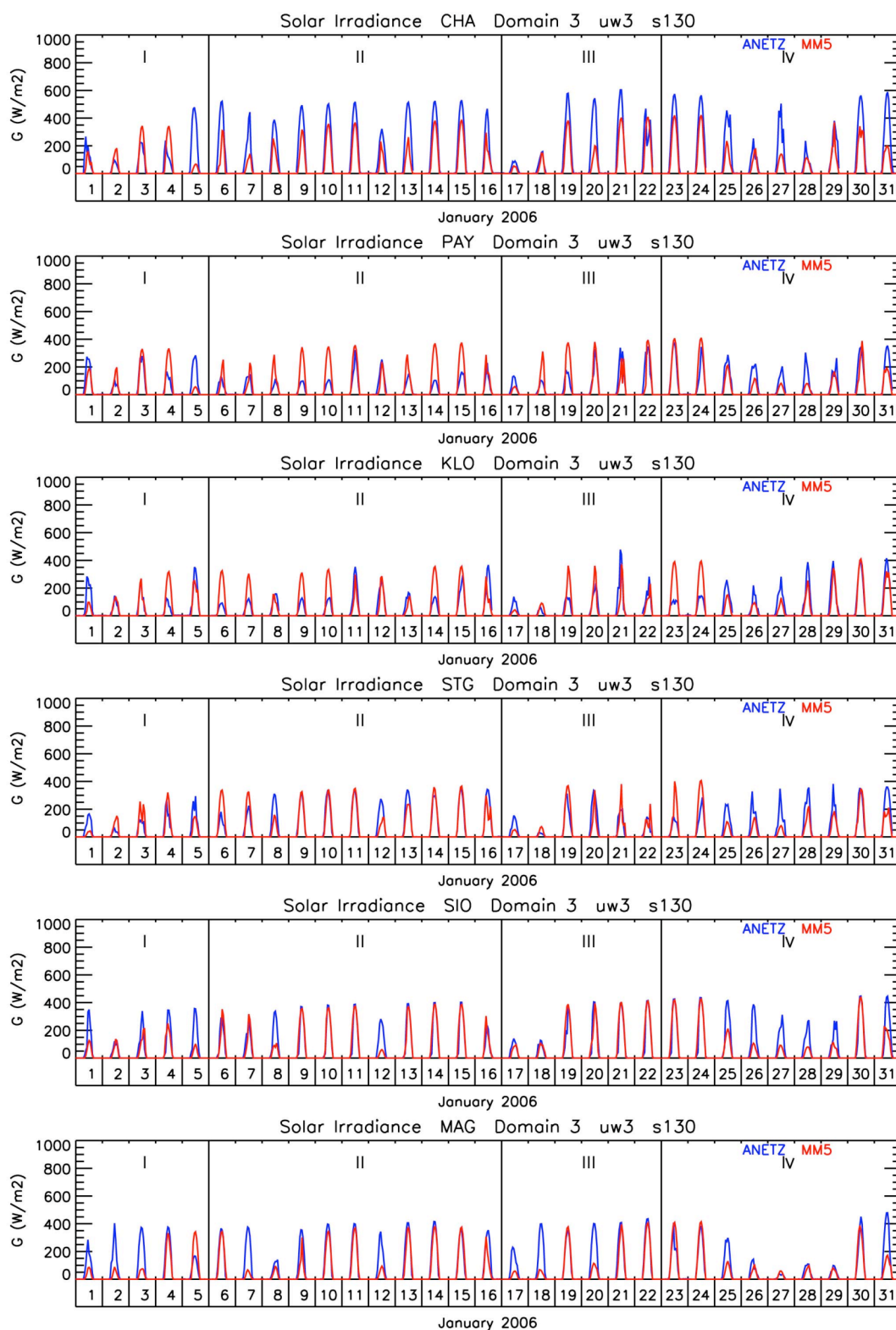


Figure A5: Surface measurements and simulations of global irradiance at the ANETZ sites Chasseral (CHA), Payerne (PAY), Zurich Airport (KLO), St. Gallen (STG), Sion (SIO) and Magadino (MAG) in January 2006. Blue: ANETZ, red: MM5.

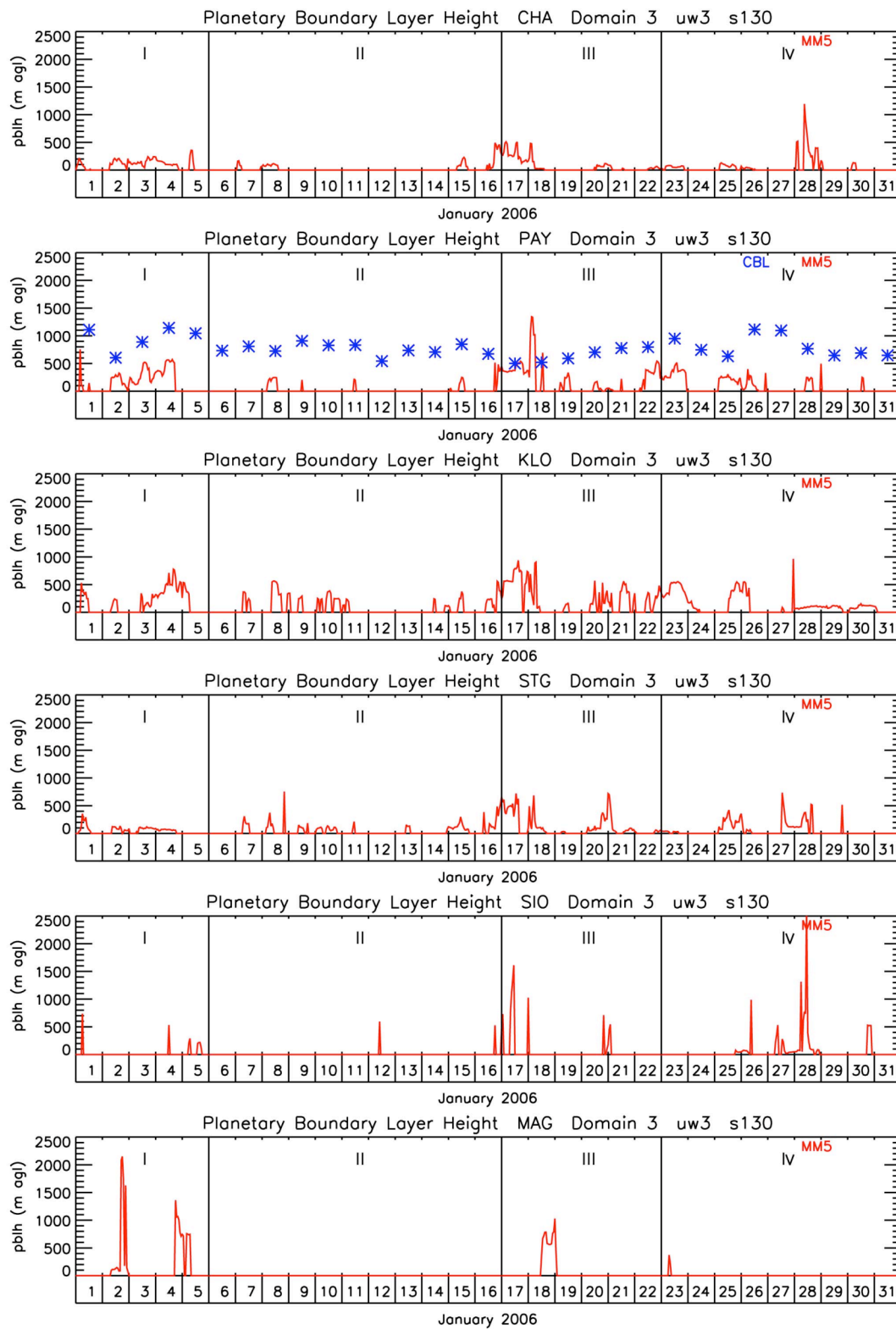


Figure A6: Simulations of planetary boundary layer height at the ANETZ sites Chasseral (CHA), Payerne (PAY), Zurich Airport (KLO), St. Gallen (STG), Sion (SIO) and Magadino (MAG) in January 2006. Blue: convective boundary layer (CBL) height derived from Payerne soundings, red: MM5.

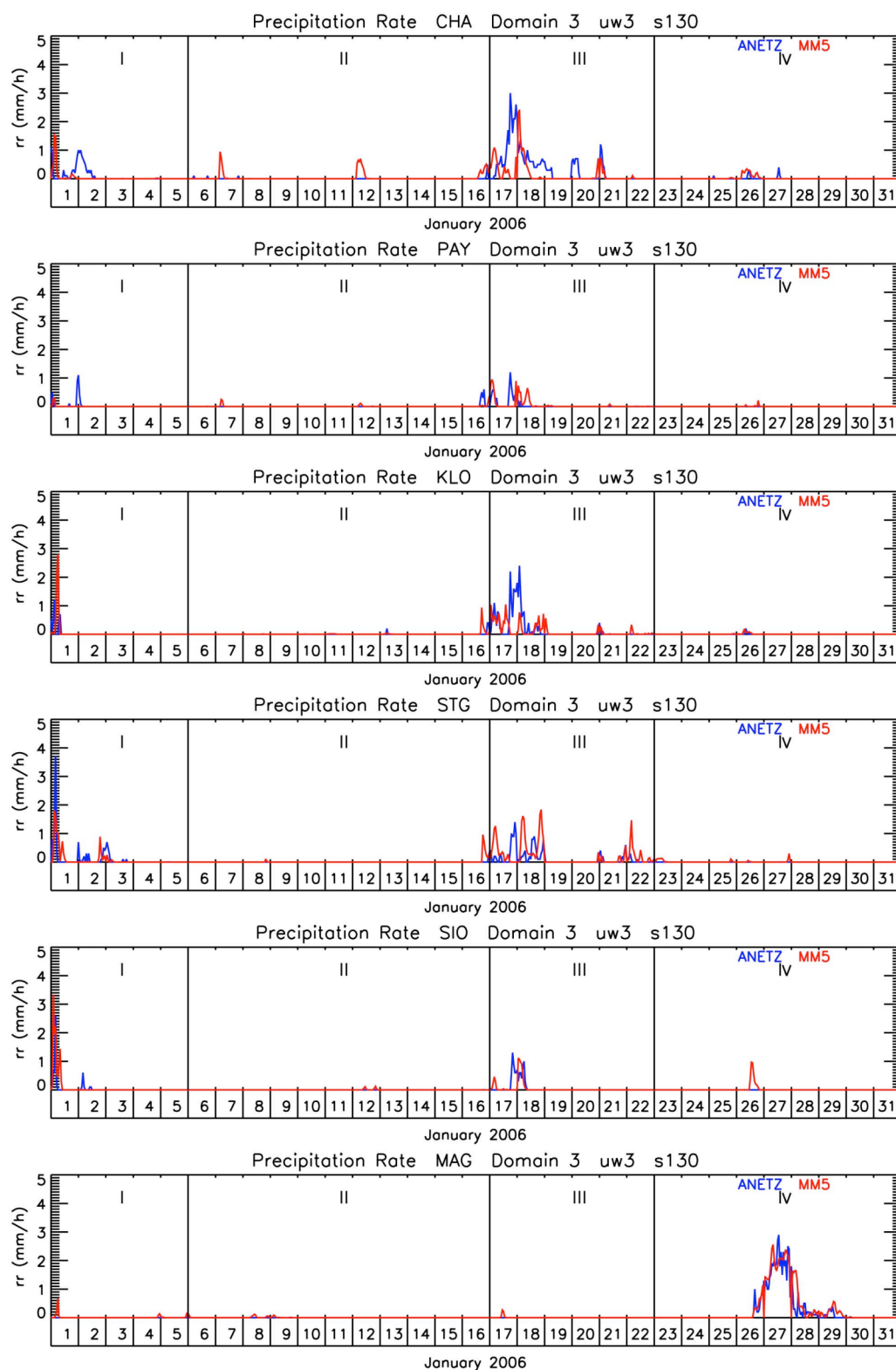


Figure A7: Surface measurements and simulations of precipitation rate at the ANETZ sites Chasseral (CHA), Payerne (PAY), Zurich Airport (KLO), St. Gallen (STG), Sion (SIO) and Magadino (MAG) in January 2006. Blue: ANETZ, red: MM5.

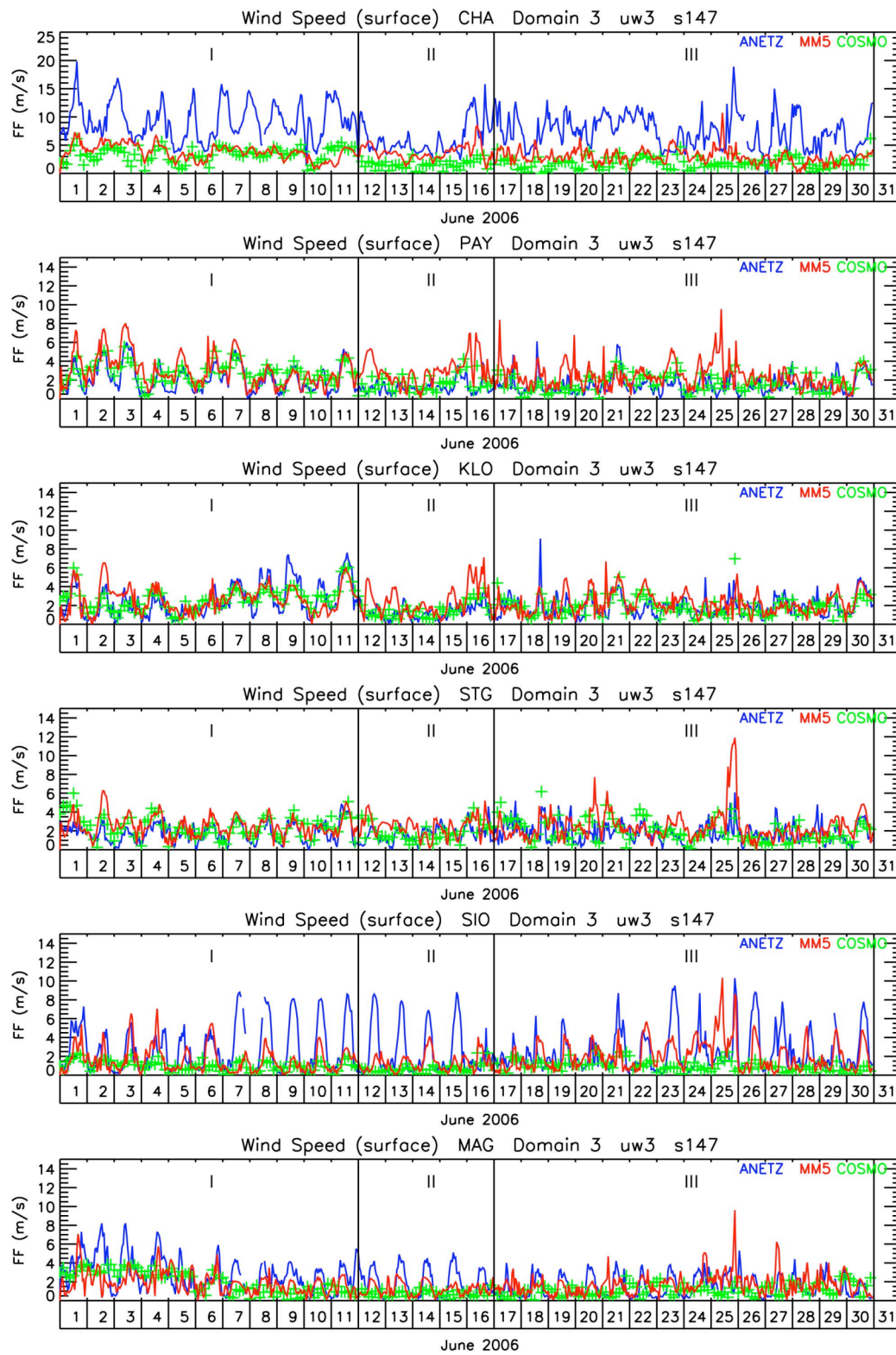


Figure A8: Surface measurements and simulations of wind velocity at the ANETZ sites Chasseral (CHA), Payerne (PAY), Zurich Airport (KLO), St. Gallen (STG), Sion (SIO) and Magadino (MAG) in June 2006. Blue: ANETZ, red: MM5, green: COSMO 7 (3h)

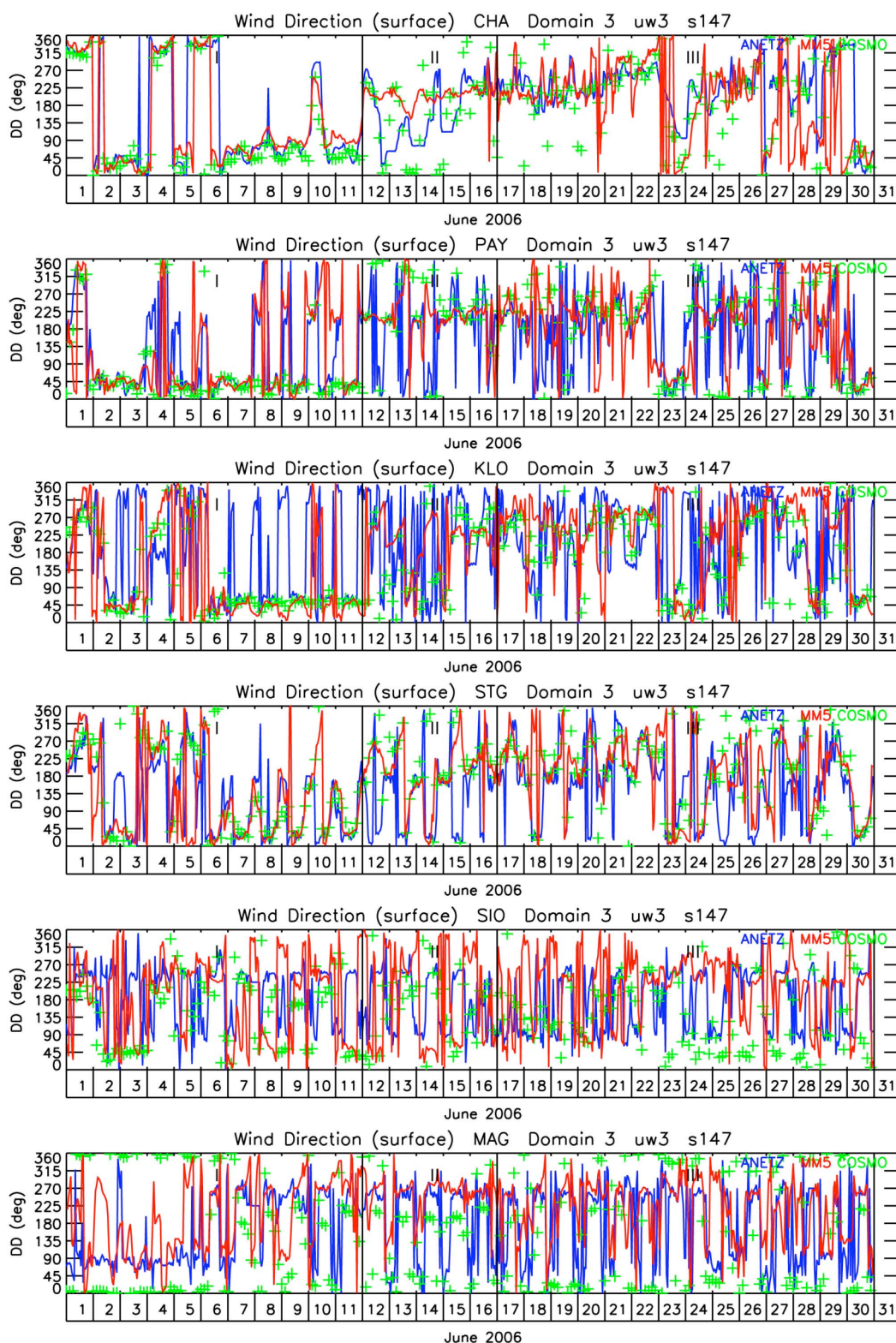


Figure A9: Surface measurements and simulations of wind direction at the ANETZ sites Chasseral (CHA), Payerne (PAY), Zurich Airport (KLO), St. Gallen (STG), Sion (SIO) and Magadino (MAG) in June 2006. Blue: ANETZ, red: MM5, green: COSMO 7 (3h)

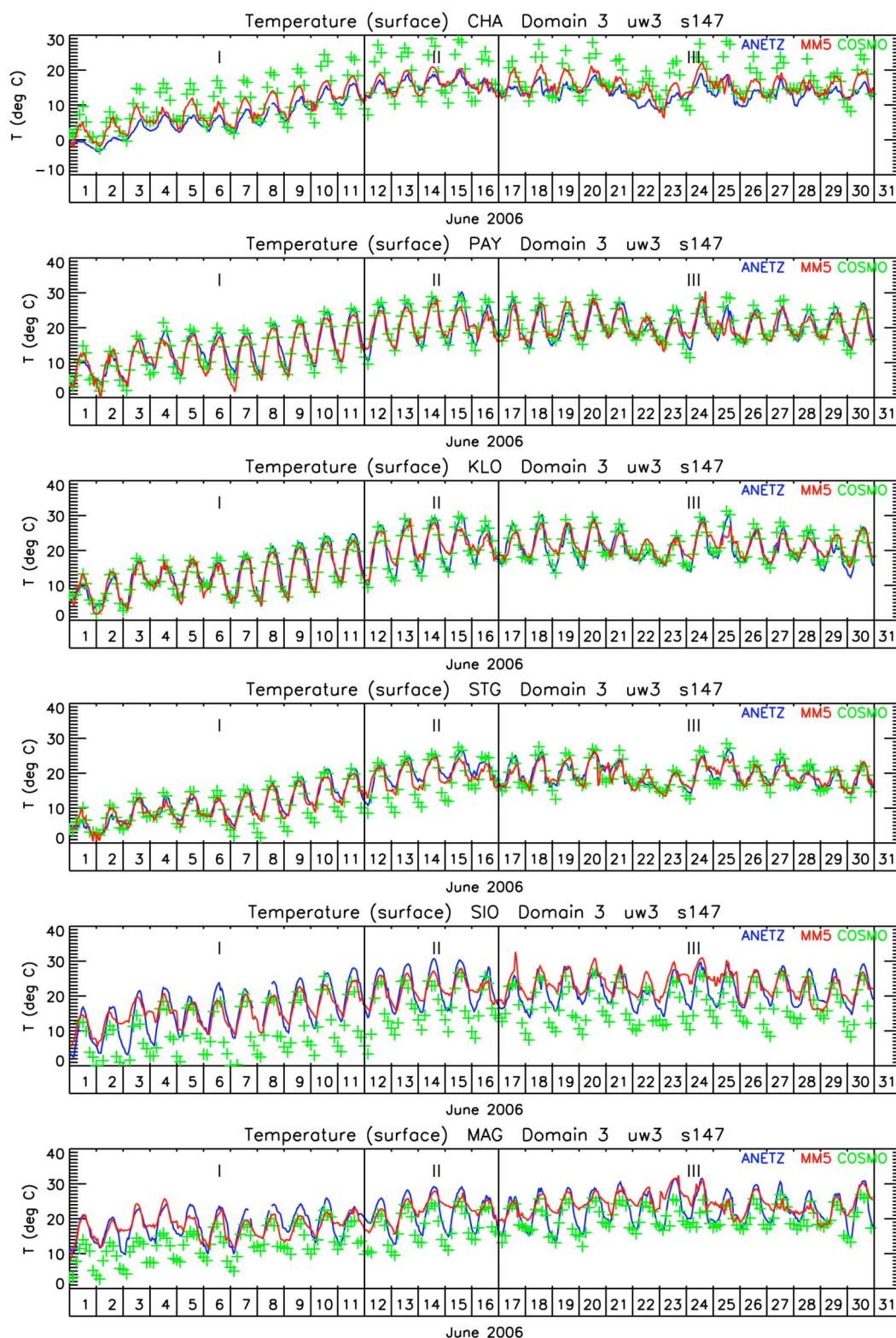


Figure A10: Surface measurements and simulations of air temperature at the ANETZ sites Chasseral (CHA), Payerne (PAY), Zurich Airport (KLO), St. Gallen (STG), Sion (SIO) and Magadino (MAG) in June 2006. Blue: ANETZ, red: MM5, green: COSMO 7 (3h)

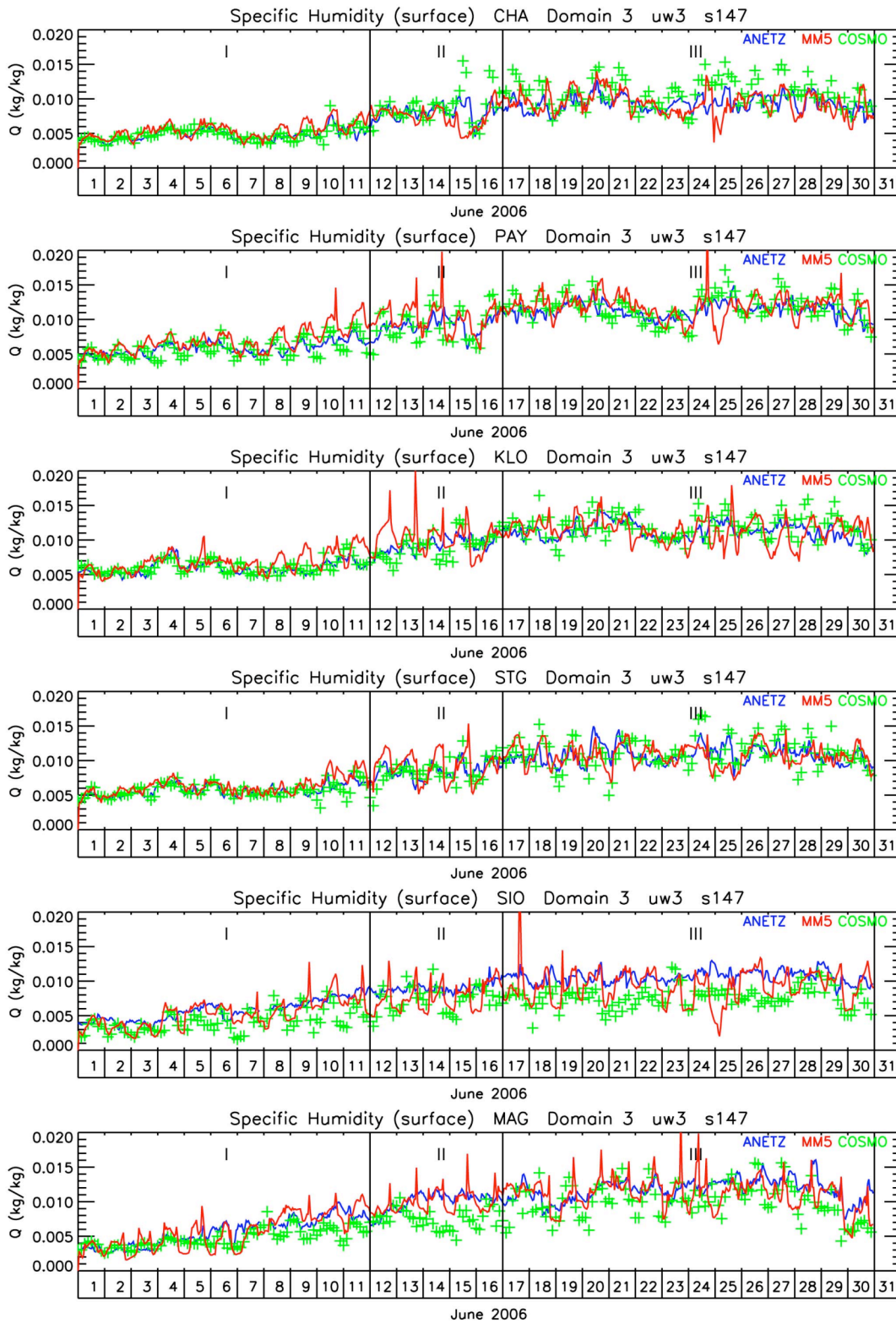


Figure A11: Surface measurements and simulations of specific humidity at the ANETZ sites Chasseral (CHA), Payerne (PAY), Zurich Airport (KLO), St. Gallen (STG), Sion (SIO) and Magadino (MAG) in June 2006. Blue: ANETZ, red: MM5, green: COSMO 7 (3h)

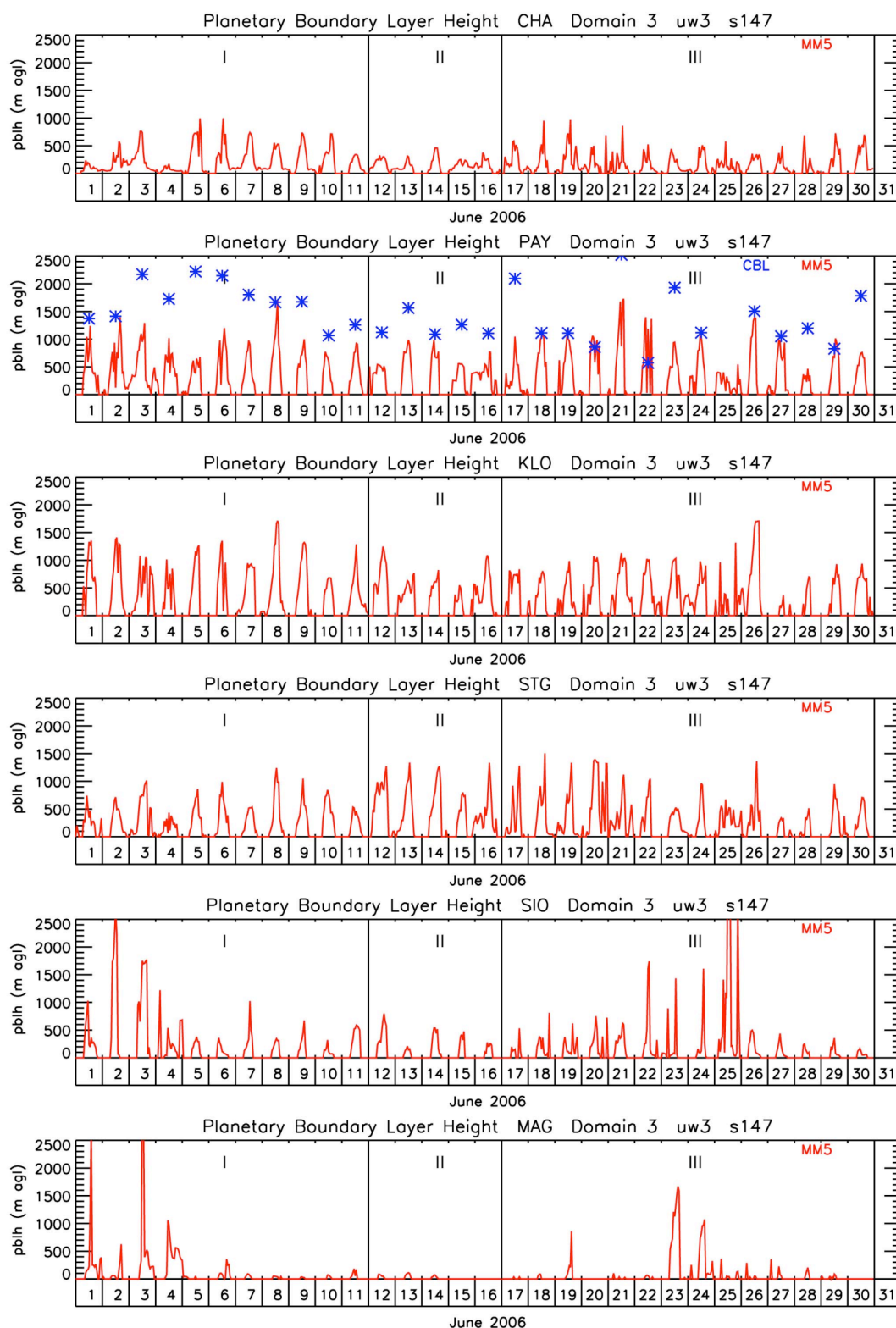


Figure A13: Simulations of planetary boundary layer height at the ANETZ sites Chasseral (CHA), Payerne (PAY), Zurich Airport (KLO), St. Gallen (STG), Sion (SIO) and Magadino (MAG) in June 2006. Blue: convective boundary layer (CBL) height derived from Payerne soundings, red: MM5.

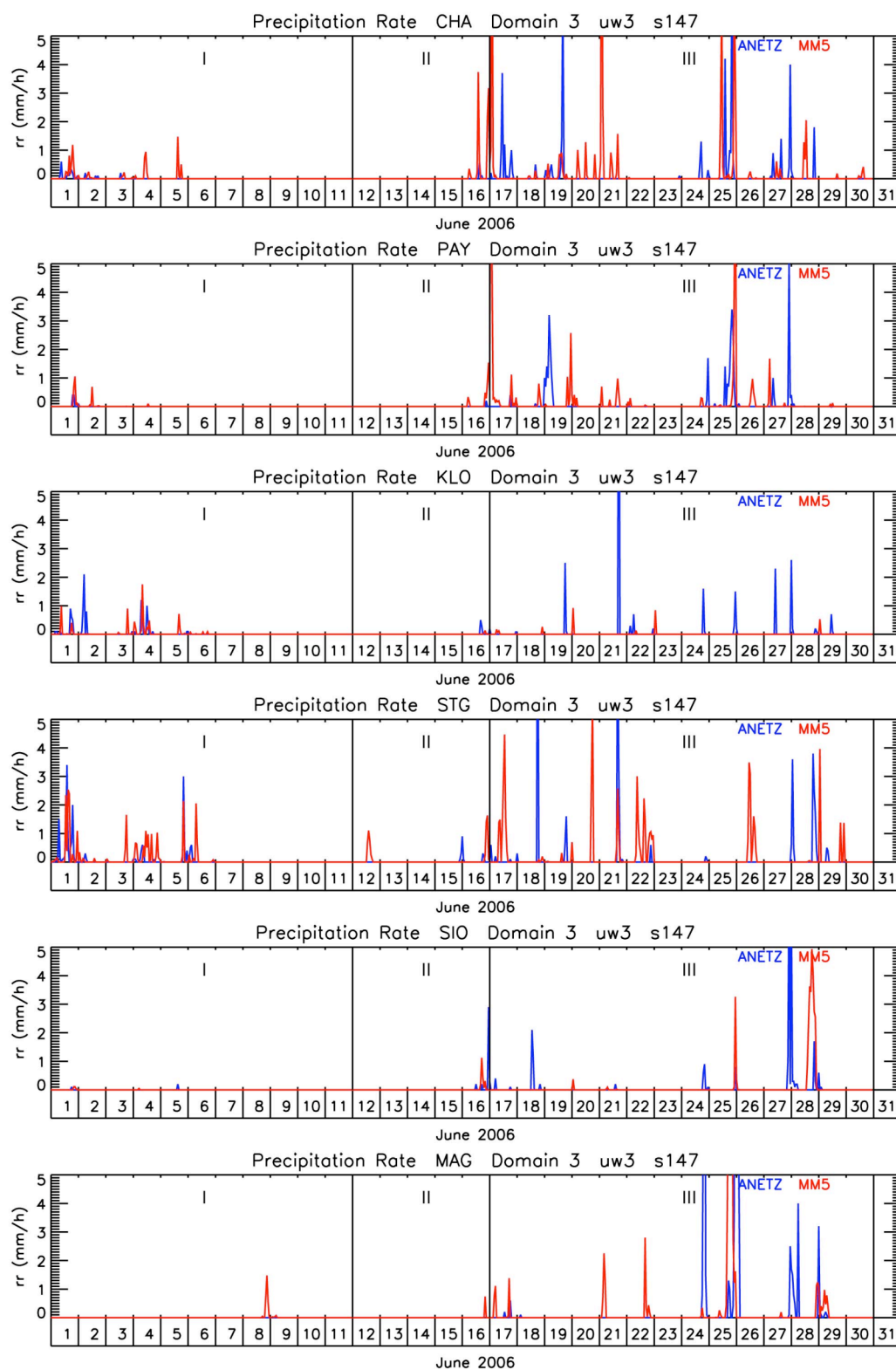


Figure A14: Surface measurements and simulations of precipitation rate at the ANETZ sites Chasseral (CHA), Payerne (PAY), Zurich Airport (KLO), St. Gallen (STG), Sion (SIO) and Magadino (MAG) in June 2006. Blue: ANETZ, red: MM5.

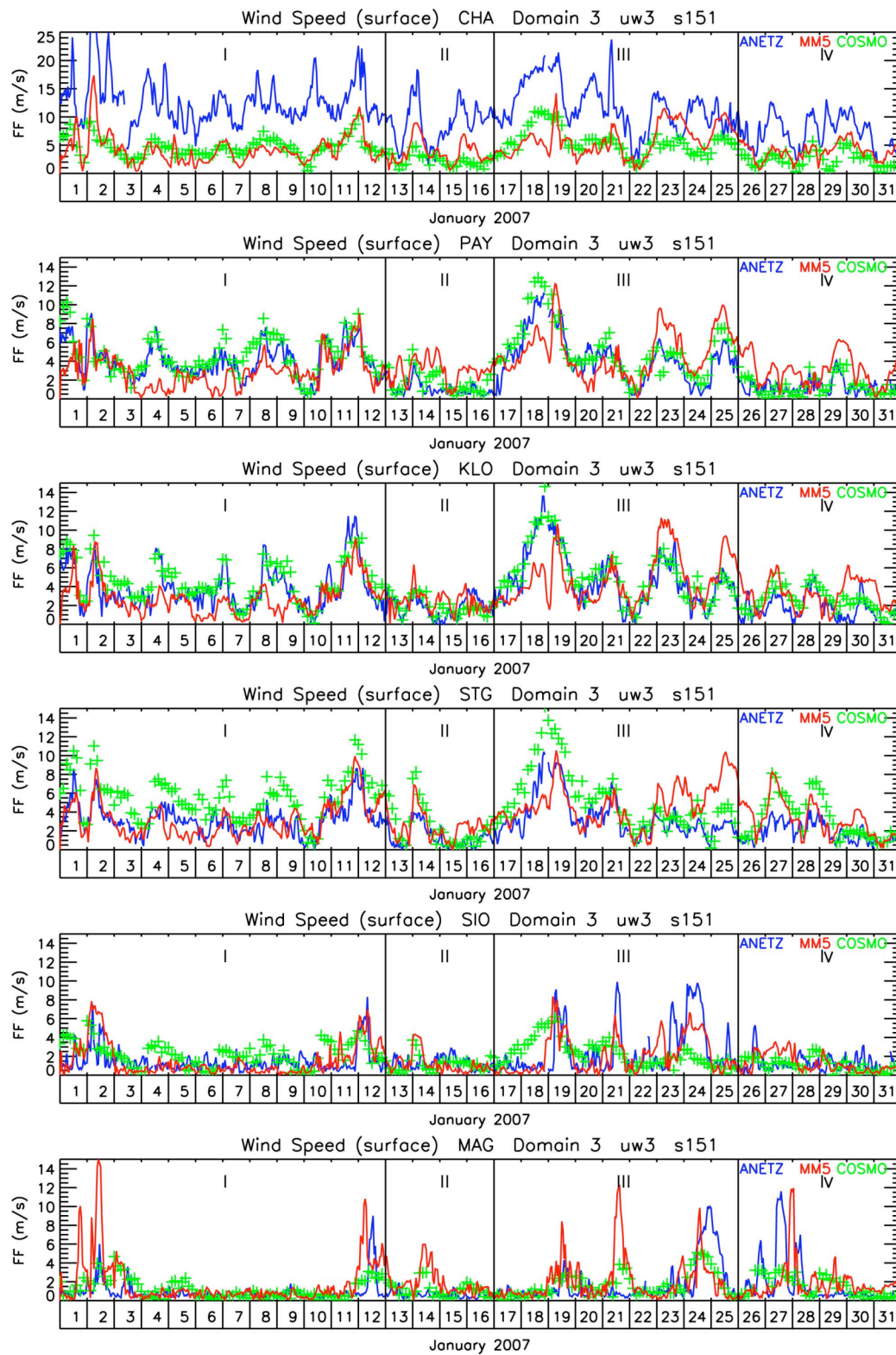


Figure A15: Surface measurements and simulations of wind velocity at the ANETZ sites Chasseral (CHA), Payerne (PAY), Zurich Airport (KLO), St. Gallen (STG), Sion (SIO) and Magadino (MAG) in January 2007. Blue: ANETZ, red: MM5, green: COSMO 7 (3h)

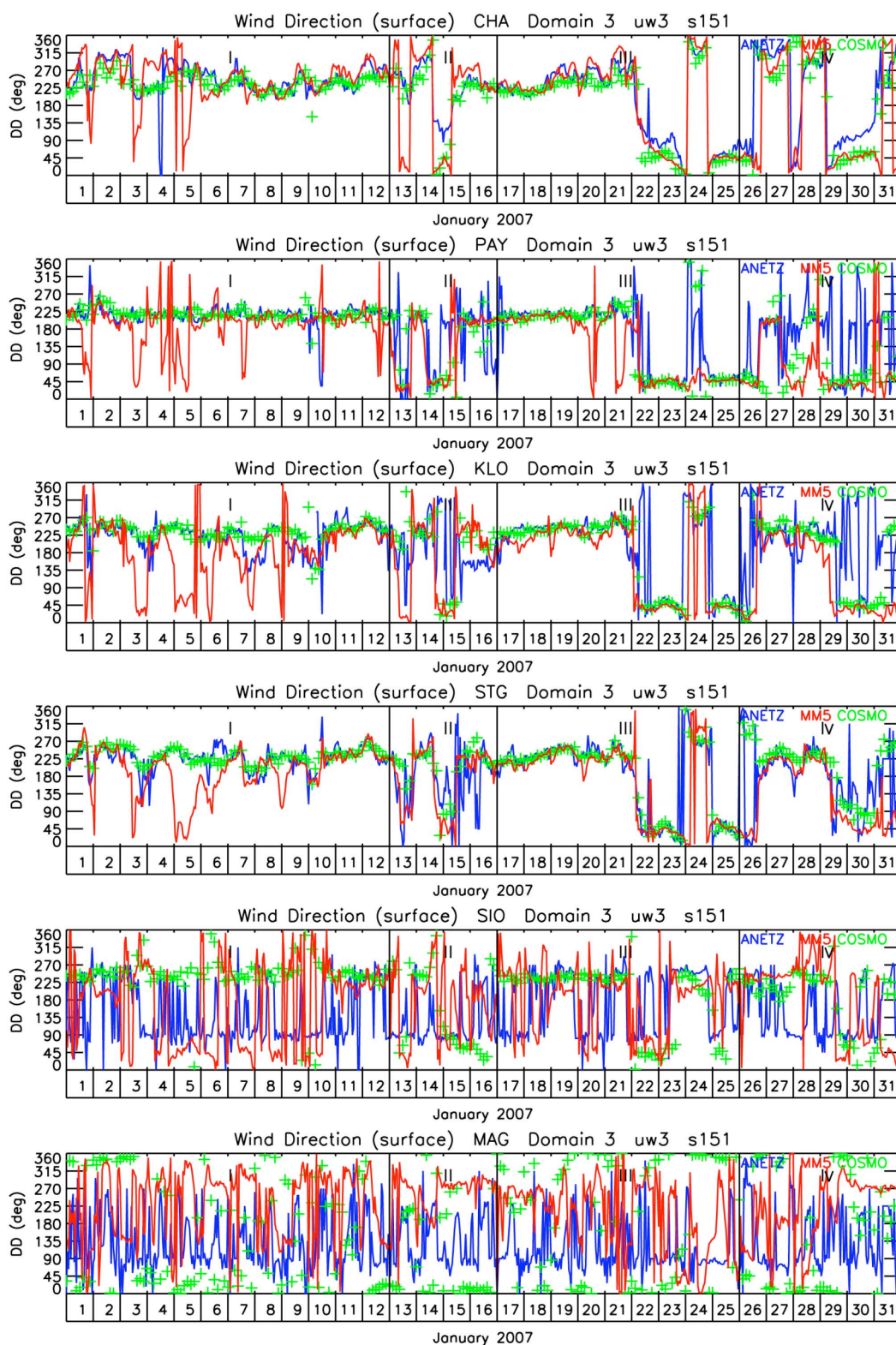


Figure A16: Surface measurements and simulations of wind direction at the ANETZ sites Chasseral (CHA), Payerne (PAY), Zurich Airport (KLO), St. Gallen (STG), Sion (SIO) and Magadino (MAG) in January 2007. Blue: ANETZ, red: MM5, green: COSMO 7 (3h)

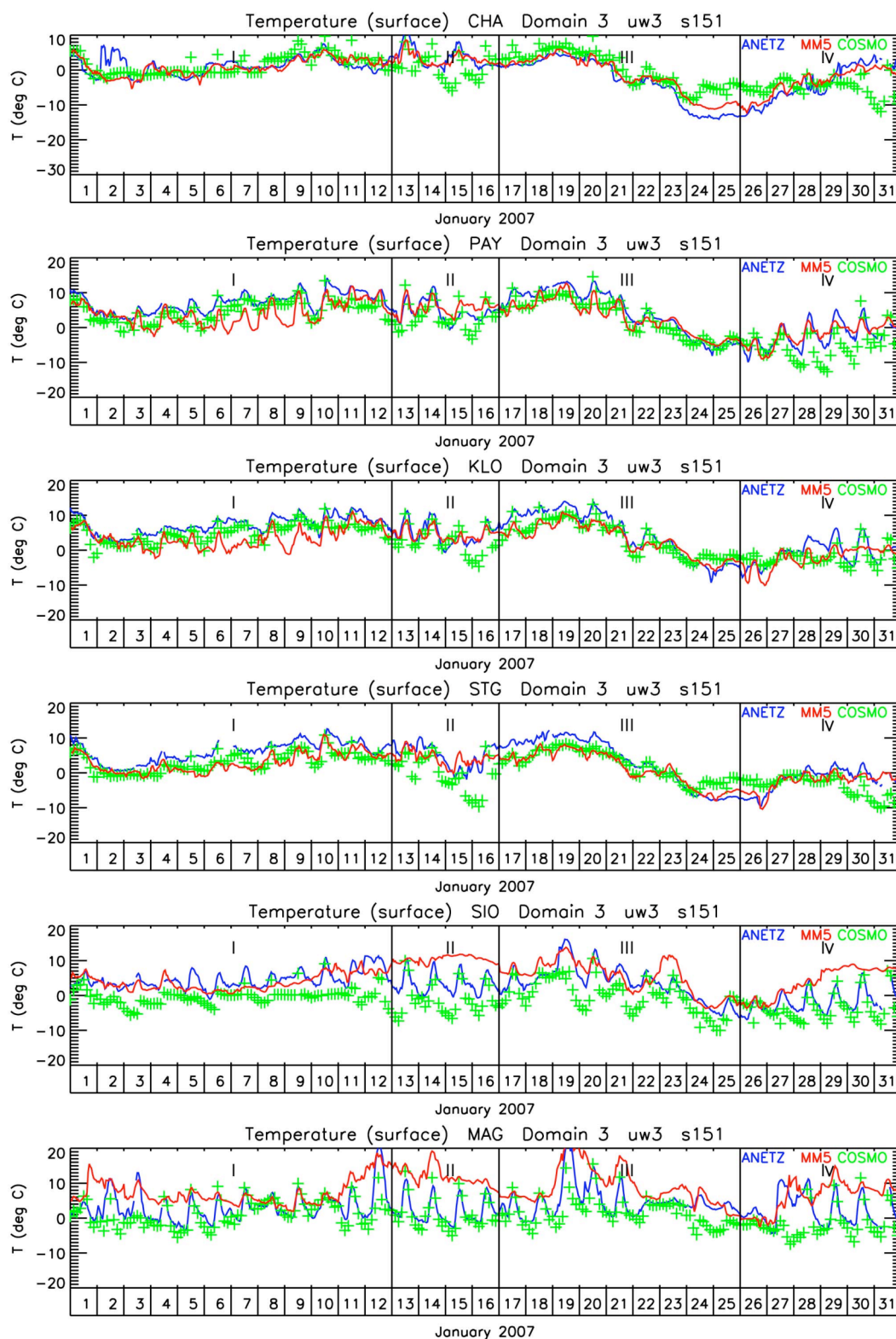


Figure A17: Surface measurements and simulations of air temperature at the ANETZ sites Chasseral (CHA), Payerne (PAY), Zurich Airport (KLO), St. Gallen (STG), Sion (SIO) and Magadino (MAG) in January 2007. Blue: ANETZ, red: MM5, green: COSMO 7 (3h)

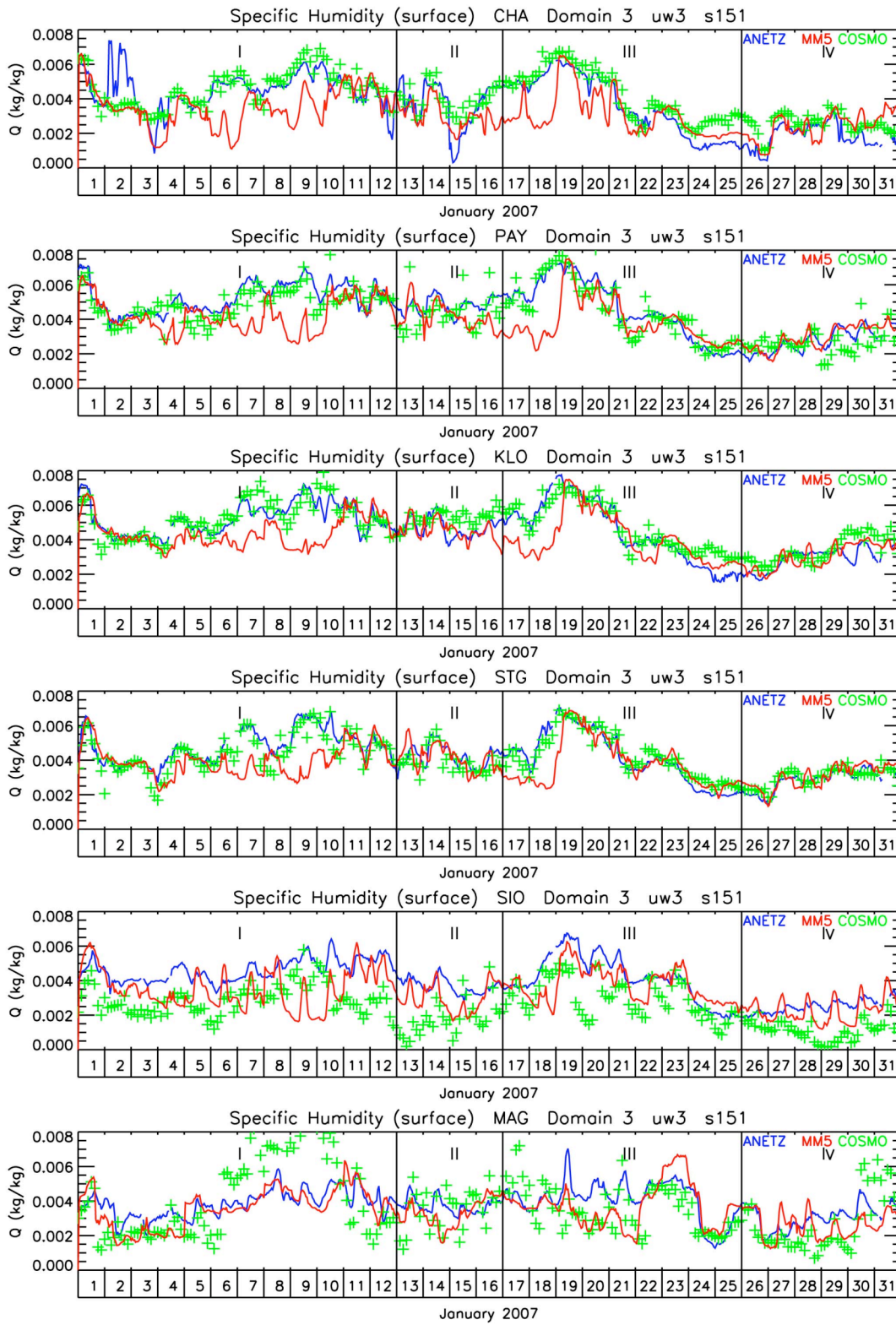


Figure A18: Surface measurements and simulations of specific humidity at the ANETZ sites Chasseral (CHA), Payerne (PAY), Zurich Airport (KLO), St. Gallen (STG), Sion (SIO) and Magadino (MAG) in January 2007. Blue: ANETZ, red: MM5, green: COSMO 7 (3h)

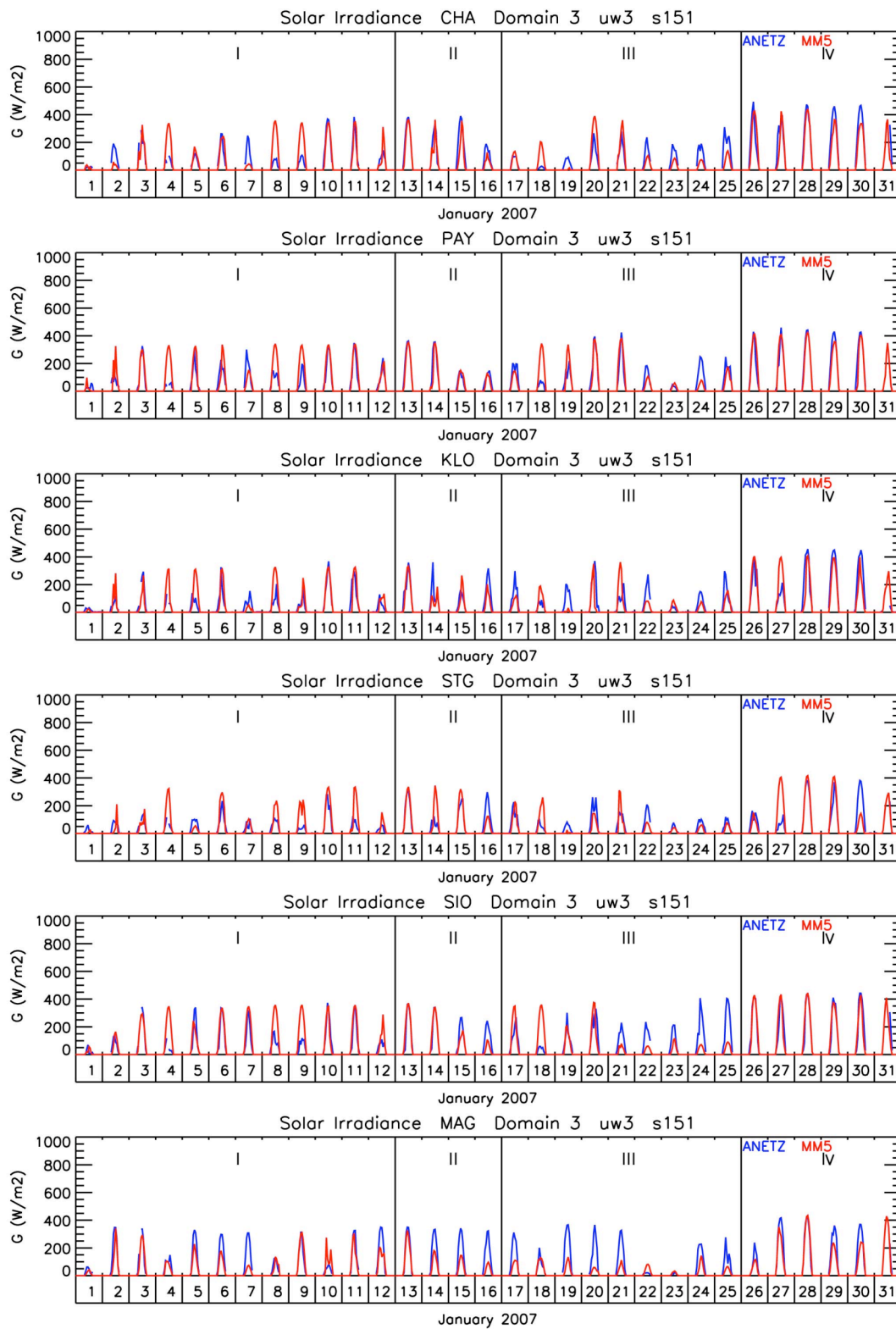


Figure A19: Surface measurements and simulations of global irradiance at the ANETZ sites Chasseral (CHA), Payerne (PAY), Zurich Airport (KLO), St. Gallen (STG), Sion (SIO) and Magadino (MAG) in January 2007. Blue: ANETZ, red: MM5.

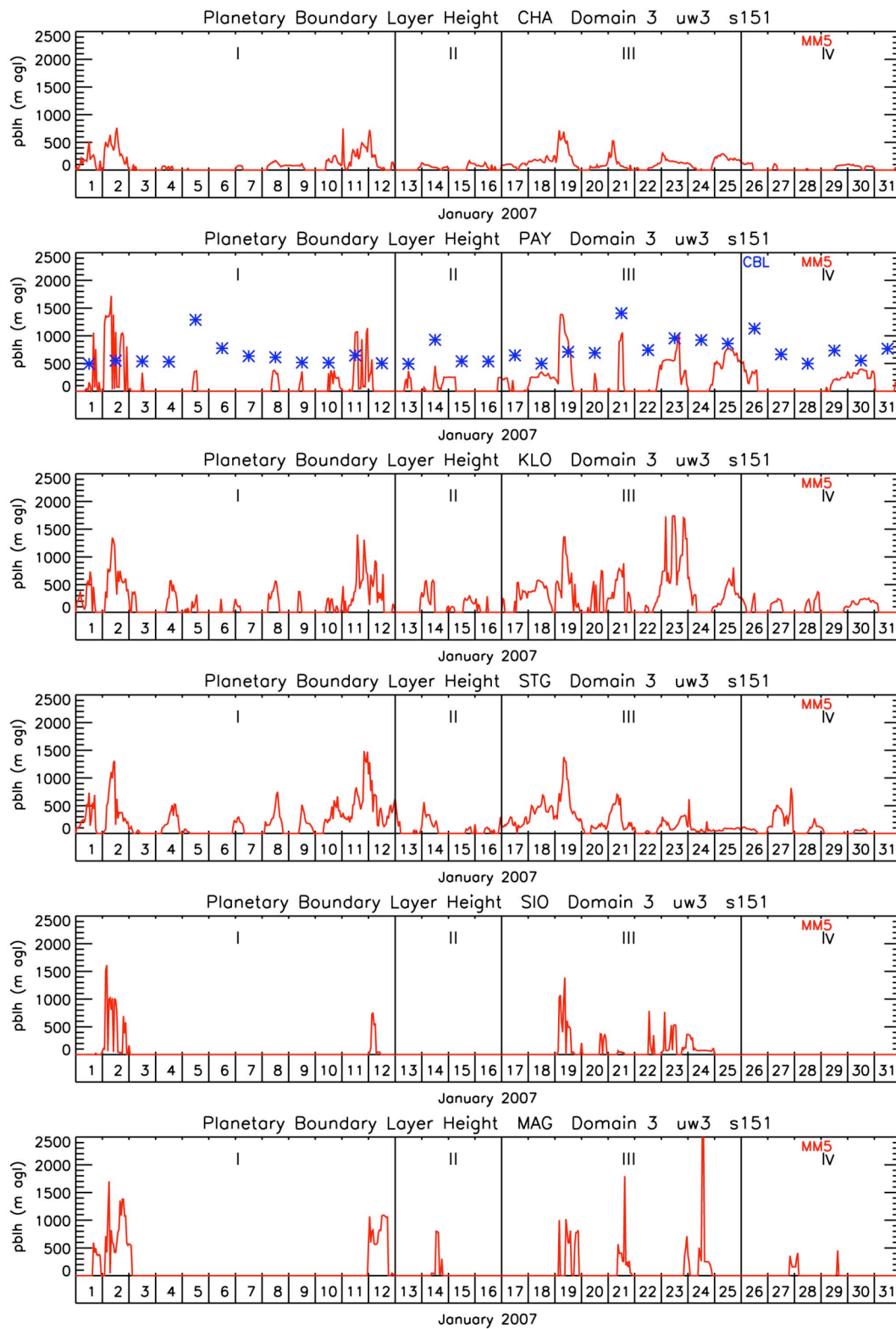


Figure A20: Simulations of planetary boundary layer height at the ANETZ sites Chasseral (CHA), Payerne (PAY), Zurich Airport (KLO), St. Gallen (STG), Sion (SIO) and Magadino (MAG) in January 2007. Blue: convective boundary layer (CBL) height derived from Payerne soundings, red: MM5.

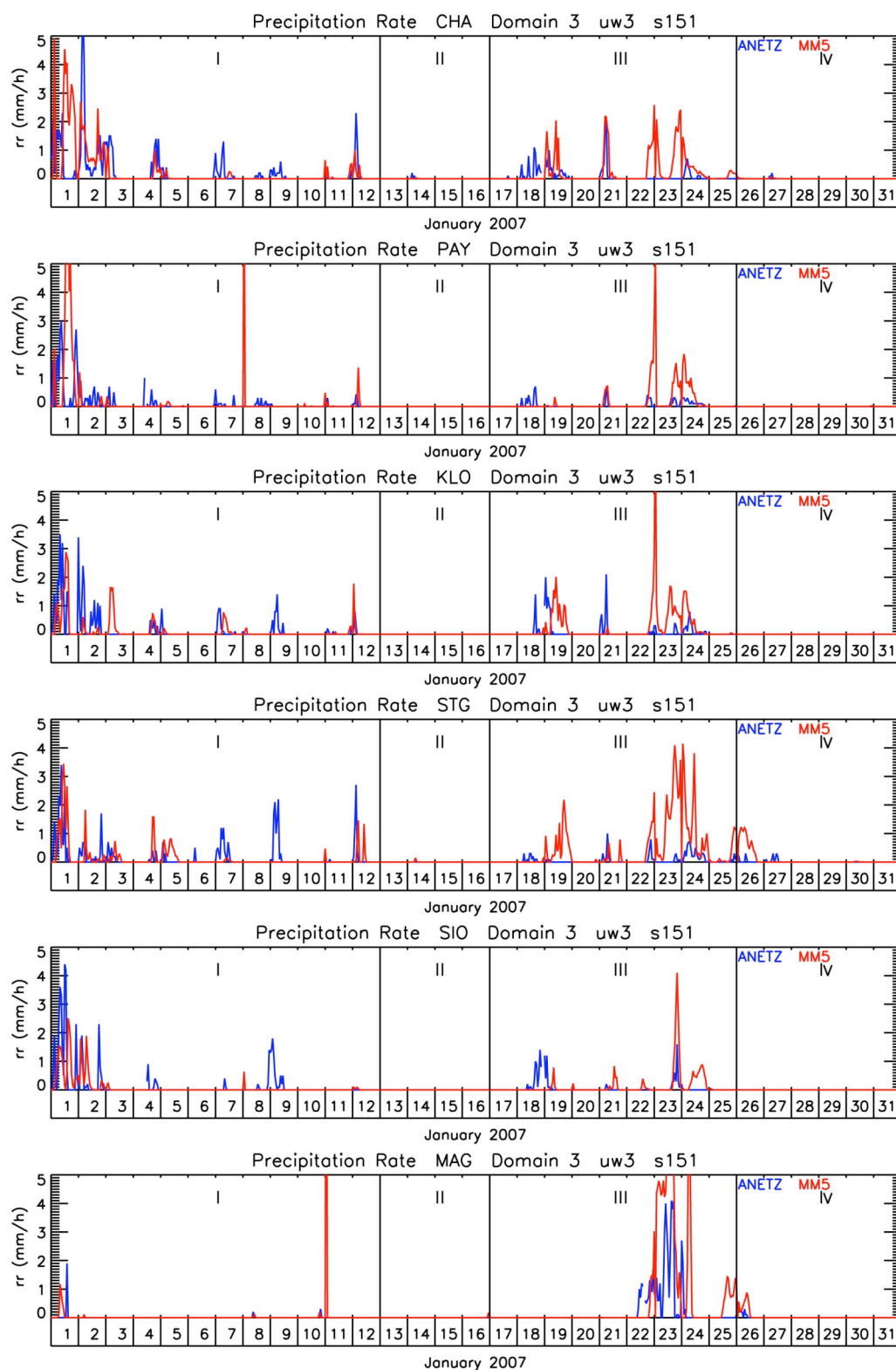


Figure A21: Surface measurements and simulations of precipitation rate at the ANETZ sites Chasseral (CHA), Payerne (PAY), Zurich Airport (KLO), St. Gallen (STG), Sion (SIO) and Magadino (MAG) in January 2007. Blue: ANETZ, red: MM5.